Title
Tuning magnetism and band topology in intrinsic magnetic topological insulators MnBi2nTe3n+1

Author
Hu, Chaowei

Publication Date
2022

Peer reviewed|Thesis/dissertation

UNIVERSITY OF CALIFORNIA

Los Angeles

Tuning magnetism and band topology in intrinsic magnetic topological insulators $MnBi_{2n}Te_{3n+1}$

A dissertation submitted in partial satisfaction

of the requirements for the degree

Doctor of Philosophy in Physics

by

Chaowei Hu

2022

ABSTRACT OF THE DISSERTATION

Tuning magnetism and band topology in intrinsic magnetic topological insulators $MnBi_{2n}Te_{3n+1}$

by

Chaowei Hu
Doctor of Philosophy in Physics
University of California, Los Angeles, 2022
Professor Ni Ni, Chair

Topological materials are materials whose electronic band structures are described by certain non-trivial topological invariants. Forty years ago the importance of band topology in condensed matter physics was first recognized when the quantum Hall effect (QHE) was found to be related with the integer Chern number in two-dimensional (2D) electron gas. Since 2008, the discovery of three-dimensional (3D) topological insulators (TI) with a non-trivial topological invariant and gapless surface state has taken the field into a new era. Various new topological phases were proposed and band topology has become a new way to classify the state of matter.

The design, synthesis and characterization of new topological materials pave essential basis to uncovering novel physics arising from non-trivial band topology and its interplay with various degrees of freedom such as spin, orbital and charge. Today, with more sought-after novel topological phases, emergent phenomena such as surface Fermi arcs, chiral anomaly, quantum anomalous Hall effect were discovered and enable future technological advances including topological quantum computation. A new topological phase can be created when additional symmetry breaking is introduced into an existing topological phase. For example, by breaking the time reversal symmetry of a 3D TI through ferromagnetism (FM), one can

get a Chern insulator in its 2D limit, where QHE can be realized without external magnetic field and gives topologically-protected dissipationless chiral edge states. This phenomenon, the so-called quantum anomalous Hall effect (QAHE), has been long sought since its early proposal in the yet-to-be-realized Haldane model for graphene lattice with opposite magnetic field at neighboring atoms in 1988. Therefore, the realization of QAHE in magnetically-doped TI $Cr_{0.15}(Bi_{0.1}Sb_{0.9})_{1.85}Te_3$ thin films in 2013 was revolutionary. However, the unavoidable sample inhomogeneity in doped materials restrains the investigation of associated emergent phenomena in mK-regime. Ideally, magnetism from intrinsic magnetic atoms in a crystal can provide more homogeneous electronic and magnetic properties than the magnetism from dopants. To realize QAHE at higher temperatures, the intrinsic magnetic TIs with only clean topological bands but no other bands at the Fermi level are strongly desired. In 2018, $MnBi_2Te_4$ was discovered to be the first of such kinds, as an antiferromagnetic (AFM) TI with intrinsic magnetic Mn site. It is a layered van der Waals (vdW) material. When the magnetism orders below 24 K, the spins are FM aligned in the *ab* plane but AFM coupled along the *c* axis. In 2D limit, $MnBi_2Te_4$ films can have a net magnetization either in odd-layer devices, or when the even-layer devices are in the spin-flop state above $\sim$ 3.5 T and the forced FM state above $\sim$ 8 T. These time-reversal-symmetry breaking states are ideal for realizing the Chern insulator state. Indeed, QAHE was experimentally observed at 0 T and 1.6 K in a 5-layer device and quantized Hall conductance was realized when the even-layer devices enter the forced FM state above the saturation field of 8 T.

Following this line, for QAHE to be realized at zero field and higher temperature, it is strongly desirable if the FM alignment of Mn spins can be accessed at a lower or even zero field. To do so, one must weaken the interlayer AFM interactions between $[MnBi_2Te_4]$ layers. We thus propose to introduce $n-1$ nonmagnetic TI $[Bi_2Te_3]$ layers between $[MnBi_2Te_4]$ layers to get natural heterostructures of $MnBi_{2n}Te_{3n+1}$. By this rational design, we can increase the distance between the neighboring $[MnBi_2Te_4]$ layers and thus reduce the interlayer AFM interaction. Under such a design principle we successfully grew single crystals of $MnBi_4Te_7$ ($n = 2$), $MnBi_6Te_{10}$ ($n = 3$) and $MnBi_8Te_{13}$ ($n = 4$). Then with the physical property

characterization, first-principles calculations and angle-resolved photoemission spectroscopy measurements, for the first time, we demonstrated that $MnBi_4Te_7$ is an intrinsic AFM TI with saturation field 40 times smaller than that of $MnBi_2Te_4$, and that $MnBi_8Te_{13}$ is the first realization of an intrinsic FM axion insulator, proving the success of our material design principle.

The manipulation of magnetism is crucial to access different magnetic topological phase and novel physics. In $MnBi_{2n}Te_{3n+1}$, the control of the magnetism from AFM to FM by n is only discrete. To achieve a fine and continuous control of the magnetic transition, we doped Sb to $MnBi_4Te_7$ where the interlayer AFM coupling is weak and more tunable. Through single crystal growth, transport, thermodynamic, neutron diffraction measurements, we show that under Sb doping, $MnBi_4Te_7$ evolves from AFM to FM and then ferrimagnetic. We attribute this to the formation of $Mn_{(Bi,Sb)}$ antisites upon doping, which results in additional Mn sublattices that modify the delicate interlayer magnetic interactions and changes the overall magnetism. We further investigate the effect of antisites on the band topology using the first-principles calculations. Without considering antisites, the series evolves from AFM topological insulator ($x = 0$) to FM axion insulators. In the exaggerated case of 16.7% of periodic antisites, the band topology is modified and type-I magnetic Weyl semimetal phase can be realized at intermediate doping. Therefore, this doping series provides a fruitful platform with rich and continuously tunable magnetism and topology.

After we achieve FM in $MnBi_{2n}Te_{3n+1}$, for practical applications especially in the pursuit of high temperature QAHE when fluctuations become important, the study on magnetic dynamics is indispensable too. We investigated the magnetic dynamics in FM $MnBi_8Te_{13}$ and Sb doped $MnBi_4Te_7$ and $MnBi_6Te_{10}$ using AC susceptibility and magneto-optical imaging. Slow relaxation behavior is observed in all three compounds, suggesting its universality among FM $MnBi_{2n}Te_{3n+1}$. The origin of the relaxation behavior is attributed to the irreversible domain movements since they only appear below the saturation fields when FM domains form and evolve. These FM domains are very soft, as revealed by the low-field fine-structured domains and high-field sea-urchin-shaped remnant-state domains imaged via

the magneto-optical measurements. Finally, we attribute the rare "double-peak" behavior observed in the AC susceptibility under small DC bias fields to the very soft FM domain formations. This study provides a thorough understanding of the soft FM in highly anisotropic magnets.

As the first intrinsic antiferromagnetic topological insulator, $MnBi_2Te_4$ is still the major material platform to search for QAHE, so its material optimization is very urged. We develop the chemical-vapor-transport (CVT) growth for of $MnBi_2Te_4$, which has a higher success rate in observation of the field-induced quantized Hall conductance in 6-layer devices. Through comparative studies between our CVT-grown and flux-grown $MnBi_2Te_4$, we find that CVT-grown $MnBi_2Te_4$ is marked with higher Mn occupancy on the Mn site, slightly higher Mn_{Bi} antisites and smaller carrier concentration. On the device end, thin film from CVT-grown sample shows by far the highest mobility of 2500 $cm^2 \cdot V \cdot s$ in $MnBi_2Te_4$ devices with the quantized Hall conductance appearing at 1.8 K and 8 T. This study provides a route to obtain high-quality single crystals of $MnBi_2Te_4$ that are promising to make superior devices and realize emergent phenomena.

In summary, we have discovered and established $MnBi_4Te_7$ and $MnBi_8Te_{13}$ as new intrinsic magnetic topological insulators. In particular, we provide deep understanding of the importance of material design, synthesis and chemical doping to the magnetism and topology in the series. The growths of high-quality single crystals and the study of magnetic dynamics provide essential basis for the search of QAHE in $MnBi_{2n}Te_{3n+1}$. Our works will shed light on future endeavors in finding novel magnetic topological materials as well as searching for QAHE and the associated emergent phenomena in the condensed matter field.

The dissertation of Chaowei Hu is approved.

Hong-wen Jiang

Stuart Brown

Paula Loredana Diaconescu

Ni Ni, Committee Chair

University of California, Los Angeles

2022

Ad maiorem Dei gloriam

Table of Contents

List of Figures

List of Tables

Acknowledgements

The journey of Ph.D. has been a long and difficult, yet cheerful and life-changing one. The past years has seen may times of joy and stress, delight and frustration, sowing and reaping, to which I cannot be thankful enough. The completion of the thesis is attributed to the support from many.

First and foremost, I would like to express my gratitude to Dr. Ni Ni for her generous support and caring mentorship. Throughout my Ph.D., she has been a constant source of motivation and inspiration of new ideas. She always encourages me to ask question fearlessly in my earlier years, which I find to be a simple but precious gem. Her passion of science was infectious to me, and I always benefited much from her experimental instinct during discussion with her. Through her networks, I also get to interact with top scientists through our collaborations, and she has been very supportive in sponsoring me to travelling to various conferences and national laboratories. All these aspects have helped me become a better experimentalist.

It has also been a great honor to work with many past and current members of Ni's lab. I learned and mastered the synthesis skills under the guidance from the fellow postdocs Bing Shen, Jie Xing, and Jinyu Liu. Eve Emmanouilidou is the one graduate student I overlapped and talked to the most in the past years. I benefited from her discussion and advice, as well as our time to troubleshoot equipment together. I enjoyed too working with Tiema Qian and J Green, who came in the lab after me and brought in new ideas and insights. Talking to them daily and being able to grow in science together has been a rewarding experience. I would also like to thank undergraduate researchers Scott Mackey and Jacklyn Zhu for their assistance and opportunity for me to mentor them.

My works would not be accomplished without our wonderful collaborators, and many "office hours" I got from them. Huibo Cao, Lei Ding, and Erxi Feng at ORNL helped us with many neutron diffraction measurement and taught me step-by-step how to refine an unknown crystal and magnetic structure. It was a pleasure to collaborate with Kyle and

Byran from Daniel Dessau's group at CU Boulder on ARPES measurement, and Qihang Liu's and Tay-Rong Chang's group at SUSTech and NCKU who performed band structure calculations. The magneto-optic imaging was done by Ruslan Prozorov from Ames lab. A special thanks to Suyang Xu and his team members at Harvard University, Anyuan Gao, Ted Liu, Jianxiang Qiu, Houchen Li, Sheng-Chin Ho for their collaborations and discussions on Mn-Bi-Te devices and for hosting me to learn about device fabrication process. I learned valuable experiences and gained much insight on the 2D device applications.

Outside our lab, I learned a lot from the interaction within the UCLA physics department. Other than the introductory and solid-state courses, it was a pleasure to be a part of the condensed matter experiment journal club with Prof. Stuart Brown's, Prof. Anshul Kogar's, Prof. Christopher Gutiérrez's and Prof. Qianhui Shi's groups. Meetings with them on different research topics regularly greatly expanded my vision of the condensed matter field. In addition, I cannot thank enough Professor Seth Putterman and the Schwinger foundation, which he is a part of, to support me financially for a year at UCLA and then three-month research at Harvard. It has been a major encouragement for me to pursue my research interests. Finally, I would like to thank Prof. Stuart, Prof. Brown, Prof. Jiang and Prof. Diaconescu for advising my thesis.

I would like to express my gratitude to all my friends who accompanied me during the graduate school years: Yiqing Shi, Jingkang Yu, Helen Kwak, Amy Hung, Peter Chen, Amanda Chuang, Peng-Yu Chen, Eric and Zixun Yu, Anne, Shawn and Emmanuel Yeh, and many more. With them I shared the most memorable times. It has been a blessing to have them around in this journey.

Lastly, I would like to thank my beloved family for their unwavering love. I would never be where I am today without my parents' trust and support of my passion since my childhood. My sister always believes in me in all I do. Having her around has been a bliss. My partner Yang has been a major source of joy in my PhD too. Thank you for always making me laugh and keeping me cheered up even during my toughest time!

Curriculum Vitae

June 2016	B.S. in Physics
	B.S. in Chemistry/Material Science
	Minor in Mathematics
	University of California, Los Angeles

Publications

[1] C. Hu, K. N. Gordon, P. Liu, J. Liu, X. Zhou, P. Hao, D. Narayan, E. Emmanouilidou, H. Sun, Y. Liu, *et al.*, "A van der waals antiferromagnetic topological insulator with weak interlayer magnetic coupling," *Nature communications*, vol. 11, no. 1, pp. 1–8, 2020.

[2] C. Hu, L. Ding, K. N. Gordon, B. Ghosh, H.-J. Tien, H. Li, A. G. Linn, S.-W. Lien, C.-Y. Huang, S. Mackey, *et al.*, "Realization of an intrinsic ferromagnetic topological state in $MnBi_8Te_{13}$," *Science Advances*, vol. 6, no. 30, p. eaba4275, 2020.

[3] C. Hu, S.-W. Lien, E. Feng, S. Mackey, H.-J. Tien, I. I. Mazin, H. Cao, T.-R. Chang, and N. Ni, "Tuning magnetism and band topology through antisite defects in Sb-doped $MnBi_4Te_7$," *Phys. Rev. B*, vol. 104, p. 054422, Aug 2021.

[4] C. Hu, M. A. Tanatar, R. Prozorov, and N. Ni, "Unusual dynamic susceptibility arising from soft ferromagnetic domains in mnbi8te13 and sb-doped mnbite (n= 2, 3)," *Journal of Physics D: Applied Physics*, vol. 55, no. 5, p. 054003, 2021.

[5] C. Hu, A. Gao, B. S. Berggren, H. Li, R. Kurleto, D. Narayan, I. Zeljkovic, D. Dessau, S. Xu, and N. Ni, "Growth, characterization, and chern insulator state in $MnBi_2Te_4$ via the chemical vapor transport method," *Physical Review Materials*, vol. 5, no. 12, p. 124206, 2021.

[6] B. Shen, C. Hu, H. Cao, X. Gui, E. Emmanouilidou, W. Xie, and N. Ni, "Structural distortion and incommensurate noncollinear magnetism in $EuAg_4As_2$," *Physical Review Materials*, vol. 4, no. 6, p. 064419, 2020.

[7] K. N. Gordon, H. Sun, C. Hu, A. G. Linn, H. Li, Y. Liu, P. Liu, S. Mackey, Q. Liu, N. Ni, *et al.*, "Strongly gapped topological surface states on protected surfaces of antiferromagnetic $MnBi_4Te_7$ and $MnBi_6Te_{10}$," *arXiv Preprint:1910.13943*, 2019.

[8] Y.-J. Hao, P. Liu, Y. Feng, X.-M. Ma, E. F. Schwier, M. Arita, S. Kumar, C. Hu, M. Zeng, Y. Wang, *et al.*, "Gapless surface dirac cone in antiferromagnetic topological insulator $MnBi_2Te_4$," *Physical Review X*, vol. 9, no. 4, p. 041038, 2019.

[9] D. Ryan, S. L. Bud'ko, C. Hu, and N. Ni, "Magnetic and structural transitions in $EuAg_4As_2$ studied using ^{151}Eu mössbauer spectroscopy," *AIP Advances*, vol. 9, no. 12, p. 125050, 2019.

[10] L. Ding, C. Hu, F. Ye, E. Feng, N. Ni, and H. Cao, "Crystal and magnetic structures of magnetic topological insulators $MnBi_2Te_4$ and $MnBi_4Te_7$," *Physical Review B*, vol. 101, no. 2, p. 020412, 2020.

[11] L. Ding, C. Hu, E. Feng, C. Jiang, I. A. Kibalin, A. Gukasov, M. Chi, N. Ni, and H. Cao, "Neutron diffraction study of magnetism in van der waals layered $MnBi_{2n}Te_{3n+1}$," *Journal of Physics D: Applied Physics*, vol. 54, no. 17, p. 174003, 2021.

[12] A. Gao, Y.-F. Liu, C. Hu, J.-X. Qiu, C. Tzschaschel, B. Ghosh, S.-C. Ho, D. Bérubé, R. Chen, H. Sun, *et al.*, "Layer hall effect in a 2d topological axion antiferromagnet," *Nature*, vol. 595, no. 7868, pp. 521–525, 2021.

[13] T. Qian, M. H. Christensen, C. Hu, A. Saha, B. M. Andersen, R. M. Fernandes, T. Birol, and N. Ni, "Revealing the competition between charge density wave and superconductivity in CsV_3Sb_5 through uniaxial strain," *Physical Review B*, vol. 104, no. 14, p. 144506, 2021.

CHAPTER 1

Introduction to Magnetic topological insulator

Following the discovery of three-dimensional (3D) topological insulator (TI), the past decade has seen a booming growth of the studies of band topology in condensed matter physics. Band topology has since emerged as an organizing principle of the states of matter [1]. Fast forward to today, many topological phases, such as quantum spin Hall (QSH) insulators, quantum anomalous Hall (QAH) insulators, Dirac semimetals, and Weyl semimetals, have now been discovered [2, 3]. These topological phases are associated with particular nontrivial topological invariants which arise from the global property of the electronic structure, and are robust against perturbations. Inside these topological phases, emergent phenomena were theoretically proposed based on the interplay of nontrivial band topology and the charge, spin, orbital degrees of freedom. The material realization of different 3D topological phases has turned out to be the driving force of the field. It has enabled physicists to explore and discover many proposed phenomena, including the dissipationless edge transport, chiral anomaly effect, etc, making the past decade a new era of condensed matter physics.

Among these topological phases, the magnetic TI (MTI) phase has been the frontier of research. When ferromagnetism couples with the Dirac surface states in TI, it breaks the time-reversal symmetry, lifts the topological protection on the surface states, opens a surface gap and gives rise to new topological phases such as Axion insulators and QAH insulators. As a result, seeking MTI where emergent physics awaits exploration has been strongly desired. However, the search of MTI is challenging. Although first-principle calculations have been quite successful in predicting non-magnetic topological materials, they often run into inherent difficulties in successfully producing band structures due to the nature of strong electron-

electron correlations in these magnetic materials. Without much theoretical input, it remains a big challenge of the material search and realization of magnetic topological materials. To address this problem, my Ph. D work focuses on the search, design and studies of intrinsic magnetic topological insulators based on [$MnBi_2Te_4$] layered structure.

1.1 The structure of the thesis

My thesis is structured as the following. In Chapter 1, I will give an overview of two pillars of our studies on MTI - topology and magnetism. In Chapter 2, I will go over experimental techniques that allow us to grow single crystals and perform property characterizations. Chapters 3 and 4 discuss our discovery of the intrinsic antiferromagnetic TI $MnBi_4Te_7$ and the ferromagnetic axion insulator $MnBi_8Te_{13}$ that greatly extends the $MnBi_{2n}Te_{3n+1}$ (MBT) family. Chapters 5 discusses the effect of Sb doping in $MnBi_4Te_7$, which allows us to tune the magnetism and topology in a continuous and controllable way. The work emphasizes how antisite defects can modify the magnetism and topology in the $MnBi_{2n}Te_{3n+1}$ family. Chapter 6 focuses on the magnetic dynamics in the ferromagnetic members of the $MnBi_{2n}Te_{3n+1}$ family, including $MnBi_8Te_{13}$ and Sb-doped $MnBi_{2n}Te_{3n+1}(n = 2, 3)$, pointing to the important role of their very-soft ferromagnetism nature on the spin dynamics. In Chapter 7, I present our development of a new growth method of $MnBi_2Te_4$ via the chemical vapor transport. The comparison of the crystals grown by the flux method and chemical vapor transport method suggests the detrimental role of antisites in device applications of the material. Chapter 8 concludes the thesis and outlooks the ongoing research of $MnBi_{2n}Te_{3n+1}$ family and MTI in general.

1.2 Background on Hall effect and band topology

For the rest of this chapter, I will first review the history and previous development that have lead to the recent discovery of magnetic TIs and provided motivations to our studies. The notion of topology was first introduced in the condensed matter field to describe the

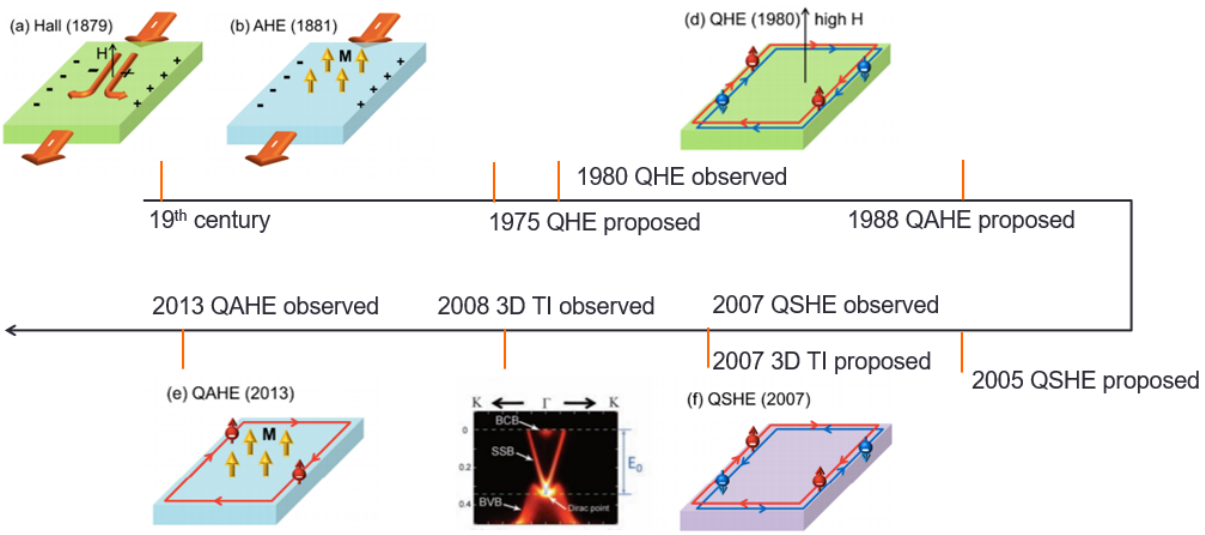

Figure 1.1: History of the discoveries of different types of Hall effects. Classic Hall effect, AHE, QHE, QSHE, 3D TI and QAHE in the chronological orders. Numbers in parentheses indicate the years of each discovery. H is the external magnetic field. M is the intrinsic spontaneous magnetization. S denotes spin. Adapted from [4, 5]

quantum Hall state, and later found to be closely linked to all types of Hall effects. Therefore, we will cover mostly the phenomenological aspects of various Hall effects, with the emphasis on the role of topology. We will then go over the theoretical formulations to provide the basis of the topology and magnetism. Finally we will summarize and outline a road map for the overall studies of topological materials.

Hall effect refers to the production of voltage difference transverse to the current direction. Today, physicists have discovered different types of Hall effects. Among them, there are three classical ones, including the ordinary Hall effect, spin Hall effect, anomalous Hall effect. Then there are three corresponding quantum versions, quantum Hall effect (QHE), quantum spin Hall effect (QSHE) and quantum anomalous Hall effect (QAHE). In Fig. 1.1 we show the timeline for the theoretical proposals and experimental realization of each type. The earliest discovery of the series dates back to 19th century while the last member QAHE was discovered less than 10 years ago.

1.2.1 Classical Hall effect

The classical Hall effect was first discovered in 1879 by Edwin Hall, whom the phenomenon is later named after. The Hall effect happens as a result of the classical electrodynamics in which the charge carriers are driven by the Lorentz force under magnetic field to accumulate at the edge of the sample and generate a voltage difference across the sample. The associated electric field is perpendicular to the current direction as well as the external magnetic field. Eventually the system enters an equilibrium, where the effect of magnetic field is eventually balanced by the induced electric field.

$$\mathbf{F} = q(\mathbf{E} + \mathbf{v} \times \mathbf{B}) = 0 \tag{1.1}$$

In this equilibrium, the sign and magnitude of Hall voltage is dependent on the charge carrier, so Hall effect is commonly used to determine the charge carrier type, as well as the carrier density using

$$V_H = \frac{IB}{nte} \tag{1.2}$$

In case of single carrier type, V_H is always proportional to B. If the sample is p-type, i.e. holes are the major carriers, $V_H(B)$ will have a positive slope. If it is n-type, i.e. electrons are the main carrier, $V_H(B)$ will have a negative slope. If we let the Hall resistivity be $\rho_{xy} = \frac{V}{It}$ then, the Hall coefficient can be defined as slope of $\rho_{xy}(B)$.

$$R_H = \frac{d\rho_{xy}}{dB} = 1/ne \tag{1.3}$$

Therefore, from the Hall coefficient, one can obtain the sign and value of n, and thus get the average carrier density and dominant carrier type. This method is commonly used in the transport studies of various materials.

1.2.2 Anomalous Hall effect

Following the discovery of Hall effect, it was found in ferromagnetic (FM) materials that ρ_{xy} is not just linear with the external field. In particular, there is a spontaneous jump of the Hall signal that matches the trend of the magnetization around zero field, which leads to

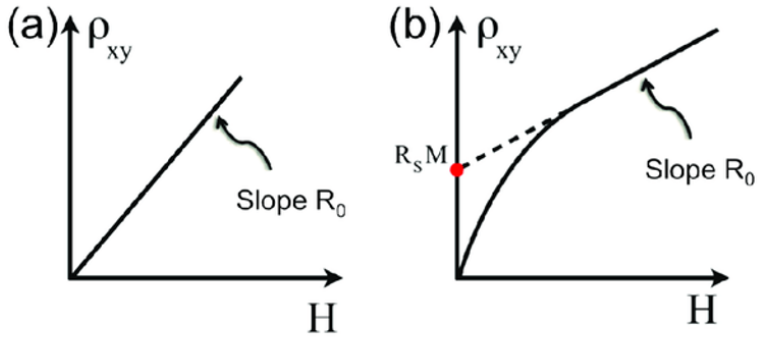

Figure 1.2: Comparison of ordinary Hall effect (a), and AHE (b). In (b), a linear interpolation of ρ_{xy} at high field yield a finite anomalous Hall resistivity proportional to the magnetization at 0 T.

a nonzero intercept at R_{xy}^A. Therefore, this type of Hall effect is named the anomalous Hall effect (AHE). Because the relative size of R_{xy}^A is generally proportional to the magnetization loop with $R_{xy}^A = R_S M$ for some constant R_S, as shown in Fig. 1.2, naively, it may seem that internal magnetic field provides the Lorentz force and results in AHE, just like what the external magnetic field does for non-magnetic materials. However, its microscopic mechanism turns out to be much more complicated than that. Today, it is believed that AHE is caused by a combination of extrinsic factors like asymmetric magnetic scattering and side jumps, as well as intrinsic factor from Berry curvature in the momentum space [6]. The intrinsic scenario is more of a topological origin, where the role of internal magnetism is to break the time reversal (TR) symmetry, and allows a nonzero integrated Berry curvature over the entire Brillouin zone in the reciprocal space. Moreover, in special cases where the magnetic moments are not coplanar, a moving charge carrier experiences similar interaction with the spin curvature in the real space, and gives rise to "topological Hall effect". The detailed role of symmetry to Berry curvature for a general magnetic material is discussed in Section 1.3.3 of this chapter.

1.2.3 Spin Hall effect

Spin Hall effect (SHE) was first proposed in 1970s [7] but only recent predictions in doped semiconductors like GaAs in this century [8,9] have lead to experimental observation [10]. In contrast to a typical Hall effect where there is a transverse charge current, in SHE, there is transverse spin current under a electric field. In a spin current, opposite spin carries opposite momentum.

Note that a charge current is odd but a spin current J^s is even under TR symmetry. This makes the SHE very different from the "charge" Hall effect. No external field is needed because SHE is TR-preserving. Here, the role of the external field is taken by the spin-orbit coupling in the system, which does not break TR symmetry but acts oppositely on opposite spins, and drives them to the opposite directions. Although SHE is not named "quantum", its intrinsic origin in spin-orbit coupling is very much quantum mechanical like AHE. It is similar to that of the later discovered quantum spin Hall effect, except here it is not quantized.

1.2.4 Quantum Hall effect

In 1970s, a quantized version of Hall effect was proposed in two-dimensioanl (2D) electron gas [13], and later observed in silicon-based MOSFET samples [14] which provided an interface environment for the electron to behave like a nearly ideal 2D gas. In this quantum Hall system, the Hall conductance becomes quantized with units of e^2/h under high field. Its Hall resistance forms several platforms at $R_{xy} = \frac{1}{n}\frac{h}{e^2}$ $(n = 1, 2...)$ where the longitudinal resistance R_{xx} becomes vanishing as shown in Figure 1.3. Physically, one can understand the phenomena by constructing the Hamiltonian for the systems under field. We start with non-interacting degenerate free electron gas constrained within the $x-y$ plane. If a magnetic field is applied along the z direction, then using Landau gauge potential $\mathbf{A} = By\hat{x}$, one can write down the Hamiltonian as

$$H = \frac{1}{2m}(p_x + \frac{eBy}{c})^2 + \frac{1}{2m}p_y^2 \tag{1.4}$$

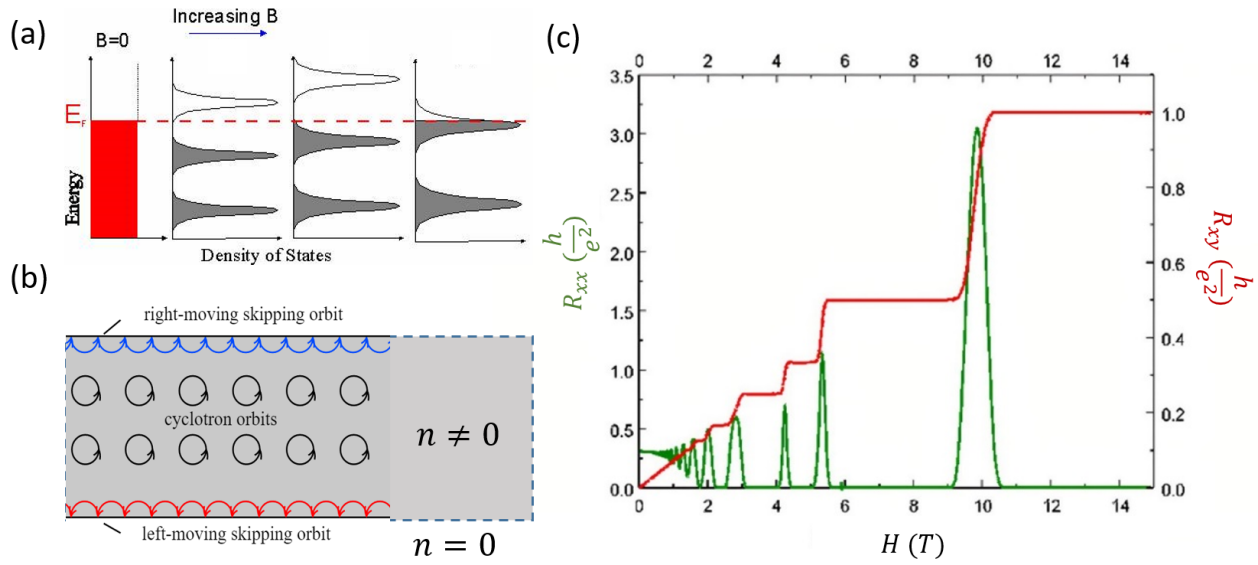

Figure 1.3: Quantum Hall effect: (a) Evolution of Landau levels under magnetic field. (b) Localized cycling electrons and the formation of chiral edge states between the topologically trivial and nontrivial states. (c) Transport behavior showing the quantized Hall resistance R_{xy} and vanishing longitudinal resistance R_{xx} at high field. Figures are adapted from Ref. [11, 12].

This can be solved by separating the variable x and y so

$$\psi(x,y) = \frac{1}{2\pi} e^{ikx} \phi(y) \tag{1.5}$$

Then we can write the Schrodinger equation for $\phi(y)$

$$[-\frac{\hbar^2}{2m}\partial_y^2 + \frac{1}{2}m\omega_c^2(y-y_0)^2]\phi(y) = E\phi(y) \tag{1.6}$$

Here $\omega_c = \frac{eB}{mc}$ and $y_0 = k\sqrt{\frac{\hbar}{m\omega_c}}$. One can note that the form is exactly that of the quantum harmonic oscillator. Therefore, the time-dependent solutions to the Schrodinger equation will take the form

$$\psi(x,y,t) = \frac{1}{2\pi} e^{i(kx-\omega_c t)} \Phi_n(y-y_0) \tag{1.7}$$

with the energies

$$E_n = (n+\frac{1}{2})\hbar\omega_c \tag{1.8}$$

This means by applying the magnetic field, we go from free electron obeying Dirac-Fermi statistics to quantized energy state with the energy gap of $\hbar\omega_c$ that is proportional to B. Therefore, with increasing B, landau levels will pass across the chemical potential. When the chemical potential lies in between two Landau Levels, the 2D electron gas becomes semi-conducting or insulating in bulk. When the nth Landau level crosses the chemical potential at a certain field, the sample can become conducting in bulk. This leads to a resistance behavior that is periodic with the inverse of the magnetic field B^{-1}. In a generic bulk metal or semimetal, this gives rise to quantum oscillation of magnetization or conductance with a periodicity in the inverse field.

For quantum Hall system, the bulk-insulating state also comes with a dissipationless conduction channel on the edge and the Hall conductance will be an integer multiple of e^2/h.

$$\sigma_{xy} = ne^2/hc \tag{1.9}$$

Semi-classically, we can understand the picture as electrons in the bulk entering localized cyclotron orbit due to strong external field as shown in Fig 1.3(b). The direction of the circulation, i.e. the chirality, depends on the sign of the charge and the magnetic field. For

2D free electron, when the chemical potential is in the gap of two neighboring landau levels, the bulk is insulating and thus electrons will be circulating locally. The only exception happens at the edge of the system, where the orbiting electron hits the boundary, bounces and continues to propagate along the 1D edge via skipping cyclotron orbits. Because the chirality of the edge conduction is fixed, the transport direction along a certain edge cannot be flipped. Therefore the edge transport is robust against any backscattering and becomes dissipationless. Note the protection from backscattering is inseparable from the insulating bulk because otherwise, the backscattered electron can travel across the bulk to be move backward.

One unique feature of QHE state is that it is no different from a typical band insulator in terms of symmetry. The transition from trivial state at a low field to a quantum Hall state at a high field, or from one Hall plateau to another, cannot be characterized by any broken symmetry. To fully describe the physics, one must now introduce the notion of topology. Here, each quantized plateau in Hall data is associated with a unique topological invariant called Chern number, which equals the value n in the Hall conductance $\sigma_{xy} = ne^2/h$. The skipping orbits, or, chiral edge states occur as the Chern number is nonzero. We shall discuss about the significance of the topological numbers and how to obtain them in Section 1.3.

1.2.5 Quantum Spin Hall effect

Following the QHE and classical SHE, the Quantum spin Hall effect (QSHE) was first proposed in 2005 [16, 17]. It can be thought as superposing a pair of dissipationless edge states, i.e., the chiral edge states with opposite spin, opposite propagation direction, opposite Chern number and opposite chirality, as shown in Fig. 1.4. This separation of the spin-up and spin-down charge edge states can be realized in materials with inverted band structure that is driven by strong spin-orbit coupling (SOC). The pair can be related by time reversal operation. Each state is similar to that of the quantum Hall state but with opposite Chern number. Then overall the time reversal symmetry is still preserved and the Chern number is 0. Since its Chern number is zero, additional topological number $\mathbb{Z}_2$ is necessary to define

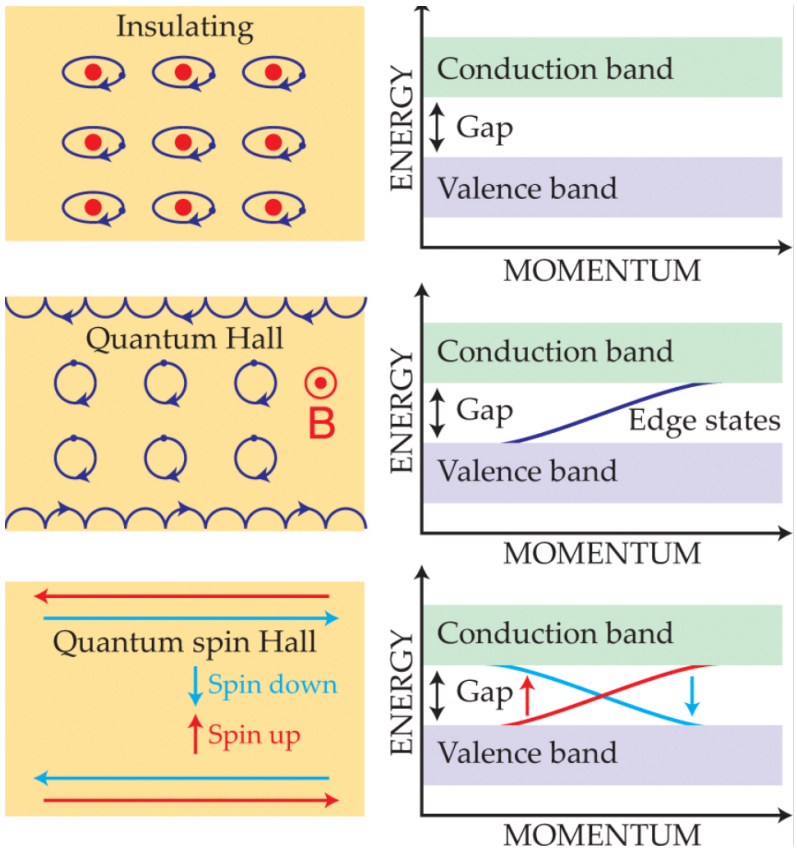

Figure 1.4: Comparison of electronic states with different topology. In trivial insulators (top), all electrons are localized. A gap is present at all values of momentum. In the QHE (middle), an external magnetic field pins the electrons and opens a bulk gap. Within the gap are the edge states which carry dissipationless current. In the QSHE (bottom), a bulk gap is always present. The helical edge states consists of two chiral states that cross the gap and carry counter-propagating currents of spin-up and spin-down electrons. Taken from Ref [15].

the QSHE state. The definition and mathematical formulations of $\mathbb{Z}_2$ will be talked about in Section 1.3.5 of the chapter.

Like in QHE, the bulk of QSHE is insulating and the edge conduction is also dissipationless. Although electrons are allowed to travel on both edges, electrons with each spin state can only travel in one direction due to the strong SOC in the system. To reverse the propagating direction of one electron, it must flip its spin, which is forbidden under TR symmetry. The opposite-chirality edge states are the Kramer's degenerate for each other. Kramer's degeneracy theorem states that for every energy eigenstate of a TR symmetric system with half-integer total spin, there is at least one more degenerate eigenstate. T is an anti-unitary operator. For integer angular momentum, $T^2 = 1$. However, for half-odd-integer angular momentum, it satisfies $T^2 = -1$, which implies the presence of degenerate state. In particular, the matrix elements of a TR-invariant perturbation between two Kramer's degenerate vanish identically, so any backscattering or hybridization between the spin-up and spin-down states are forbidden. Therefore, the dissipationless edge conduction in QSHE is protected by TR symmetry. From the energy band point of view, Kramer's theorem also requires the crossing of the edge state to occur at high-symmetry point in the Brillouin zone, so as shown in Fig. 1.4 (f), two 1D Dirac bands that corresponds to the helical edge stats cross each other at $k = 0$.

Since SOC-driven band inversion is important to realize QSHE, QSHE was found in materials made of heavy elements where SOC are stronger due to large effective nuclear number. The nuclei of heavier elements carry a larger charge and effectively induces a larger magnetic field that caused a splitting of the opposite spin states of the electrons. One necessary condition for QSHE is that SOC needs to be large enough to invert the usual ordering of valence and conduction band. [18] Experimentally, QSHE was first observed in CdTe-HgTe-CdTe 2D quantum well, where the SOC in the HgTe layer is thickness dependent. Below a critical thickness of 6.5nm, SOC was relative weak so no band inversion in this quantum well. When HgTe becomes thicker than 6.5nm, a band inversion occurs between Hg-6s and Te-5p orbitals, allowing QSHE to occur. Indeed, a quantized longitudinal conduction

of $2h/e^2$ from the helical edge states was observed in the absence of external magnetic field when the chemical potential is tuned to the band gap [19].

1.2.6 Topological Insulator

Following QSH state, which now we know is the 2D version of topological insulator, the notion of 2D insulating bulk with dissipationless 1D conducting edge can be generalized into higher dimensions, e.g. 3D bulk with 2D surface. One simple thought-experiment is to realize this is to stack N numbers of QSH insulators on top of each other. Then certain side surfaces will host N pairs of conducting edge state. Now the side surface will be conductive, while the bulk of the sample remains insulating. In 2007, this generalization to 3D is mathematically formulated to a general 3D bulk material, called topological insulator.

The 3D topological insulator are described by four $\mathbb{Z}_2$ invariant $(\nu_0; \nu_1, \nu_2, \nu_3)$, where ν_0 is the strong topological invariant, and ν_1, ν_2 and ν_3 are the weak topological invariants. If $\nu_0 = 0$, but $\nu_1 + \nu_2 + \nu_3 \neq 0$, then the system is called weak topological insulator. The fore-mentioned model of stacked 2D QSH insulator is an example of weak TIs, where protected surface states only exist on certain surface terminations. If $\nu_0 = 1$, the system is called strong topological insulator where all surface states are topologically protected. Otherwise, if all $\nu_i = 0$, then the system is topologically trivial like a regular band insulator.

Band-structure-wise, from 2D to 3D, the two 1D Dirac bands for the helical edge states evolve into a continuous Dirac cones for the surface states. Such Dirac cones can be described mathematically by the Hamiltonian as

$$H = v_F(-k_y\sigma_x + k_x\sigma_y) \tag{1.10}$$

Here, v_F is the Fermi velocity of the linear dispersion and σ_i is the Pauli matrices for spin. The Hamiltonian suggests the spin-momentum locking of the massless Dirac electrons, which means, electrons carrying opposite spins travel in opposite directions like in 2D QSHE. The surface states in TIs are not spin degenerate except at the Dirac point. Because the states at momenta $\boldsymbol{k}$ and $-\boldsymbol{k}$ have opposite spins, the spin must rotate with $\boldsymbol{k}$ around the Dirac cone.

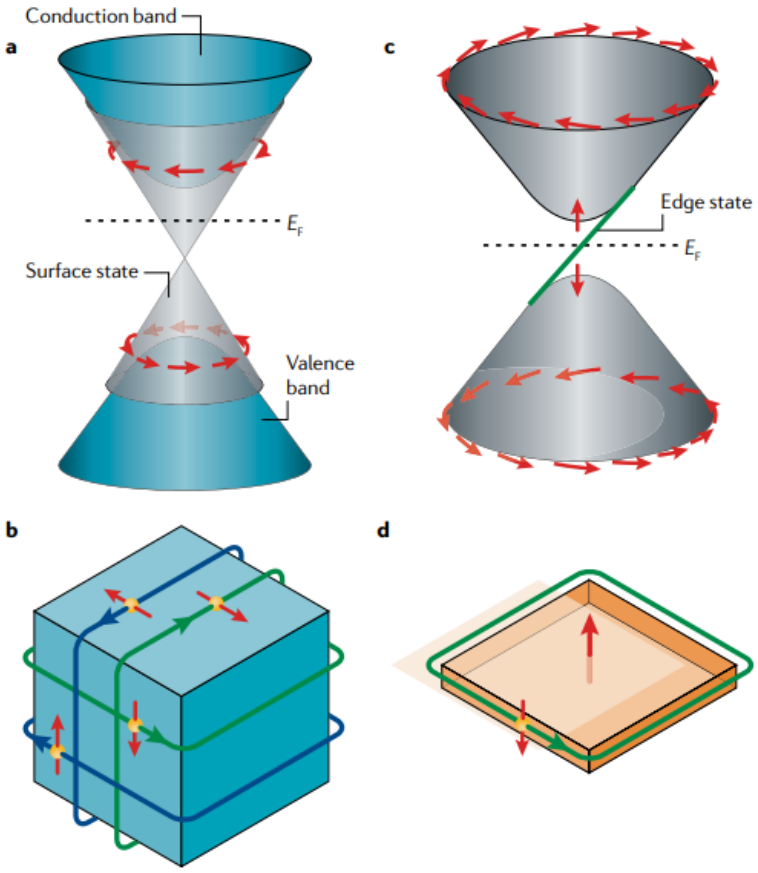

Figure 1.5: The electronic structure of a 3D TI and of a MTI at its 2D limit, taken from Ref [3]. (a) The massless Dirac-like dispersion of the surface state with spin–momentum locking in a TI. The spin-locking surface state band connects the bulk valence and the bulk conduction bands. (b) Real-space picture of the surface state in a TI. Electrons with opposite spins move in opposite directions. (c) The Dirac-like dispersion of the edge state in a 2D MTI that connects the surface states gapped due to the magnetism. (d) The chiral edge mode that becomes apparent in a 2D MTI device when the Fermi level is located in the surface gap. The electrons conduct electricity without dissipation in one direction along the edge.

If the Fermi energy lies between the bulk gap, it leads to a nontrivial Berry phase acquired by an electron going around the Fermi surface like in Fig. 1.5 (a). TR symmetry requires that this phase be 0 or π. When an electron circles a Dirac point, its spin rotates by 2π, which leads to a π Berry phase. The Berry phase as well as the linear band dispersion (in comparison to generally parabolic ones) can be detected by quantum oscillations in transport studies.

In TI, the Dirac surface states are too protected by the TR symmetry. The bulk conduction and valence bands needs to be inverted and gapped by SOC. The most direct experimental evidence of TI is the band structure measured through ARPES and confirmed by DFT calculations. In Fig. 1.6, we show the band structure in TI Bi_2Te_3 and related compounds [20]. Among the four sister compounds, Sb_2Se_3 has the lightest atoms, so the SOC is too weak to drive the band inversion. With a stronger SOC in Bi_2Te_3, the bulk bands of Te $5p$ and Bi $6p$ are inverted around Γ point, likewise in Sb_2Te_3 and Bi_2Se_3. In between the gapped bulk band, one can clearly see the surface states with the Dirac cones for the Sb_2Te_3, Bi_2Se_3 and Bi_2Te_3.

It is important to note that a generic 3D TI itself does not show any quantized transport behavior. Intuitively, one can think of the Dirac cones as infinitely many degenerate Dirac bands in QSHE. They altogether give the conducting surfaces. The surface conduction is therefore a combined effects of all of the helical edge states which will not be quantized. Conversely, one can theoretically reduce the TI dimension to 2D, back to 2D QSHE, to access the quantized transport behavior.

1.2.7 Quantum anomalous Hall effect

Quantum anomalous Hall effect is the last of the quantum Hall family to be discovered. However, its earliest proposal dates back to 1988. In his work [21], Haldane predicts that the QHE can be realized in a graphene lattice with alternating magnetic field in the neighboring atom. Because the TRS is broken by the spatially varying magnetic field, quantized Hall resistance with Chern number 1 can be realized without the formation of landau levels. In

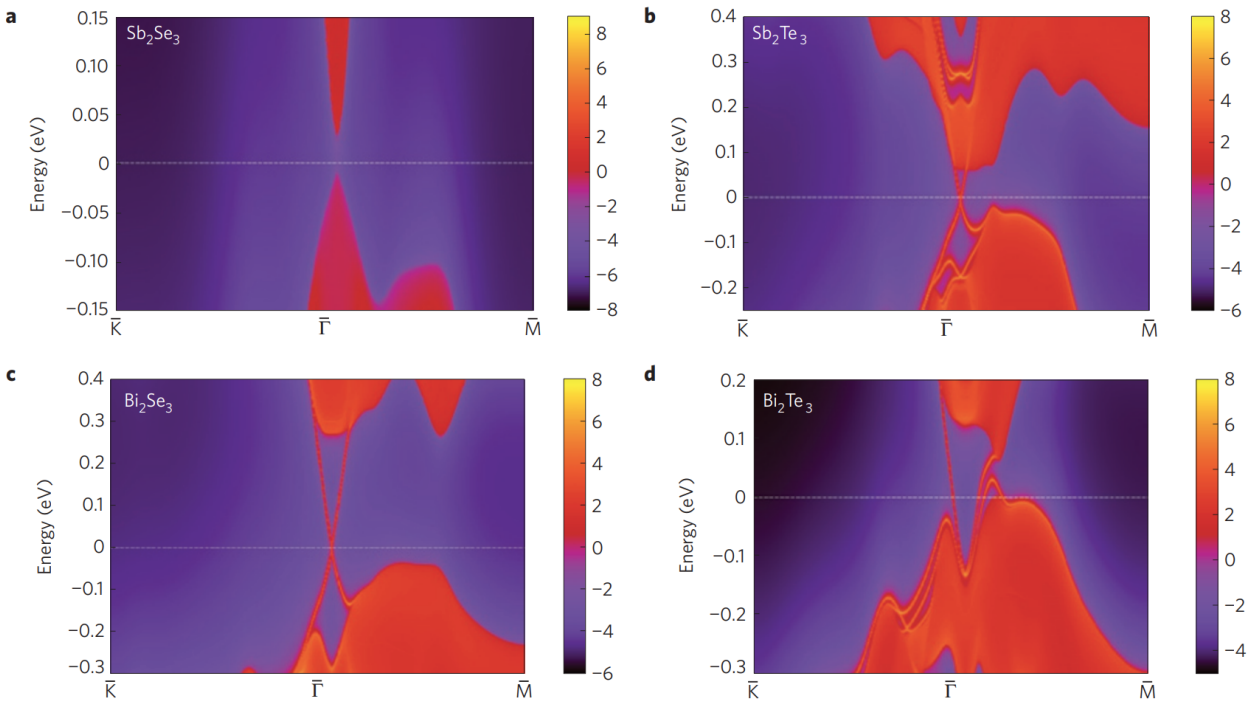

Figure 1.6: Band structures of Sb_2Se_3 (a), Sb_2Te_3 (b), Bi_2Se_3 (c) and Bi_2Te_3 (d) on the [111] surface. Here, the warmer colours represent higher local density of states. The red regions indicate bulk energy bands and the blue regions indicate bulk energy gaps. The surface states can be clearly seen around the Γ point as red lines dispersing in the bulk gap for Sb_2Te_3, Bi_2Se_3 and Bi_2Te_3. No surface state exists for Sb_2Se_3. Taken from Ref [20].

practice, however, such a system is experimentally difficult to achieve.

It was not until the discovery of 3D TI that QAHE was re-proposed to exist in magnetic topological insulators (MTI). Without magnetism, TI has a bulk gap induced by SOC and gapless Dirac surface states which is protected by the TRS (Figure. 1.5). When we make a TI into 2D limit, and introduce magnetism, because the TR symmetry is broken, the topological surface state is no longer protected. Electrons on the surface states will couple with the spontaneous magnetization. Assuming the magnetization is along z, the revised Hamiltonian for the Dirac surface states based on Eqn. 1.10 can be written as

$$H = v_F(-k_y\sigma_x + k_x\sigma_y) + m\sigma_z \tag{1.11}$$

Such interaction causes the opening of a mass gap m at the Dirac point, so the Dirac surface state is no longer massless. Nevertheless, within the gap, there is a chiral edge state similar to that in the QHE. For nonmagnetic TIs, the sample is insulating in the bulk and conducting in the surface if the Fermi level is in within the bulk gap. The topological state is characterized by the $\mathbb{Z}_2$ coefficients. Now for MTI, if the Fermi level is tuned within the surface gap, then both the bulk and the surface will be insulating, but there is a dissipationless conduction along the sample edge. The topological state is characterized by the Chern number of ± 1, so there will be quantized Hall conductance like in QHE. The directions of the edge conduction in real space and the band in the reciprocal state depend on the magnetic interaction.

Experimentally, this could be done by introducing magnetic atoms into existing topological insulator such as Bi_2Te_3. This was first realized through Cr-doped $(Bi/Sb)_2Te_3$ thin films grown by molecular beam epitaxy (MBE) on $SrIrO_3$ [22] in Figure 1.7. When the gating voltage is tuned at the charge neutrality at -1.5 V, at dilution fridge temperature of 30 mK, the Hall resistance R_{xy} reaches a quantized value of h/e^2 with a considerable drop in R_{xx} signaling the dissipationless edge transport. When gating voltage moves the Fermi level away from the gap, the behavior vanishes.

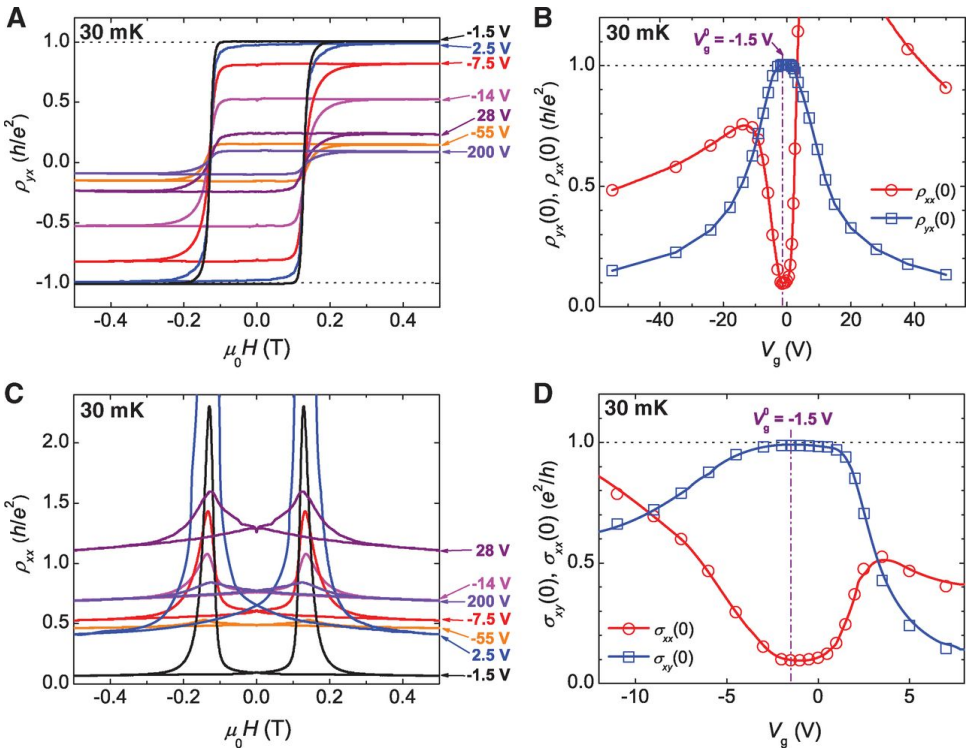

Figure 1.7: The first observation of QAHE in $Cr_{0.15}(Bi_{0.1}Sb_{0.9})_{1.85}Te_3$ thin film. (A) Magnetic field dependence of ρ_{yx} at different gating voltage V_g. (B) Dependence of ρ_{yx} and ρ_{xx} on V_g at zero field and 30 mK. (C) Magnetic field dependence of ρ_{xx} at different V_g. (D) Dependence of σ_{xy} and σ_{xx} on V_g at zero field and 30 mK. [22]

1.2.8 Beyond the quantum Hall family & TI

Many technological advances have been proposed based on these systems since the prediction and the discovery of the quantum Hall family. In addition to the novel quantized or dissipationless transport, the quantum Hall family has many practical applications in other aspects like optics. For example, one can realize some exotic electromagnetic response resulting from the unique boundary condition these topological systems. Specifically, just like a point charge above a metal surface can cause an image charge within the metal, a point charge above a 3D TI coated by a thin FM layer leads to an image magnetic monopole within the TI. Such electron-monopole composites, called dyons, follows fractional statistics [23,24].

When coupled with superconductors, topological insulators can also host another type of quasi-particle called anyons that follow non-Abelian statistics, i.e.

$$|\psi_1, \psi_2 >= e^{i\theta}|\psi_2, \psi_1 > \tag{1.12}$$

Generally, θ would be 0 for bosons and π for fermions. Yet for anyons it can be neither, so the exchanging two anyons could lead to additional states useful for fault-tolerant computational purpose. As such, braiding, creation, annihilation of anyon pairs form basic component for topological quantum computing. Majorana zero mode (MZM) is one candidate of anyons. These quasiparticles are their own antiparticles. They can be realized as the superconducting vortices on the surface of a 3D TI coated with a thin s-wave superconductor. [25,26] Likewise, QAH or QH system in proximity with s-wave superconductor was proposed to host MZM on the edge, in which the Majorana particles are localized at the two ends of the 1D conducting edge. Such a MZM on edge allows interferometer measurement to have a smoking-gun evidence of nonabelian statistics [27–29]. Finally, the induced SC at QAH edge by nature is chiral topological superconductivity, where many interesting physics await exploration [30, 31]. Since QAHE requires no external field, the experimental search of all above are mostly based on QAHE instead of QHE. To that end, the realization of material platforms which can host high temperature QAHE state is strongly urged and incessantly being pursued in many works in the field including this thesis.

Axion insulator is the last topological state relevant to this thesis. Axion is a particle proposed in quantum chromodynamcis to solve the charge-parity problem of the strong nuclear force [32, 33]. It is today also one of the candidates of dark matter in the universe. Axions couple to electromagnetism by adding an additional term $L_\theta \propto \mathbf{E}\cdot\mathbf{B}$ to the Lagrangian of electrodynamics. As a result of such a coupling, in the presence of a magnetic field $\mathbf{B}$, the axion creates an electric field $\mathbf{E}$ in the same direction and vice versa, in which case axion-photon conversion may be observed in principle.

In condensed matter, axions can be found as quasiparticles in magnetic topological insulator. The host system is named axion insulator for being able to host topological magnetoelectric effect (TME), where an electric field induces a magnetization along the same direction with a universal constant α. In particular, α is quantized in odd multiples of the fine-structure constant, i.e.

$$\alpha = \frac{\partial M}{\partial E} = \frac{\partial P}{\partial B} = \frac{e^2}{h}\frac{\theta}{2\pi} \tag{1.13}$$

θ takes the value of π for axion insulator and 0 for trivial cases [24, 34, 35]. For example, the net magnetization would be

$$\boldsymbol{M_t} = -\frac{1}{2}\frac{e^2}{hc}\boldsymbol{E} \tag{1.14}$$

Since $\theta = \pi$, the experimental signature for an axion insulator is that the top/bottom surface each shows a half-Chern number i.e. a half quantized Hall resistance, if they are fully gapped,

$$\boldsymbol{j}_H = \frac{1}{2}\frac{e^2}{h}\hat{\boldsymbol{n}} \times \boldsymbol{E} \tag{1.15}$$

In terms of band structure, a 3D axion insulator has insulating 3D bulk and 2D surface states. The half-Chern number at the top and bottom surface are carried by the 1D hinge states along the hinges. Therefore, 3D axion insulator can be regarded as a higher order topological state. [36–38](In comparison, a $C = 1$ QAHE is defined for 2D system which has conducting edge states and insulating surface.) The signature of $\theta = \pi$ in axion insulator can actually be captured by another topological invariant $Z_4 = 2$, which will be discussed in section 1.3.6.

1.3 Theoretical Formulations for topology

1.3.1 Topology in Condensed Matter system

Throughout the proposal and the discovery of QHE, QSHE, TI and QAHE, one important insight is the notion of topology. Generally, the state of matter is classified according to the symmetries breaking/forming. For example, a solid-to-fluid transition is one that breaks translation symmetry by removing the periodic lattice order. However, no such symmetry breaking can be associated with the onset of QHE state and other quantum-type Hall states. As we have seen, each type of quantum-type Hall effect is characterized by some topological numbers. In fact, since the discovery of QHE, today topology has become a new and important standard to classify matter.

Why topology? Mathematically, topology refers to the robust properties of a geometric object that are preserved under continuous deformations. For example, this robust property can be the number of holes inside. Then the local perturbations to the object such as stretching, twisting does not affect the topological properties, as long as it does not involve creating/closing holes, tearing apart, etc. For example, the letter 'D' on a plane can be continuously deformed into 'P', but not 'B' nor 'M'. A donut in 3D space has a closed surface, which can be continuously deformed into a mug without enclosing the hole, but not into a sphere or a pretzel. In geometry, the number of holes for a closed surface is directly related to a topological invariant called Euler characteristic χ. It can be calculated by integrating the Gaussian curvature everywhere at the surface K,

$$\frac{1}{2\pi}\oiint KdS = \chi \tag{1.16}$$

For any shape of 3D object with a closed surface, $\chi = 1 - n$, where n is just the number of hole. Since both n and χ have to be an integer, they cannot change continuously. Only under a large deformation that creates or remove the holes, will the topological number χ change. In this case, we call the change of matter/geometric state a topological transition. The n or χ then allows one to classify different objects geometrically. Objects with the same topological invariant χ, like a donut and a mug, are called topologically equivalent. Today in

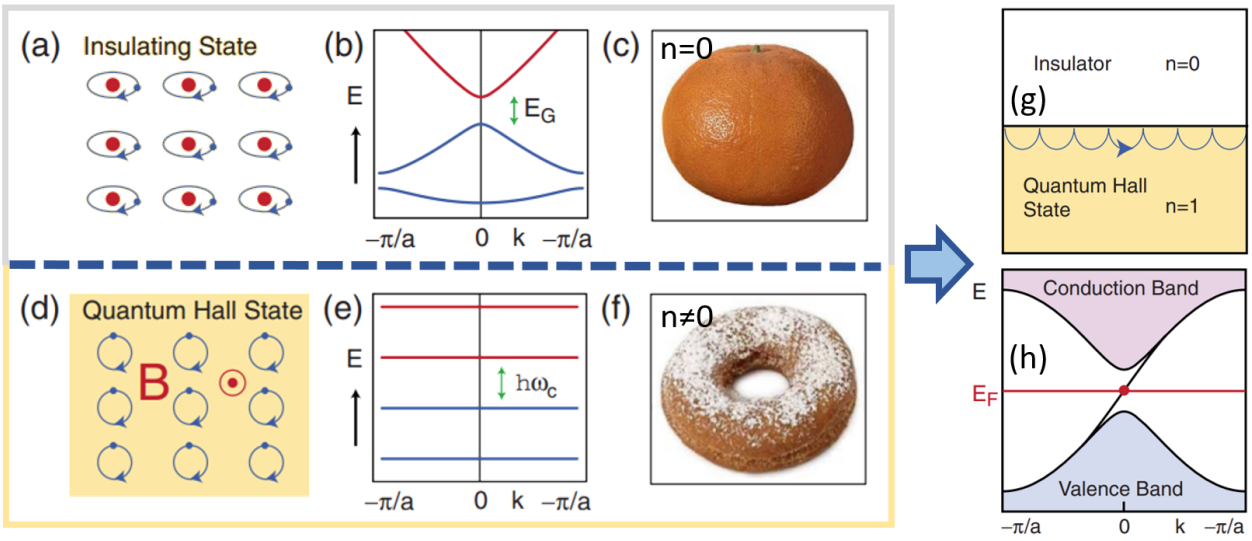

Figure 1.8: Two states of matter characterized by Chern number. Top-left panel: (a) A trivial insulating state with localized electrons and $n = 0$ in real space. (b) Characteristic band structure of (a) in reciprocal space. (c) Orange is the geometric analog of (a) since there is no hole in the orange and thus $n = 0$. Bottom-left panel: (d) The quantum Hall state with $n \neq 0$ and localized cyclotron orbit in the bulk in real space. (e) Characteristic band structure of (d). (f) Donut is the geometric analog of (d) since there is a hole in the donut and thus $n \neq 0$. (g)-(h): Bulk-boundary correspondence in QHE. (g) Real space picture. The chiral edge mode lies at the interface between a quantum Hall state and a trivial insulator. It appears as the skipping cyclotron orbits in the real space. (h) Reciprocal space picture. A single edge state connecting the valence band to the conduction band. Adapted from Ref [1]

physics, topology is of central importance in many fields. Before it gained popularity in the condensed matter field, the notion was first applied to particle physics, e.g. for the theoretical proposal of magnetic monopole, and quantum field theory, in order to study systems with singularities (vortices) where the vector fields like electromagnetic fields become undefined. The discovery of QHE and the topological invariant Chern number marks its entry to the field in modern condensed matter. In Figure 1.8, a parallel is drawn between topological systems in condensed matter and in real life. The different Chern number in the trivial insulator and QHE system means the two systems are topologically distinct, just like the donut and the orange. For our studies, we are mainly looking at three types of topological invariants. They are Chern number C for QHE and QAHE, $\mathbb{Z}_2$ coefficient(s) ν for QSHE or $(\nu_0; \nu_1, \nu_2, \nu_3)$ for 3D TI, and finally Z_4 coefficient describing the TR-breaking higher-order topological systems.

One common and remarkable feature of the topological state is the *bulk-boundary correspondence*. The bulk and boundary for 2D systems are the surface and the edge, respectively. For 3D TI, they refer to the bulk and the surface of the sample, re. In general, it is the n-dimensional bulk and $n-1$-dimensional boundary. The bulk-boundary correspondence requires the presence of gapless edge state in all the topological phases we have discussed. This happens because of the discontinuity of the topological number across the boundary between the topologically trivial and nontrivial phases. For this reason, these surface/edge states on the boundary are called topologically protected. In 3D nonmagnetic topological insulators, the bulk-boundary correspondence leads to the well-known topologically protected gapless surface state; In 2D electron gas, the bulk gaps that are opened either by broken TR symmetry for QHE and QAHE or by strong SOC for QSHE, have to close at the boundary, leading to chiral or helical edge state, as shown in Figure 1.8 (g-h).

In general, the number of edge states at the boundary is a reflection of difference in topological invariant between the phases. At the interface between two phases with different Chern numbers N_L and N_R respectively, for example QAH insulator (C=1) and vacuum

(C=0), the number of chiral edge states can be described as

$$n = N_R - N_L \tag{1.17}$$

and each edge state will correspond to one quantized Hall conductance.

For QSHE in 2D systems with the topological invariant $\mathbb{Z}_2$, one can also get a similar relationship to get the number of helical edge state pairs. Again, the formalism suggests there can be only one pair of such helical states, and it only occur between a topologically trivial phase ($Z_2 = 0$) and a nontrivial phase ($Z_2 = 1$).

$$n = (\nu_R - \nu_L) \bmod 2 \tag{1.18}$$

1.3.2 Berry Phase and Berry Curvature

One characteristics that connects between band structure and topology is the notion of Berry curvature. It derives from the Berry phase and serves as an essential building block to understanding topological phenomena and relevant ones such as anomalous Hall effect.

The concept of the Berry phase is defined in the adiabatic evolution of a non-degenerate eigenstate when the system evolves in the parameter space but returns to itself, effectively making a loop in the space. The eigenstate $|n(\boldsymbol{R(0)}>$ will stay the same but up to a different phase, which is the time integral of the energy over $\hbar$ plus the Berry phase.

$$|\psi_n(t)>= e^{i\gamma_n(t)} \exp\left[-\frac{i}{\hbar}\int_0^t dt' \epsilon_n(\boldsymbol{R}(t'))\right] |n(\boldsymbol{R}(t))> \tag{1.19}$$

The first exponent in the above equation is the Berry phase or geometric phase, whereas the second exponent in the bracket is known as the dynamic phase factor. In particular, Berry shows that along the closed loop the Berry phase can be nonzero, and is independent of the variation of the path $\boldsymbol{R}(t)$ in time but dependent on the overall geometric aspect of the path. It can be extracted by taking the equation 1.19 into time-dependent Schrodinger equation and left multiply by $< n(\boldsymbol{R(t)})|$. Then one would get

$$\gamma_n = \int_C d\boldsymbol{R} \cdot A_n(\boldsymbol{R}) \tag{1.20}$$

, where

$$A_n(\boldsymbol{R}) = i < n(\boldsymbol{R})|\frac{\partial}{\partial \boldsymbol{R}}|n(\boldsymbol{R}) > \tag{1.21}$$

is called the Berry connection, or Berry vector potential. As an analogy to the magnetic vector potential in the electrodynamics, one can define a gauge-field tensor from the Berry vector potential. In 3D, this can be written as the same vector form as the magnetic field in electrodynamics. The term is the Berry curvature.

$$\boldsymbol{\Omega}_n(\boldsymbol{R}) = \boldsymbol{\nabla}_{\boldsymbol{R}} \times \boldsymbol{A}_{\boldsymbol{n}}(\boldsymbol{R}) \tag{1.22}$$

Similarly, the Berry phase can adopt a similar formalism as the magnetic monopole, whose existence itself is yet to be found.

$$\gamma_n = \int_S d\boldsymbol{S} \cdot \Omega_n(\boldsymbol{R}) \tag{1.23}$$

In general, Berry curvature integrated over a closed manifold S is quantized to the units, and the quantization depends on the number of monopoles inside.

For systems mostly studied in condensed matter, i.e. crystals with periodic boundary conditions, the parameter in which the eigenstate evolves is the momentum space or the Brillouin zone. The eigenstates can be written according to Bloch's theorem as

$$\psi(\boldsymbol{r}) = e^{i\boldsymbol{k}\cdot\boldsymbol{r}} u_{\boldsymbol{k}}(\boldsymbol{r}) \tag{1.24}$$

Here k is the crystal momentum. $u(\boldsymbol{r}) = u(\boldsymbol{r} + \boldsymbol{a})$ for some Bravais lattice vector of the crystal $\boldsymbol{a}$. Then for a closed path C in the Brillouin zone, one can define the Berry phase for some Bloch state to be

$$\gamma_n = \oint_C d\boldsymbol{q} \cdot < u_n(\boldsymbol{q})|i\boldsymbol{\nabla}_{\boldsymbol{q}}|u_n(\boldsymbol{q}) > \tag{1.25}$$

Likewise, the Berry curvature at each point of the band is defined as

$$\Omega_n(\boldsymbol{q}) = \boldsymbol{\nabla}_{\boldsymbol{q}} \times < u_n(\boldsymbol{q})|i\boldsymbol{\nabla}_{\boldsymbol{q}}|u_n(\boldsymbol{q}) > \tag{1.26}$$

Note, the Berry curvature $\Omega_n(\boldsymbol{q})$ is an intrinsic property of the band structure that depends only on the wavefunction $|u_n(\boldsymbol{q}) >$. The notion of a closed loop is not needed for Berry

curvature since it is only a local gauge-invariant quantity. For this reason, it can be reflected in the transporting electrons. For example, for a moving electron driven by a perturbative external electric field, the velocity can gain an additional anomalous term so it becomes

$$\boldsymbol{v}_n(\boldsymbol{q}) = \frac{\partial \epsilon_n(\boldsymbol{q})}{\hbar \partial \boldsymbol{q}} - \frac{e}{\hbar}\boldsymbol{E} \times \boldsymbol{\Omega}_n(\boldsymbol{q}) \tag{1.27}$$

The second velocity term is perpendicular to the electric field. Hence phenomenologically, the effect of nonzero Berry curvature resembles that of an additional magnetic field in crystal systems. Using Eqn. 1.27, one can obtain the Hall conductivity of the system as integration of some components of Berry curvature in the Brillouin zone. For electron in 3D system,

$$\sigma_{xy} = \frac{e^2}{\hbar}\int_{BZ}\frac{d^2k}{(2\pi)^2}\Omega_{k_xk_y} \tag{1.28}$$

1.3.3 Role of Symmetries

The effect of Berry curvature on physical properties are very much related to the crystal symmetry and the associated symmetry requirement on the band structure. In fact in most systems, the overall effect of the Berry curvature is cancelled out or has to be zero due to the symmetry in the electronic band structure. Under time reversal (TR), $\boldsymbol{v}_n$ and $\boldsymbol{q}$ both flip signs. Therefore, to satisfy the Eqn. 1.27 under TR operations in TR symmetric systems, it must requires that

$$\boldsymbol{\Omega}_n(-\boldsymbol{k}) = -\boldsymbol{\Omega}_n(\boldsymbol{k}) \tag{1.29}$$

Under inversion operation, $\boldsymbol{v}_n$, $\boldsymbol{q}$ and $\boldsymbol{E}$ all change their signs. Then in inversion symmetric system, Eqn. 1.27 requires

$$\boldsymbol{\Omega}_n(-\boldsymbol{k}) = \boldsymbol{\Omega}_n(\boldsymbol{k}) \tag{1.30}$$

Therefore, the Berry curvature must vanish for system with both TR and inversion symmetries. Other symmetries such as mirror and rotation can also impose a restriction on all or some vector components of Berry curvature. A more extensive list of symmetry and Berry curvature can be found in the Table 1.1.

It becomes interesting, then, when one or more of the symmetries become missing to induce the nonzero Berry curvature. Here is the general rule of thumb. If for some crystal

Table 1.1: Common symmetry operations in crystals and their imposed requirements on Berry curvature.

Symmetry Operation	Symbol	Transformation on $\boldsymbol{r} = (x, y, z)$	Effect on $\boldsymbol{\Omega}(\boldsymbol{k})$
Translation	$t_{\boldsymbol{d}}$	$\boldsymbol{r} \longrightarrow \boldsymbol{r} + \boldsymbol{d}$	$\boldsymbol{\Omega}(\boldsymbol{k})$ unaffected
Rotation	C_n	$\boldsymbol{r} \longrightarrow C_n\boldsymbol{r}$	$\boldsymbol{\Omega}(\boldsymbol{k}) = \boldsymbol{\Omega}(C_n\boldsymbol{k})$
Inversion	P	$\boldsymbol{r} \longrightarrow -\boldsymbol{r}$	$\boldsymbol{\Omega}(\boldsymbol{k}) = \boldsymbol{\Omega}(\text{-}\boldsymbol{k})$
Mirror in xy plane	M_z	$z \longrightarrow -z$	$\boldsymbol{\Omega}^z(\boldsymbol{k}) = \boldsymbol{\Omega}^z(\text{-}\boldsymbol{k})$
Time Reversal	T	$\boldsymbol{r}$ unaffected, $t \longrightarrow -t$	$\boldsymbol{\Omega}(\boldsymbol{k}) = \text{-}\boldsymbol{\Omega}(\text{-}\boldsymbol{k})$

symmetry R there is $\boldsymbol{\Omega}(R\boldsymbol{k})$=$-\boldsymbol{\Omega}(\boldsymbol{k})$, Berry curvature at $R\boldsymbol{k}$ and $\boldsymbol{k}$ will be cancelled in the integration overall Brillouin Zone and gives overall zero AHE. Conversely, in order for Berry curvature to be not canceled by itself, one must break the symmetry R. For many systems, R is simply the TR symmetry. It can be broken by magnetic field or ferromagnetic order. Although AFM breaks TR symmetry as well, but $R = Tt_{\boldsymbol{d}}$ for certain translation $\boldsymbol{d}$ is invariant in many AFM materials and leads to the vanishing of Berry curvature. However, if one can break inversion symmetry, e.g. noncentrosymmetric systems with collinear AFM like RuO_2 and $CrNb_3S_6$ [39,40] where the net magnetization is close to zero under magnetic field, the integrated Berry curvature can still be nonzero. In noncollinear magnet such as Mn_3Ir [41], such symmetry is TM, which can be broken by in plane magnetic field and the spin-orbit coupling, giving rise to a finite anomalous Hall effect.

1.3.4 Chern number

Next, we will go through the mathematical formulations to obtain the topological invariants. From Eqn. 1.28, one can quickly draw a comparison to the Hall conductance of the QHE $\sigma_{xy} = ne^2/h$. Therefore the Chern number, n, can be directly derived from the Berry curvature integrated over a closed manifold,

$$n = \int_{BZ} \frac{d^2k}{(2\pi)^2} \Omega_{k_x k_y} \tag{1.31}$$

The same could also be employed when magnetism is introduced in topological insulator and gives rise to QAHE. Then for a 2D Dirac band with finite magnetization, we can rewrite the Hamiltonian n Eqn. 1.11 as $H = \boldsymbol{R} \cdot \boldsymbol{\sigma}$ for $\boldsymbol{R} = (-v_F k_y, v_f k_x, m)$. The Chern number in this case can be calculated by

$$n = \int_{BZ} \hat{\boldsymbol{R}} \cdot (\frac{\partial \hat{\boldsymbol{R}}}{\partial k_x} \times \frac{\partial \hat{\boldsymbol{R}}}{\partial k_y}) \frac{dk_x dk_y}{2\pi} = sgn(m) \tag{1.32}$$

, where $\hat{\boldsymbol{R}} = \frac{\boldsymbol{R}}{|\boldsymbol{R}|}$, and the cross product corresponds to the Berry curvature of the band in this particular case. The integration overall gives a winding number of $C = \pm 1$ and the sign depends on the sign of the exchange coupling term.

1.3.5 $\mathbb{Z}_2$ invariant

There are several formulations for $\mathbb{Z}_2$. One intuitive way is to calculate the Chern number for each spin channel [16, 42, 43]. If one can calculate n_u and n_d as the Chern number in up and down spin channels respectively, which satisfy $n_u + n_d = 0$ due to TR symmetry, then it follows that $Z_2 = (n_u - n_d)/2 \bmod 2$. One can also calculate $\mathbb{Z}_2$ directly with some Brillouin zone integral that involves Berry's potential with a continuous gauge such that electron wave functions are globally continuous [44], although such gauge may be difficult to define.

Another more common way that was adopted in our studies is to characterize the zeros of Pfaffian functions [1, 43, 44]. From some Bloch functions $u_m(\boldsymbol{k})$, one can define a unitary matrix

$$w_{mn}(\boldsymbol{k}) = < u_m(\boldsymbol{k}) | \Theta | u_n(-\boldsymbol{k}) > \tag{1.33}$$

, where $\Theta = \exp(i\pi S_y/\hbar)K$ is the TR operator with S_y and K being the spin operator and the complex conjugate. Θ is antiunitary so it satisfies $\Theta^2 = -1$ for spin half electrons, which leads to the previously stated Kramer's theorem. Thus one also should expect

$$w^T(\boldsymbol{k}) = -w(-\boldsymbol{k}) \tag{1.34}$$

At some high-symmetry points Γ_a in the Brillouin zone, $\boldsymbol{k}$ and $-\boldsymbol{k}$ coincide, so $w(\Gamma_a)$ becomes antisymmetric. There are 4 of these so called TR invariant momentum (TRIM) points in

2D Brillouin and 8 in 3D Brillouin zone. Since the determinant of an antisymmetric matrix is the square of its Pfaffian, one can define

$$\delta_a = Pf[w(\Gamma_a)]/\sqrt{Det[w(\Gamma_a)]} = \pm 1 \tag{1.35}$$

As long as $u_m(\boldsymbol{k})$ is chosen to be globally continuous in the Brillouin zone, the branch of the square root can be specified globally so the $\mathbb{Z}_2$ invariant is

$$(-1)^{\nu} = \prod_{a=1}^{4 \text{ or } 8} \delta_a \tag{1.36}$$

In presence of inversion symmetry, the Bloch states at the TRIM points $w(\Gamma_a)$ are also parity eigenstates with eigenvalues $\xi_m(\Gamma_a) = \pm 1$. Therefore, the process above can be simplified [1, 45]. For each TRIM point one can calculate

$$\delta_a = \prod_m \xi_m(\Gamma_a) \tag{1.37}$$

Here the product is over Kramer's pairs of occupied bands. Then Eqn. 1.36 becomes.

$$(-1)^{\nu} = \prod_{a=1}^{4 \text{ or } 8} \prod_m \xi_m(\Gamma_a) \tag{1.38}$$

One may note that 3D topological insulator has in total four Z_4 invariant. The formulation above describes the strong invariant ν_0. For three weak topological invariants, they can be calculated as as Pfaffian over selected four TRIM points

$$(-1)^{\nu_{i=1,2,3}} = \prod_{n_i=1; n_{j\neq i}=0,1} \delta_a \tag{1.39}$$

, where $\Gamma_a = \sum_{i=1,2,3} n_i \boldsymbol{b}_i$ marks the location of TRIM points in Brillouin zone and $\boldsymbol{b}_i$ is the primitive reciprocal lattice vectors.

1.3.6 Z_4 invariant

When TR symmetries are broken, $\mathbb{Z}_2$ becomes ill-defined. However, as long as the inversion symmetry is preserved, there exists a parity-based higher-order invariant called Z_4. It

can calculated similarly with the parity eigenvalues $\xi_m(\Gamma_a)$ mentioned above for each Bloch states at each TRIM point as follows [46]

$$Z_4 = \sum_{a=1}^{8} \sum_{m} \frac{1 + \xi_m(\Gamma_a)}{2} \text{ mod } 4 \tag{1.40}$$

The summation counts the total number of parity-odd states at all TRIM points. An odd $Z_4 = 1, 3$ suggests all product of all TRIM parities is -1, which forbids an insulating gap and corresponds to a Weyl semimetal states. If $Z_4 = 2$, it corresponds to axion insulating state and it has a quantized magnetoelectric effect with $\theta = \pi$.

1.4 Overview of Magnetism

1.4.1 Magnetic Orders

Another aspect of study on magnetic topological material is on the magnetism. Magnetism arises from unpaired electrons typically from $3d$ and $4f$ orbitals. At high temperature, the spins are uncoupled to each other due to thermal fluctuations. The spin direction can be in any direction, unless they experience and become aligned to the external field, leading to paramagnetism (PM). On the opposite, for systems without unpaired electrons are diamagnetic materials. At lower temperatures, the spins may spontaneously align themselves parallel with or opposite with each other and form long range or short range magnetic order.

There are generally three types of magnetic orders- FM structure where all moments are aligned, AFM structure in which moments are oppositely aligned and compensated, and ferrimagnetic structure where opposite spins are not fully compensated so the overall magnetization is nonzero. As these spins now adopt definite orientations depending on the crystal, the magnetic ordering can break the time reversal symmetry of the overall systems. Certain ferrimagnetism and AFM can further break translation symmetry and creates additional magnetic superlattice.

Magnetic property measurements are widely used to investigate the nature of magnetic ordering whereas neutron scattering experiment serves as the most powerful tool to obtain the

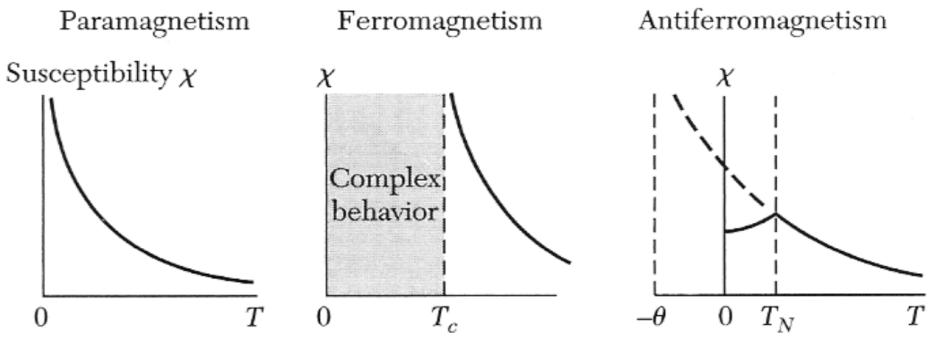

Figure 1.9: Curie-Weiss behavior of PM, FM and AFM materials, which has Curie-Weiss temperature θ to be zero, positive and negative.

magnetic structural information. The Curie-Weiss law describes the temperature dependence of the magnetic susceptibility χ above the ordering temperature

$$\chi(T) = \frac{C}{T - \theta} \tag{1.41}$$

θ is the Curie-Weiss temperature at which the susceptibility will diverge. At temperature below θ, the system develops spontaneous magnetization. If one plots the inverse magnetic susceptibility, χ^{-1}m vs. T, one would find χ^{-1} is linear with T in the PM phase and θ is the x-axis intercept. θ is zero for PM, positive for FM, and negative for AFM as shown in Figure 1.9. The slope of the curve is the inverse of Curie constant C in the Eqn. 1.41 .

$$C = \frac{\mu_0 \mu_B^2}{3k_B} n g^2 J(J+1) \tag{1.42}$$

where n is the number of atoms per unit volume, g is the Landé g-factor, μ_B is the Bohr magneton, J is the angular momentum quantum number, the rests are fundamental constants. If C is in the unit of Oe-mol/emu, one can simply get the effective moment, which is a temperature-independent term, $\mu_{\text{eff}} = \sqrt{8C}$ in the unit of μ_B per atom. The effective moment allows us to estimate the spin state of the magnetic ions.

The reason why a material adopts one magnetic structure over another depends on the combined effect of several energy schemes, including magnetic exchange interactions, magnetic anisotropy and the coupling with external magnetic field. We will next overview each relevant term in the rest of the section.

1.4.2 Magnetic exchange interactions

The type of magnetism depends on the mechanism of the magnetic interaction. Like classic dipoles, magnetic moments can couple through dipolar interaction. The dipole-dipole interaction between two moments m_1 and m_2 can be described as

$$E = \frac{mu_0}{4\pi r^3}[\boldsymbol{m}_1 \cdot \boldsymbol{m}_2 - \frac{3}{r^2}(\boldsymbol{m}_1 \cdot \boldsymbol{r})(\boldsymbol{m}_1 \cdot \boldsymbol{r})] \tag{1.43}$$

The dipole-dipole interaction prefers a FM configuration. However, for a solid-state system, this short-range effect is usually very weak. Rather, magnetic exchange interactions from a quantum mechanical origin, the Pauli's exclusion principles, tends to dominate.

The exchange interaction describes the process in which two unpaired spins exchange in position between nearby magnetic atoms. From the exclusion principles, electrons with the same spins experience a different (usually stronger) repulsion than those with opposite spins. The process can be captured by Heisenberg Hamiltonian,

$$H = -\sum_{i,j} J\boldsymbol{S_i} \cdot \boldsymbol{S_i} \tag{1.44}$$

This type of interaction depends on the sign of J. If J is positive, the interaction favors a FM picture. If J is negative, AFM ground state is favored instead. This can happen between two nearest-neighboring magnetic atoms (Direct Exchange) or over a longer range via intermediate atoms (Superexchange). Its strength depends on the extent of hopping between the atoms as well as the hopping distance. If the superexchange interaction is via the intermediate atom at an angle of 90 (180) degrees, the interaction favors a FM (AFM) configuration. In nature, it was found that the superexchange is usually AFM.

Ruderman–Kittel–Kasuya–Yosida (RKKY) interaction is the exchange that occurs between localized moments (typically in $4f$ orbitals) through conducting electrons. The sign of RKKY interaction is distance-dependent. Dzyaloshinskii-Moriya (DM) interaction is an antisymmetric, anisotropic exchange coupling in a lattice without inversion symmetry. These two are common mechanism for many non-collinear or non-coplanar AFM, which may have unique magnetic and transport response.

1.4.3 Magnetic Anisotropy

For most magnetic materials, it is energetically preferable for the moments to stay in certain direction than others. The system is said to have magnetic anisotropy, which adds another term to the Hamiltonian in addition to the exchange term. The axis or plane in which the moment can have the lowest anisotropy energy is called easy axis/plane. Ones with the highest anisotropy energy are called hard axis/plane.

One major source of magnetic anisotropy comes from the crystal structure called magnetocrystalline anisotropy. It is a result of the coupling between the electron orbit and the crystal electric field. The easy axis is typically the principal axis of the crystal lattice. Other sources of magnetic anisotropy include sample geometry, sample tension, and exchange interaction. They combined lead to the observed overall anisotropy.

The magnetic anisotropy can also be categorized according to the number of easy/hard axis. For the scope of this thesis on $MnBi_{2n}Te_{3n+1}$ family, we will consider the simplest case of all, uniaxial anisotropy, which usually features an easy axis and a perpendicular hard plane. Within the hard plane it is isotropic. If we let the θ be the angle between the moment direction and z axis, the anisotropy energy can be expressed as

$$H = K_1 \mathbf{S}_z^2 + HO. \tag{1.45}$$

If $K_1 < 0$, the system prefers a system with easy z axis. On the contrary, $K_1 > 0$ suggests the moments tend to lie in the plane perpendicular to z, which requires a consideration of higher order term to specify. Sometimes it is necessary to consider the higher order terms (HO), which may depend on the particular crystal structure and local environment of the magnetic atoms.

1.4.4 Coupling with magnetic field

Under external magnetic field, the system gains an additional Zeeman energy from the coupling between the field and the moment. The Zeeman term

$$H_Z = g\mu_B \mathbf{H} \cdot \mathbf{S} \tag{1.46}$$

tries to align the moment with the external field. At a high enough field, H_Z dominates in the Hamiltonian so all moments will become parallel to **H**. The evolution of a simplest ordered magnetic state under magnetic field is described by Stoner-Wohlfarth (SW) model. For a single domain ferromagnet, the Hamiltonian for the exchange coupling is always a constant, because all moments are parallel so $\mathbf{S}_i \cdot \mathbf{S}_j = S_i S_j$ for any i and j. Therefore effectively, the Hamiltonian under external field will contain the Zeeman and anisotropy term. Then the energy is simply dependent on the field and the moment directions with respect to the z axis, defined as θ_0 and θ_1 respectively. Given the field direction along θ_0,

$$E(\theta_1) = K_1 S^2 \sin^2 \theta_1 + g\mu_B HS \cos(\theta_1 - \theta_0) \tag{1.47}$$

Given a field direction at θ_0, the moments configuration at each field value will correspond to the local energy minimum of the θ_0 map with $\partial E/\partial\theta_1 = 0$. The model explains a formation of magnetic hysteresis at ground state, and proposes an astroid-like angular dependence for saturation field as shown in Fig 1.10(a) and (b). The saturation field is highest along easy axis and hard plane due to the need to overcome the entire anisotropy energy for a full flip. In reality, most ferromagnetic systems are multiple-domained, so the SW model proposed at ground state (0 K) can only be interpreted qualitatively when compared with real data at finite temperature.

The SW model can be further extended to simple AFM systems. For example, in a layered A-type AFM of $MnBi_2Te_4$, the magnetism may be simplified as two sub-lattice AFM. Then, the SW model can describe the system by simply including the interlayer exchange coupling term $J_c \mathbf{S}_i \cdot \mathbf{S}_{i+1} = J_c S_i S_{i+1}$ where J_c is the interlayer exchange coupling constant. Again, the ferromagnetic configuration within each sublattice does not contribute. Writing it in terms of E as a function of angles of both sublattices, we can get the energy

$$E(\theta_1, \theta_2) = J_c S^2 \cos(\theta_1 - \theta_2) + K_1 S^2 (\sin^2 \theta_1 + \sin^2 \theta_2) + g\mu_B HS(\cos(\theta_1 - \theta_0) + \cos(\theta_2 - \theta_0)) \tag{1.48}$$

Note there is a competing factor between J_c and K terms. The former prefers an opposite moment configuration. The latter prefers the moment stays along the axis. For the down-spin to flip up, or vice versa, it has to overcome both terms, which may not occur at the

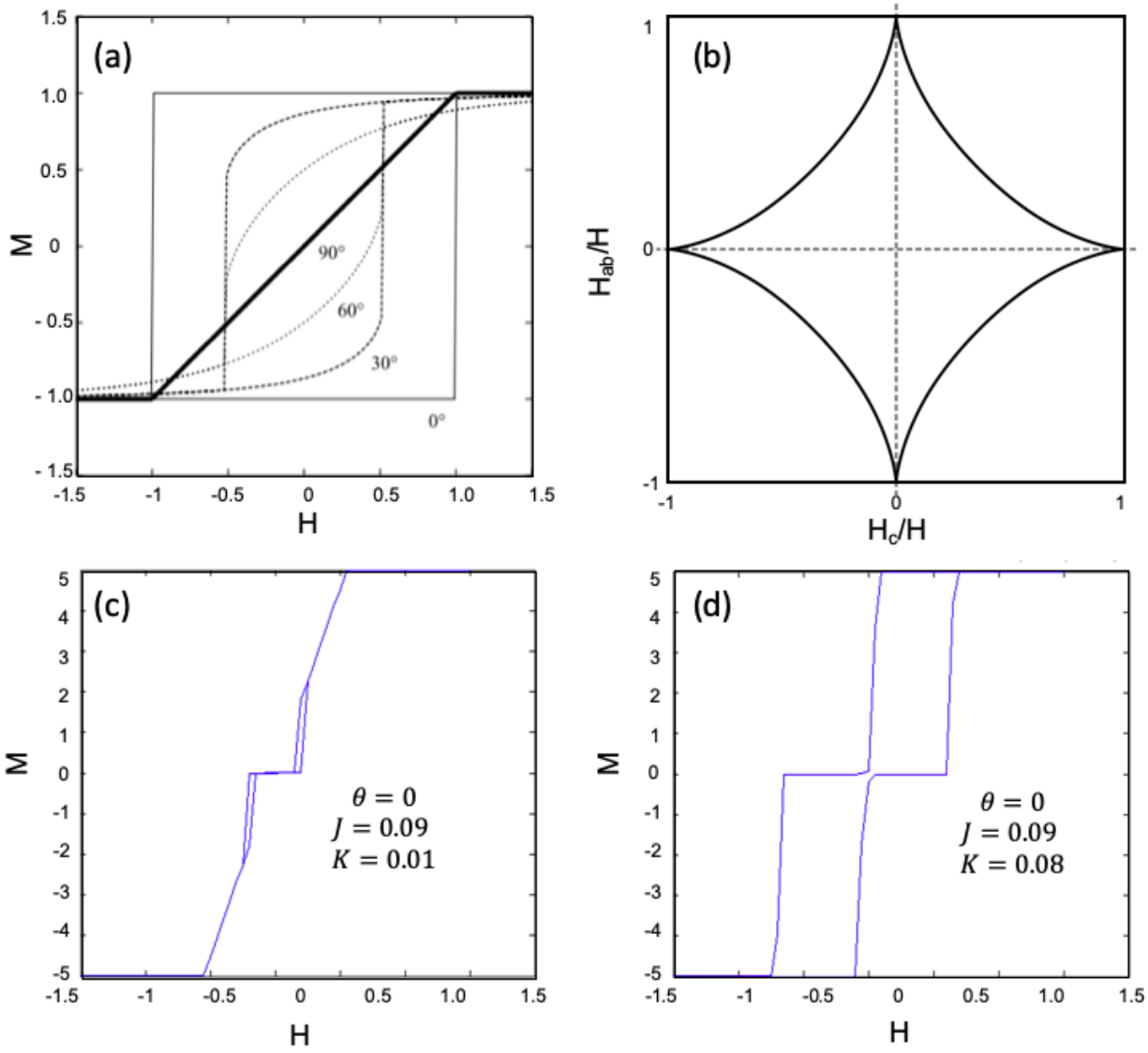

Figure 1.10: SW model for evolving magnetization with field in different situations. (a) A single-domain ferromagnet at different field orientation, adapted from Ref [47]. (b) Astroid-shaped angular dependence. The axes are the normalized in-plane and out-of plane field and each point in the curves marks where the saturation occurs in (a). (c)-(d) Modified SW model for a two-sublattice AFM system when the field is along z axis, with (c) relatively large exchange coupling J_c compared to anisotropy K and (d) comparable J_c and K. The former has a spin-flop transition from AFM to canted AFM, and then a saturation to forced FM phase; the latter features only a spin flip transition from AFM to forced FM phase.

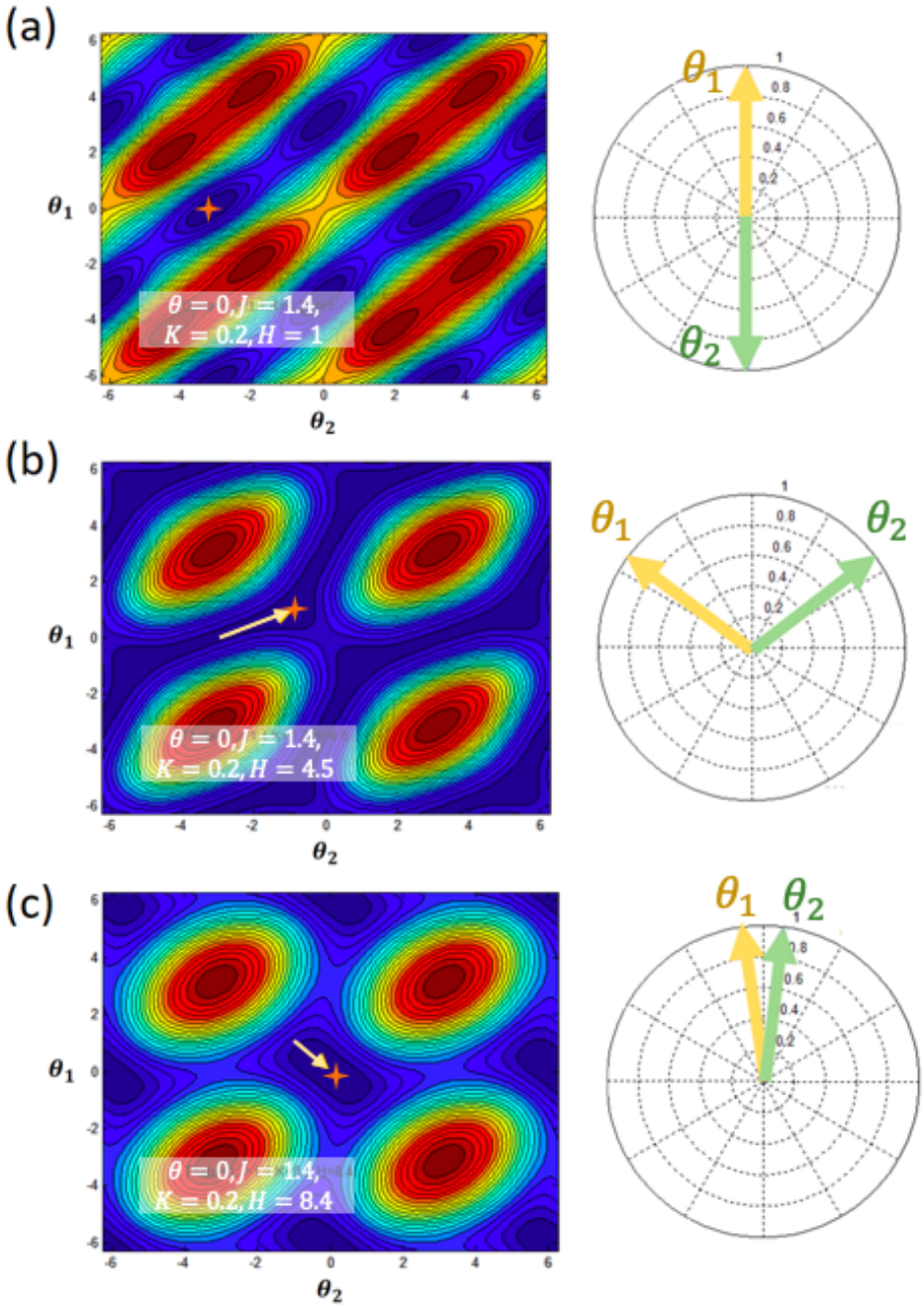

Figure 1.11: Evolution of energy landscape of the two sublattices AFM SW model at (a) low, (b) medium and (c) high field. In the left figures, the blue-to-red color scheme shows the free energy $E(\theta_1, \theta_2)$ from low to high. The star marks the configuration with the lowest energy. The arrow indicates the relative shift of the minimum with the field. The right plots show the corresponding configuration of the two sublattices at the field. The yellow and green arrows correspond to the moment along θ_1 and θ_2 respectively.

same field. If J_c is stronger than K, the system enters a canted AFM state as shown in Fig. 1.11(b). Here, the K term is first overcome so moments are partially in plane, but J_c term still dominates and forces moments to be opposite in plane. Eventually at a large field, Zeeman term dominates and the system becomes fully polarized, as shown in Fig. 1.11(c). On the other hand, if J_c is relatively small, there is no intermediate steps. Because the moments always try to align along easy axis, there is only one spin flip transition from AFM state to FM state without the intermediate step. Simulated magnetization patterns at ground state in the two contrasting scenarios are shown in Fig. 1.10 (c)-(d).

1.5 Summary: Road map to QAHE

Topology in condensed matter systems has developed rapidly in the past few decades and lead to some great advances in the field. The tremendous efforts in these years paved avenue that takes us to where we are and what we study, starting from QHE under field with nonzero Chern number, to QSHE and 3D TI showing edge/surface states under no field with nontrivial $\mathbb{Z}_2$, and finally QAHE in MTI showing spontaneous edge state with nonzero Chern number.

In this PhD thesis, we will show our search, design, synthesis, characterization and optimization of magnetic topological insulator $MnBi_{2n}Te_{3n+1}$ family. To realize a MTI material platform for QAHE, material design is a key. There are mainly two components- topology and magnetism. On the side of topology:

(1) To host nontrivial topology in TIs, one essential element is a strong SOC. The SOC is proportional to the effective charge of nucleus. That usually takes us to the bottom right of the periodic table, where atoms like Bi, Te, Sb, Pb etc. with high effective nuclear charge are situated.

(2) It is optimal to have clean band structure at the Fermi level. This means there should be ideally no other states between the bulk gap other than the topological surface states. Existing TIs such as Bi_2Te_3 family are good candidates to start with. Then, hopefully the

inclusion of magnetic atoms should not drastically change this prerequisite condition.

Then for magnetism:

(3) Magnetism requires unpaired electrons. The introduction of magnetic atoms should not bring in states around the topological band near Fermi level, so ideally the moments should be very much localized. This means, we are generally looking at the row for $3d$ transition metals and $4f$ rare earth elements (lanthanide).

(4) FM is needed. If the magnetic order is not FM, the following question will be, how can we make it into FM? This involves the design of different crystal structures and growth of the proposed systems.

(5) As we bring in additional elements, it is facile to introduce defects such as crystal defects and antisite defects. They can serve as scattering centers during the transport and lower the electron mobility. They can also change the band structure, or the magnetic structure by redistributing the magnetic atoms. Some defects are unavoidable. Some defects may not be totally destructive. Therefore, a good understanding and capability to control of these defects are essential for optimization of MTI.

CHAPTER 2

Experimental techniques

2.1 Single Crystal Growth

For many experiments in the condensed matter field today, successful single crystal growth of the material under studied is essential. A high-quality single crystal has many privileges compared to their polycrystalline counterpart. It can allow many state-of-the-art experimental techniques on the material. First of all, an ideal single crystal has only one grain, so it contains fewer defects like grain boundaries, enabling physical measurements to reflect the intrinsic characteristics of the material. Second, a single crystal has well-defined surfaces and edges. The presence of the flat surfaces allows the surface-sensitive measurements such as ARPES, STM, etc. Third, a single crystal has well-defined crystalline axis (sometimes, one can even easily identify different crystallographic axis based on the growth habit). Therefore, transport, thermodynamic, optical and other measurements can be made along specific sample orientations so that anisotropic physical properties can be obtained. For example, we can map out the 3D Fermi surfaces via quantum oscillation measurements along different crystalline orientations, etc. There are many more advantages of a single crystal, but for the MTI as a material platform to realize QAHE, there is one important advantage for being single-crystal if it is van der Waals (vdW) material. That is, good single-crystallinity and the fewer defects are superior for fabrication and quality improvement of 2D devices, providing access to study the physics in 2D limit.

Therefore generations of physicist in the field have been looking for the best recipes for crystals and ways to optimize them to yield the highest-quality single crystals for these purposes. Today, there are generally three possible routes to obtain a single crystal. One

is through solid-state melt growth. This is one where stoichiometric mixtures is first heated so everything fully reacts and melts, then material is cooled from the liquid phase directly but in a controlled fashion. A day-to-day example is freezing water into ice in our daily life. However, ice is usually polycrystalline because without control of temperature gradient there tend to be multiple grains forming together. Therefore, special ways were developed to provide delicate control of the temperature near the melting point, including Bridgman, Czochralski and floating-zone methods etc. These are often applied in the semiconducting industries for Si wafers. In general, we use melt-growth to look for possible phases. Then for single crystal growth, we are mainly using the other two types of growth, the flux-growth using high-temperature liquid solution and the chemical vapor transport using high-temperature gas vapor.

2.1.1 Flux Growth

Flux method involves growing single crystals out of high temperature liquid called flux. The growth mainly occurs in four steps. Firstly, the starting materials all dissolve in the flux at high temperature, effectively forming a high-temperature solution with the flux as solvent and the constituent elements of the target phase as solute. The solution is held at this high temperature for a few hours to ensure a homogeneous liquid formation. Secondly, upon cooling to a temperature where the solubility of the solute becomes smaller than its actual concentration in the flux, the system becomes oversaturated. As a result, the target phase starts to precipitate through nucleation of tiny crystals and its concentration in the flux is lowered to its solubility limit. Thirdly, with further slow cooling, the solubility continues to decrease, forcing the target phase to grow around the nucleation sites. By continuous slow cooling, the process repeats and single crystals can grow large. Eventually, at a temperature that is tens degrees higher than the melting point of the flux, single crystals of the target material can be separated from the flux in liquid phase by a centrifuge.

In order for the flux to accommodate the material growth in an extended temperature range so that the single crystals can grow larger, the flux is usually chosen as the low-melting-

point and low-vapor-pressure metals like Sb, Sn, Bi and others inside which each constituent element can dissolve. A drawback here is that the flux may participate in the reaction, and thus give wrong and additional phases. One possible way to avoid this problem is to use one of the starting elements/compounds as flux, i.e., self-flux. In some cases, flux can also be binary compounds. For the works of $MnBi_{2n}Te_{3n+1}$ presented in this paper, Bi_2Te_3 is used as the self-flux. Because the crystal can form over a large temperature range, the control of the growth rate and quality is much easier than solid state reaction. For example, the number of nucleation is dependent on the cooling rate and starting elemental ratio. By tuning the two parameters, one can get growths with lots of smaller crystals or a few very large crystals.

The details for each particular growth of the materials studied in this thesis is summarized in each corresponding chapter. Here I will present an overview of the synthesis process for flux growth. The synthesis always starts with weighing elemental forms of materials. If no element is air-sensitive, like Mn, Bi, Te, this part can be done on a bench top. Otherwise, this needs to be done in the glovebox. The samples are loaded in an alumina crucible. Because the growth needs to be in an inert environment, i.e. either in vacuum or Ar gas, quartz ampules are made to hold the growth at high temperature. A section of the quartz tube is first melted at the middle to make shorter tubes with one closed end. The crucible with the starting material is then loaded into the quartz tube with a little quartz wool at the bottom and more on the top. Then a neck is made on top of the tube to leave a small channel for pumping. The quartz tube is then pumped and purged for a few times until the pressure falls down below 50 mTorr, one can seal the tube at the neck. That leaves us with samples contained in a fully evacuated quartz ampule. Then the tube is placed in a box furnace and first heated to very high temperature so everything is melted, followed by slow cooling as described earlier in this section. When the final temperature is reached, the quartz tube is quickly inverted and moved to a centrifuge. It quickly starts to spin the tube at 3000 rounds per min, effectively providing a large centrifugal acceleration nearly 1000 g. The large acceleration allows the most viscous liquid to flow out of the alumina crucibles so that the crystals inside the crucibles can be separated from the liquid flux.

2.1.2 Chemical Vapor Transport

In chemical vapor transport (CVT) growth, transport agents are frequently used and single crystals are grown out of the vapor phase. Transport agents are volatile elements or compounds such as halogens, $AlBr_3$ and $TeCl_4$, etc. In some special cases where one or a few starting materials are volatile themselves, they are capable of transporting without additional agents. For most reactions, which are exothermic, the source end where the starting materials are loaded is hotter while the sink end where the single crystals grow is colder. The transport agents react with the constituent elements of the target material at the source end to form intermediate gaseous compounds. At the sink end, if the target phase has a lower free energy of formation than the intermediate gaseous phases, the intermediate phases disassociate and the target phase nucleates. Since the final product depends on the transport rate of each element in the equilibrium state as well as the phase stability at the sink end, the key of a successful CVT growth is to optimize the temperature profile, the type of transport agent, the initial element ratio as well as the length of the tube so that our target phase is favored at the sink end. Note the growth is an equilibrium process where the intermediate compounds disassociate and associate simultaneously everywhere. Such an equilibrium depends on multiple factors including the type of transport agent and the temperature, so at different parts of the tube, the rate of disassociation and association varies. Overall, the intermediate compounds form faster at the source end, while they disassociate the most at the sink end. Therefore, the crystals can grow large at the sink end over time until all constituent elements are transported to the sink end. It turns out the larger the temperature gradient and the more the transport agent, the faster the growth rate.

Experimentally, elemental mixtures of starting materials are added in a quartz tube which is then necked down as described in section 2.1.2. Then transport agent is carefully added through the neck to avoid too much heating on the volatile transport agent during the tube-sealing process. The growth ampule is slowly heated to high temperature to avoid overpressure due to the volatile elements. Then it is transferred to a 3-zone tube furnace where the temperatures at two ends of the ampule are calibrated. The growth time varies

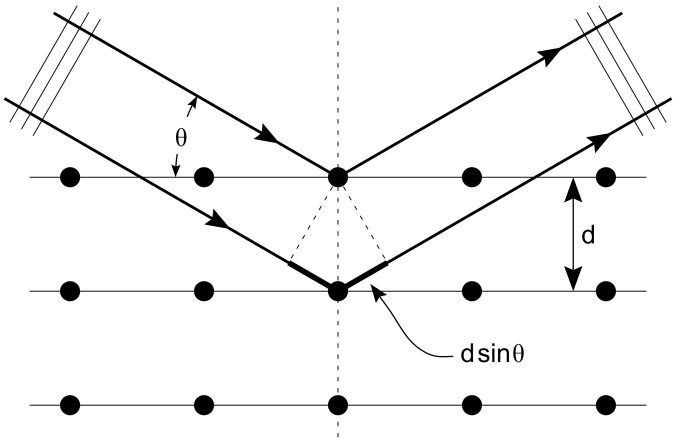

Figure 2.1: Bragg's condition for constructive interference that gives the Bragg peak in XRD spectrum.

from a few days to weeks to get mm-sized single crystals at the sink.

2.2 Structure determination

2.2.1 X-ray diffraction

Once crystals are grown, the next step is to determine the structure to identify the phase and check the purity. Powder X-ray diffraction (XRD) are performed using PANalytical Empyrean Cu-Kα diffractometer at room temperature. Each peak corresponds to a repeating unit length along a certain direction in which the particle in the powder is oriented. The relationship of the unit length and scattering angle is given by Bragg's law.

$$n\lambda = 2d\sin\theta \tag{2.1}$$

n is the diffraction order. $\lambda = 1.5406$ Åfor Cu-Kα. d is the length of the repeating unit in real space, so it depends on and contains the crystal structural information. θ is the diffraction angle. The peak marks the condition where the diffracted beam can interfere constructively as shown in Fig. 2.1.

If the structure of a material is totally unknown, single crystal XRD is the most powerful way to determine it since it maps out the reflection peaks in the entire 3D reciprocal

space. With the structural information from every single peak, the powder XRD spectrum is analyzed using HighScore Plus for phase determination. If needed, Rietveld refinement is performed to refine the detailed crystalline information using the FullProf software [48]. Nonetheless, powder XRD is a destructive method. It allows us to check the phase purity of an entire crystal at the expense of turning the crystal into powder. One alternative is to check a particular surface reflection. It provides the phase information of that surface but not the overall purity. For example, for $MnBi_{2n}Te_{3n+1}$, we can perform X-ray on the flat side, i.e., (00L) surface. The (00L) spectrum reflects the lattice spacing along the c axis and is usually a good guide to distinguish different members in $MnBi_{2n}Te_{3n+1}$.

2.2.2 Neutron Scattering

Neutron is an elementary particle that can diffract on crystals just like X-ray photons. Furthermore, because neutron is a spin 1/2 fermion, it can diffract not only on the crystal structure, which consists of mainly the heavy nuclei, but also on the electrons carrying ordered magnetic moments too. In comparison, photons are spin-0 bosons, so X-ray diffraction cannot provide the magnetic information in XRD. On the other hand, neutron diffraction can provide both the nuclear and magnetic structure.

Like XRD, neutron diffraction can be done on single-crystal and powder. For our studies, single-crystal neutron diffraction was performed below the magnetic ordering temperature for the magnetic structure determination, and high temperature for the crystal structure refinement on HB-3A DEMAND single-crystal neutron diffractometer located at Oak Ridge National Laboratory [49]. Neutron wavelength of 1.551 Å was selected by a bent perfect Si-220 monochromator. The nuclear and magnetic structures were subsequently refined with the FULLPROF SUITE software [48].

2.2.3 Energy and wavelength dispersive spectroscopy

Energy dispersive spectroscopy (EDS) and wavelength dispersive spectroscopy (WDS) are two common ways for elemental analysis. While the diffraction studies can determine sample

phases by solving the crystal structure, elemental analysis also provides direct chemical analysis of the elemental ratio. In combination with the scattering tools, WDS and EDS can help us better understand the extent of antisites, interstitials or vacancies in the sample. Furthermore, for many doping studies, the actual doping level are usually different from the nominal values from the growth. In these cases, EDS and WDS help to determine the actual doping levels.

Both EDS and WDS analyze the X-ray emission spectrum after the sample is hit with high energy electron (usually 15-20 kV). After the high energy electrons knock out a deeply localized electron in an atom, the emission occurs as the outer electrons relax into the hole. Since each element has unique atomic orbitals, it has a characteristic emission spectrum. The total spectrum is a combination of the emissions from all the elements, which allows qualitative determination of the elemental ratio.

EDS measurements were performed using an energy dispersive X-ray spectroscopic analyzer (EDAX; EDAX Inc.) mounted on a scanning electron microscope (JEOL JSM 6700 F). It measures the entire X-ray emission spectrum, and does numerically fitting with the known spectra of all elements to determine the elements and the ratios. WDS measurements were performed on a JEOL JXA-8200 Superprobe. The probe comes with several diffraction unit to measure the intensity of the emission at a particular wavelength. Each has been calibrated with a pure elemental sample. The measurement gets the relative intensity compared to the pure element, and outputs the percentage of the calibrated elements in the sample.

2.3 Physical property measurement

The physical property measurement in this study includes the field dependence and temperature dependence of the electric transport, heat capacity and the magnetization.

2.3.1 Electrical transport property measurement

Electrical transport measurements were performed using the Quantum Design Dynacool Physical Properties Measurement System (QD Dynacool PPMS). They are done using the standard six-probe configuration. The samples are typically cut or polished into a bar shape whose dimensions can be well determined. The temperature dependence can be measured from 1.8 K to 400 K. The magnetotransport data were collected during the field sweep from -9 T to 9 T. In order to get rid of the mixed-channel signal, the data were then symmetrized to obtain $\rho_{xx}(B)$ using $\rho_{xx}(B) = \frac{\rho_{xx}(B)+\rho_{xx}(-B)}{2}$ and antisymmetrized to get $\rho_{xy}(B)$ using $\rho_{xy}(B) = \frac{\rho_{xy}(B)-\rho_{xy}(-B)}{2}$. The sign of ρ_{xy} is chosen so that hole carriers lead to positive ρ_{xy}.

2.3.2 Specific heat measurement

Specific heat measurements were performed using QD Dynacool PPMS. The sample is loaded onto a 2 mm x 2 mm platform. The sample surface in contact with the platform needs to be flat to ensure a good thermal contact with the platform. Apiezon N grease is used to further enhance the thermal contact between the sample and the platform in the temperature rage we measured. The PPMS chamber is pumped to high vacuum during the measurement to minimize the thermal transport through the gas medium.

The relaxation technique is used for the thermodynamic measurement. First heat is applied at certain power for a short period of time. The heat is then gradually lost to the environment through the supporting wires. The temperature response on the platform T_p is recorded throughout the process, which follows

$$C\frac{dT}{dt} = -K_w(T - T_0) + P(t) \tag{2.2}$$

The K_w is the thermal conductance of the wires. T_0 is the PPMS temperature. $P(t)$ is the power of the heat. The data allow us to solve for C, the total heat capacity of both the sample and the platform. In practice, two sets of measurement are taken- first just for the background which includes the platform and the grease, and then with the added sample.

Eventually

$$C_{\text{sample}} = C_{\text{total}} - C_{\text{background}} \tag{2.3}$$

2.3.3 Magnetic property measurement

Magnetic property measurement was performed using the QD Magnetic Properties Measurement System (QD MPMS3). The MPMS3 features a Superconducting Quantum Interference Device (SQUID) magnetometer, which has a pick up coil to detect the change of internal field from the moving sample with the sensitivity on the order of 10^{-7} to 10^{-8} emu. Both DC and AC moment data can be measured. In the vibrating sample magnetometer (VSM) mode, the sample is vibrated at a set frequency, and the pick-up coil is used to detect the electromotive force generated from the internal field and the motion, which is then processed to determine the actual magnetic response from the sample with a few-times higher sensitivity.

In preparation of the measurement, the sample is loaded on a quartz or straw holder with GE varnish. For temperature-dependent susceptibility measurement, two cooling modes are used, zero-field-cooled (ZFC) and field-cooled (FC). In the ZFC mode, the sample is first cooled across the ordering temperature under no field before the field is switched on for measurements. The ZFC data are taken while the sample is then warmed across the ordering temperature with the field on. In the FC mode, the sample is cooled with field on, and data are taken while the sample is then warmed across the ordering temperature. If FC and ZFC data bifurcate, it indicates certain magnetic states such as spin glass or soft ferromagnets where magnetic relaxation plays a role.

CHAPTER 3

The discovery of $MnBi_4Te_7$: an intrinsic antiferromagnetic topological insulator with weak interlayer magnetic coupling

This chapter is adapted from [50]. This work was done in collaboration with Dan Dessau's group at University of Colorado, Boulder on ARPES measurements, Qihang Liu's group at Southern University of Science and Technology on first-principles band structure calculations, Huibo Cao's group at Oak Ridge National Lab on neutron diffraction measurements and Arthur P. Ramirez's group at University of California, Santa Cruz on magnetic property measurement.

3.1 Introduction

The proposal and discovery of quantum anomalous Hall effect (QAHE) in $MnBi_2Te_4$ have unarguably been one of the most significant breakthroughs in the field of condensed matter physics in recent years [51–55]. Since the discovery of topological insulator (TI) in 2000s, there have been predictions of various novel topological states when the topology is accompanied with magnetic order, such as the axion insulators, the magnetic Weyl semimetals, the Chern insulators and the 3D quantum anomalous Hall (QAH) insulators [3]. The interplay between topology and magnetism can lead to fascinating phenomena including QAH effect and quantized magnetoelectric effect (QME), and provides future opportunities for application in low-energy-consumption devices, quantum metrology and quantum computing [56–58]. Therefore the search of these magnetic topological materials, and magnetic topo-

logical insulator (MTI) in particular, have been a goal for many in the past decade. In 2013, QAHE was first achieved in a MBE-grown thin film, made of MTI $Cr_{0.15}(Bi_{0.1}Sb_{0.9})_{1.85}Te_3$, only at extremely low temperature of 30 mK [22]. The requirement for such a low temperature to realize QAHE, is a result of defect that comes along with the chemical doping. To overcome this issue, a topological material that is intrinsically magnetic was very much desired.

Then comes $MnBi_2Te_4$, the first of such kind, an intrinsic system with both magnetism and non-trivial band topology [51,51–55,59–67,67–72]. It crystallizes in the $GeBi_2Te_4$ structure with the septuple layers (SL) of $[MnBi_2Te_4]$. It orders below 24 K with the A-type AFM structure, that is, the spins are FM aligned in the *ab* plane but AFM coupled along the *c* axis. Its van der Waals (vdW) nature also makes exfoliation possible and facilitates the fabrication of thin film devices. Indeed, within a year of its first proposal, quantized Hall resistance is found at the record high temperature of 1.5 K under no field in a 5-layer device, or tens of Kelvins when it enters the forced FM state above the saturation fields [54,55,67].

Although FM state is crucial to realize the QAH effect experimentally, as we await an ideal candidate that has both TI and FM properties, an intrinsic AFM TI with low saturation fields and clean band structure where only non-trivial bands cross the Fermi level can also provide a good material platform. By this, the QAH effect may be realized with higher temperatures and reasonably low magnetic fields, which will allow us to study their associated emergent phenomena at more accessible conditions. How can we realize such intrinsic AFM TIs based on the $[MnBi_2Te_4]$ building block? Given that $MnBi_2Te_4$ is AFM with in-plane FM and out-of-plane AFM exchange interaction, one material design strategy is to reduce the interlayer AFM Mn-Mn exchange interaction by introducing spacer layers between $[MnBi_2Te_4]$ layers. Then what kinds of spacer layer can be compatible with $[MnBi_2Te_4]$? Recall that $MnBi_2Te_4$ crystallizes in the $GeBi_2Te_4$ structure, and $GeBi_4Te_7$ [73] with alternating SL $[GeBi_2Te_4]$ and quintuple layers (QL) $[Bi_2Te_3]$ exists, therefore, $[Bi_2Te_3]$ may alternate with $[MnBi_2Te_4]$ to form $MnBi_4Te_7$. with much larger Mn-Mn interlayer distance than that in $MnBi_2Te_4$. This superior compatibility, if it works, will provide us with flexible structural control to

achieve our goal. Furthermore, not only can such superlattices manifest weak interlayer magnetic coupling, but they can also serve as natural heterostructures by exfoliation, which may enable the realization of various topological states.

In this chapter, I will first review the structure and physical properties of $MnBi_2Te_4$. Based on this building block, with our material design strategy, I will then present our discovery of $MnBi_4Te_7$ which has alternating layers of the SL [$MnBi_2Te_4$] and QL [Bi_2Te_3] building blocks. Through our transport, thermodynamic, collaborative angle-resolved photoemission spectroscopy (ARPES) and density functional theory (DFT) calculations, we discovered that $MnBi_4Te_7$ is a Z_2 AFM TI with an out-of-plane saturation field as low as 0.22 T at 2 K, 40 times lower than that of $MnBi_2Te_4$. Furthermore, the natural-heterostructure-like construction of $MnBi_4Te_7$ can host two distinct (001) surface states. For the [Bi_2Te_3] termination, clean gapped surface states are observed as has long been desired; while for the [$MnBi_2Te_4$] termination, nearly gapless surface Dirac cone is observed, similar to the case of the $MnBi_2Te_4$ compound [66, 68, 69, 74].

3.2 The first intrinsic AFM TI $MnBi_2Te_4$

The magnetism and topology of $MnBi_2Te_4$ have been extensively studied both experimentally and theoretically. Its magnetism benefits from a nearly uniformly distributed magnetic Mn layers in the middle of SL. Below the Néel temperature at 24 K, $MnBi_2Te_4$ adopts an A-type AFM structure: the Mn atoms in the same layer are FM coupled with the moment pointing out of the plane, while the Mn magnetic sheet in one SL is AFM coupled to the magnetic Mn sheet in the adjacent SL. Such a structure is plotted more clearly in Fig. 3.1 (a) and has been confirmed by transport, magnetization and neutron diffraction studies previously [53, 75].

In terms of topology, the strong spin-orbit coupling reverses the bands of Bi $6p$ and Te $5p$ orbitals. The band inversion allows topological surface states in between, and rich topological states under different magnetism and dimensions as shown in Fig. 3.1. In the A-

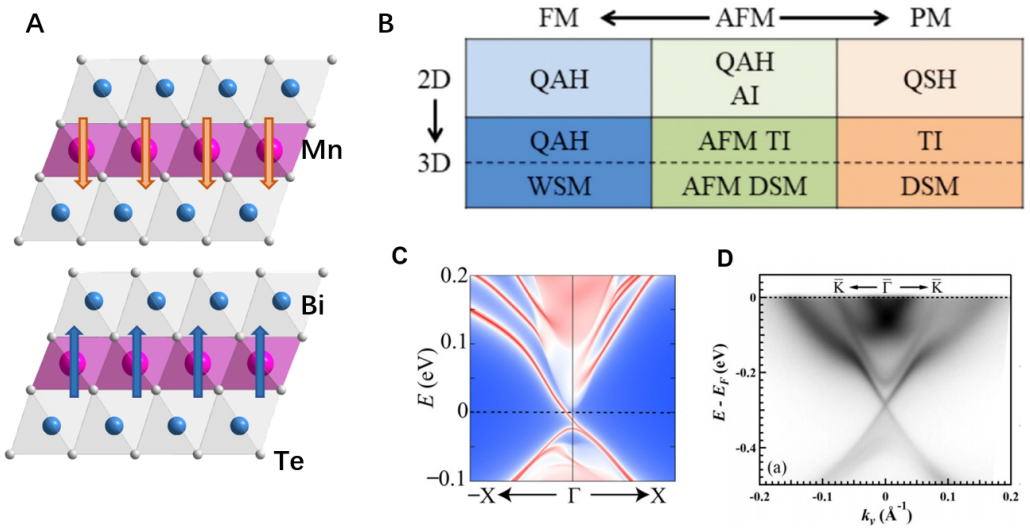

Figure 3.1: (a) Crystal structure and A-type AFM structure in $MnBi_2Te_4$, featuring in-plane FM and out-of-plane AFM. (b) Rich topological states in $MnBi_2Te_4$ thin films (2D) and bulks (3D) in AFM, FM and PM state. AI denotes axion insulator; QSH denotes quantum spin Hall; DSM denotes Dirac semimetal. (c) DFT-calculated band structure of a 5-SL film featuring an edge state inside the gapped surface state. (d) ARPES $k-E$ map along $\bar{k}-\bar{\Gamma}-\bar{k}$ showing a linear, X-shaped, gapless state between the valence and the conduction bands. (b)-(c) are taken from [52]. (d) is taken from [66].

type AFM, the (00L) surface is gapped due to the symmetry breaking and leaving an 1D edge state in its 2D limit as shown in the DFT. While this is the case theoretically [51–53], both gapless [66, 68, 69, 74, 76, 77] and gapped [53, 63, 75, 78, 79] surface states have been reported in ARPES and caused a lot of debates. The seemingly contradictory result may come from measurement effect of averaging of spectrum relevant to the spot size, or disordered surface magnetism upon cleaving, etc. While whether such a surface state is gapped or gapless remains in hot debates, QAH effect was indeed observed in a 5-layer device and Chern insulator state was discovered in even-layer devices [54, 55, 67], bringing lots of excitements in the field.

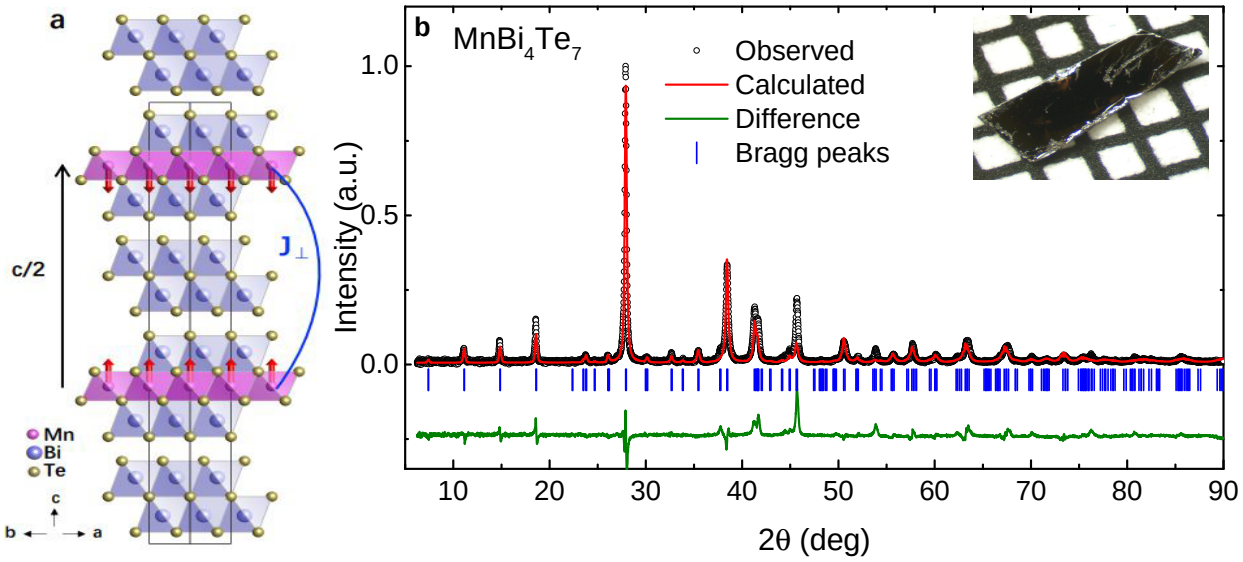

Figure 3.2: (a) Crystal structure of $MnBi_4Te_7$ with the highlighted interlayer exchange interaction $J_\perp$ between the Mn layers. (b) Powder X-ray diffraction and the refinement of $MnBi_4Te_7$. Inset: single crystal of $MnBi_4Te_7$ on mm-grids.

3.3 Growth and Characterization of $MnBi_4Te_7$

Although the existence of $MnBi_4Te_7$ was first reported in Ref [60], no single crystals were made and no physical properties were reported for the sample in its pure phase. Therefore, we have grown single crystals of $MnBi_4Te_7$ using Bi_2Te_3 as the self-flux. Mn, Bi, and Te are mixed at a ratio of MnTe:Bi_2Te_3=15:85. The mixture is first placed in an alumina crucible and sealed under 1/3 atm of Ar inside a quartz tube. The ampule was heated first to 900 °C for a few hours to ensure a good mixing, quickly cooled to 600 °C followed by slow cooling down the target decanting temperature 585 °C in 3 days. After dwelling at the final temperature for 3 days, cm-sized plate-like single crystals can be obtained when the liquid Bi_2Te_3 flux is spun out in a centrifuge.

Next, to find out the phase of single crystals from the growth, one quick way is to measure XRD on their flat $(00L)$ surfaces. Because $MnBi_4Te_7$ has a very distinct lattice parameter c among other layered materials, their Bragg reflections on $(00L)$ can well distinguish it from

other layered materials such as the Bi_2Te_3 flux. Then we perform powder XRD to obtain the crystallographic information, which is shown in Fig. 3.2 and Rietveld refinement of the pattern agrees well the $MnBi_4Te_7$ structure model given in Figure 3.2 (a). The details of the refinement could be found in Table B.1.

3.4 Magnetic, Transport, and Thermodynamic Properties

3.4.1 A-type AFM in $MnBi_4Te_7$ revealed by magnetic property measurements

The effect of the $[Bi_2Te_3]$ spacer layers can be readily seen by comparing the transport and magnetic data of $MnBi_2Te_4$ and $MnBi_4Te_7$. Figure 3.3 shows the measurement of magnetic susceptibility and isothermal magnetization of $MnBi_2Te_4$ and $MnBi_4Te_7$ in comparison. In Fig. 3.3 (a), the AFM of $MnBi_2Te_4$ transition is revealed by a cusp in $\chi(T)$ at 24 K with H $\parallel$ c. Under an external magnetic field along the c axis, a spin-flop transition starting at 3.5 T indicated by a step-like increase in magnetization is shown in Fig. 3.3 (c). $M(H)$ eventually saturates around 7.7 T. On the other hand, if the field is along the ab plane, $M(H)$ remains linear with field up to 7 T and saturates at much higher fields [75]. The higher saturation field along the ab plane indicates an easy c-axis for the moments in the system.

For the same data of $MnBi_4Te_7$ in the bottom panels of Fig. 3.3, one can see similar traits to those for $MnBi_2Te_4$. Figure 3.3(b) presents the field-cooled (FC) and zero-field-cooled (ZFC) magnetic susceptibility data of χ^{ab} (H $\parallel$ ab) and χ^{c} (H $\parallel$ c) measured at 0.01 T for $MnBi_4Te_7$. For $MnBi_4Te_7$, the abrupt halt in the rise of χ^{c} on cooling suggests the onset of AFM ordering at 13 K. This is consistent with the specific heat measurement as shown in the inset of Fig. 3.3(b), where an anomaly associated with entropy release due to the AFM transition emerges at 13 K. Fitting the (inverse) susceptibilities up to 80 K to the Curie-Weiss law results in Weiss temperatures of $\Theta_W^{ab} = 11.5$ K, $\Theta_W^{c} = 12.2$ K, $\Theta_W^{ave} = 11.7$ K, and effective moments of $\mu_{eff}^{ab} = 5.4\mu_B$/Mn, $\mu_{eff}^{c} = 5.1\mu_B$/Mn and μ_{eff}^{ave}= $5.3\mu_B$/Mn. These values indicate magnetic isotropy above T_N and thus negligible single ion anisotropy in the material. Despite the fact that $MnBi_4Te_7$ is AFM below 13 K, the positive Θ_W^{ave} of

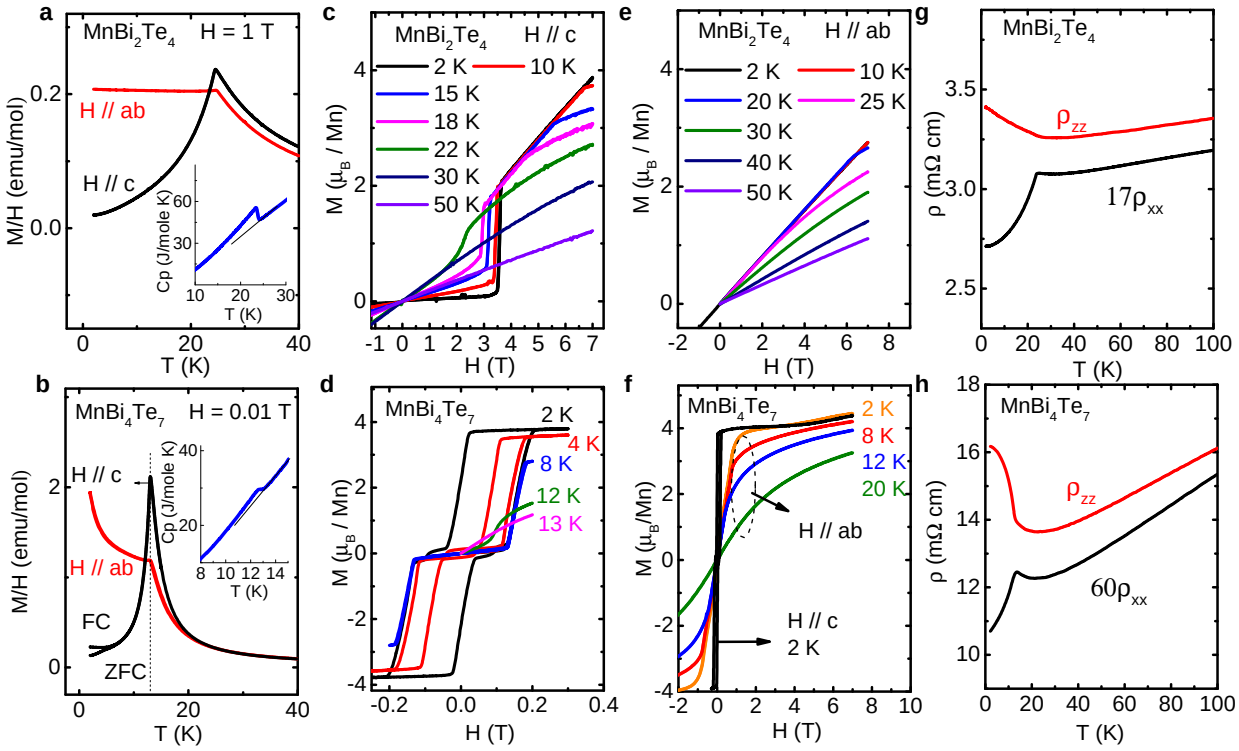

Figure 3.3: Temperature dependent magnetic, transport and specific heat properties of $MnBi_2Te_4$ and $MnBi_4Te_7$. (a-b): The temperature dependent susceptibility taken at H = 1 T for $MnBi_2Te_4$ and H = 0.01 T foe $MnBi_4Te_7$, respectively. Inset: The temperature dependent specific heat for the respective compound. (c-d): Isothermal magnetization of $MnBi_2Te_4$ and $MnBi_4Te_7$ for H$\|c$. For $MnBi_2Te_4$, there is a spin-flop near 3.5 T and no sign of saturation is reached up to 7 T. For $MnBi_4Te_7$, the saturation occurs at 0.22 T and a hysteresis loop of isothermal magnetization is seen below 8 K. (e-f): Isothermal magnetization up to 7 T with $H\|ab$ for $MnBi_2Te_4$ and $MnBi_4Te_7$. (g-h): Anisotropic temperature-dependent resistivity, ρ_{xx} and ρ_{zz} for $MnBi_2Te_4$ and $MnBi_4Te_7$.

11.7 K suggests strong ferromagnetic (FM) exchange interactions. In comparison, $MnBi_2Te_4$ has a much higher T_N of 24 K and a much lower Θ_W^{ave} of 3 to 6 K, this may indicate that the energy scales of the FM and AFM exchange interaction are much closer in $MnBi_4Te_7$. This is consistent with our expectation that the extra $[Bi_2Te_3]$ layer reduces the interlayer exchange interaction between adjacent Mn layers as we initially designed. The AFM orders of both $MnBi_2Te_4$ and $MnBi_4Te_7$ are formed under the superexchange scenario, where the magnetic interaction between the adjacent Mn layers is mediated by the Bi and Te in the path. Despite the long distance between the adjacent Mn layers (23.7Å), our DFT calculation indeed reveals an A-type AFM configuration in $MnBi_4Te_7$ with the interlayer exchange coupling about -0.15 meV/Mn, which is about one order of magnitude smaller than the counterpart of $MnBi_2Te_4$. More details are given in Supplementary Note of Ref [50].

Despite the close resemblance in temperature-dependent susceptibility, the magnetization of $MnBi_2Te_4$ and $MnBi_4Te_7$ contrast strongly with each other under magnetic field. Figures 3.3(d) and (f) present the hysteresis loops of isothermal magnetization data for M^c (H ∥ c) and M^{ab} (H ∥ ab) for $MnBi_4Te_7$. As shown in Fig. 3.3(d), in sharp contrast to $MnBi_2Te_4$ where a spin-flop transition takes place at 3.5 T, and saturates at 7.7 T in M^c (H) [75], $MnBi_4Te_7$ undergoes a first-order spin-flip transition with hysteresis starting at a much lower field of $H_f = 0.15$ T. It quickly enters the forced FM state and saturates at $H_c = 0.22$ T. The small saturation field again indicates weaker interlayer AFM exchange interactions than in $MnBi_2Te_4$. Upon warming up to 10 K, the hysteresis area is gradually reduced to zero, but H_c remains little changed, indicating a sharp triggering of the spin-flipping between 10 K and T_N. With H ∥ ab, the saturation field is 1.0 T, indicating the c axis as the magnetic easy axis and thus likely Ising form. As shown in Fig. 3.3(f), the saturation moment is $3.5\mu_B$/formula unit or 4.2 μ_B/Mn at 7 T, which is on the same order of 3.84 μ_B/Mn in $MnBi_2Te_4$ at 7 T but smaller than the DFT calculated value of 4.6 μ_B/Mn. The reduced Mn saturation moments in this family may arise from Mn disorders, which will be discussed in Chapter 5.

3.4.2 Strong coupling between charge carrier and magnetism of $MnBi_4Te_7$

Figure 3.3(g)-(h) show the temperature dependent in-plane (ρ_{xx}) and out-of-plane resistivity (ρ_{zz}) for $MnBi_2Te_4$ and $MnBi_4Te_7$. For both curves above the transition temperature, ρ_{xx} and ρ_{zz} decrease upon cooling with ρ_{zz}/ρ_{xx} near 18 and 53 for $MnBi_2Te_4$ and $MnBi_4Te_7$ respectively at 300 K, suggesting a large transport anisotropy that is consistent with its vdW nature. With further cooling, ρ_{xx} and ρ_{zz} increase slightly, which is likely caused by the enhanced scattering from spin fluctuations, a phenomenon frequently observed in low dimensional magnetic materials. Then at the transition temperature, a sudden drop of ρ_{xx} and a sharp increase of ρ_{zz} are observed. This is in agreement with the A-type magnetic structure shown in Fig. 4.1 since the antiparallel alignment of Mn moments can reduce the conductivity via spin-flip scattering, while parallel alignment of the Mn moments will eliminate such scattering and thus enhance the conductivity. The close resemblance here again confirm the same A-type AFM structure in $MnBi_2Te_4$ and $MnBi_4Te_7$.

The spin-flip transition strongly affects the magnetotransport in $MnBi_4Te_7$, as shown in Fig. 3.4 (a)-(b) for $H\|c$ and Fig. 3.4 (c)-(e) for $H\|ab$. In Fig. 3.4 (a), ρ_{xx}(H), and ρ_{xy}(H) follow the same hysteresis as that in M(H) at 2 K. With H||c, the transverse magnetoresistivity of ρ_{xx} with I||ab (mid panel of Fig. 3.4(a)) enters into a plateau between 0 T to H_f at 0.15 T that correspond to the AFM state. Above 0.2 T, ρ_{xx} drops by 3.8%. In the bottom panel showing the Hall resistivity, the negative overall slopes in ρ_{xy}(H) across all $MnBi_{2n}Te_{3n+1}$ suggest a universal n-type carrier in this family due to the Mn deficiencies. The linear ρ_{xy}(H) to 9 T above 50 K indicates single-band transport. Then using $n = H/e\rho_{xy}$, our high temperature Hall data [50, 80] yield the electron carrier density of 2.84×10^{20} cm^{-3} for $MnBi_4Te_7$, similar to that of $MnBi_2Te_4$ [53]. At 2 K, the Hall resistivity can be described by $\rho_{xy} = R_0H + \rho^A_{xy}$, where the R_0H is the ordinary Hall contribution and ρ^A_{xy} represents the anomalous Hall resistivity. For $MnBi_4Te_7$, ρ^A_{xy} is extracted to be 3.3 $\mu\Omega$ cm, which is half of the one in $MnBi_2Te_4$. Consequently, the anomalous Hall conductivity σ^A_{xy} ($=\rho^A_{xy}/\rho^2_{xx}$) is 25.5 $\Omega^{-1}cm^{-1}$ and the anomalous Hall angle (AHA = ρ^A_{xy}/ρ_{xx}) is near 1%.

Because ρ_{zz} can show a greater response than ρ_{xx} in the layered magnetism, it provides a

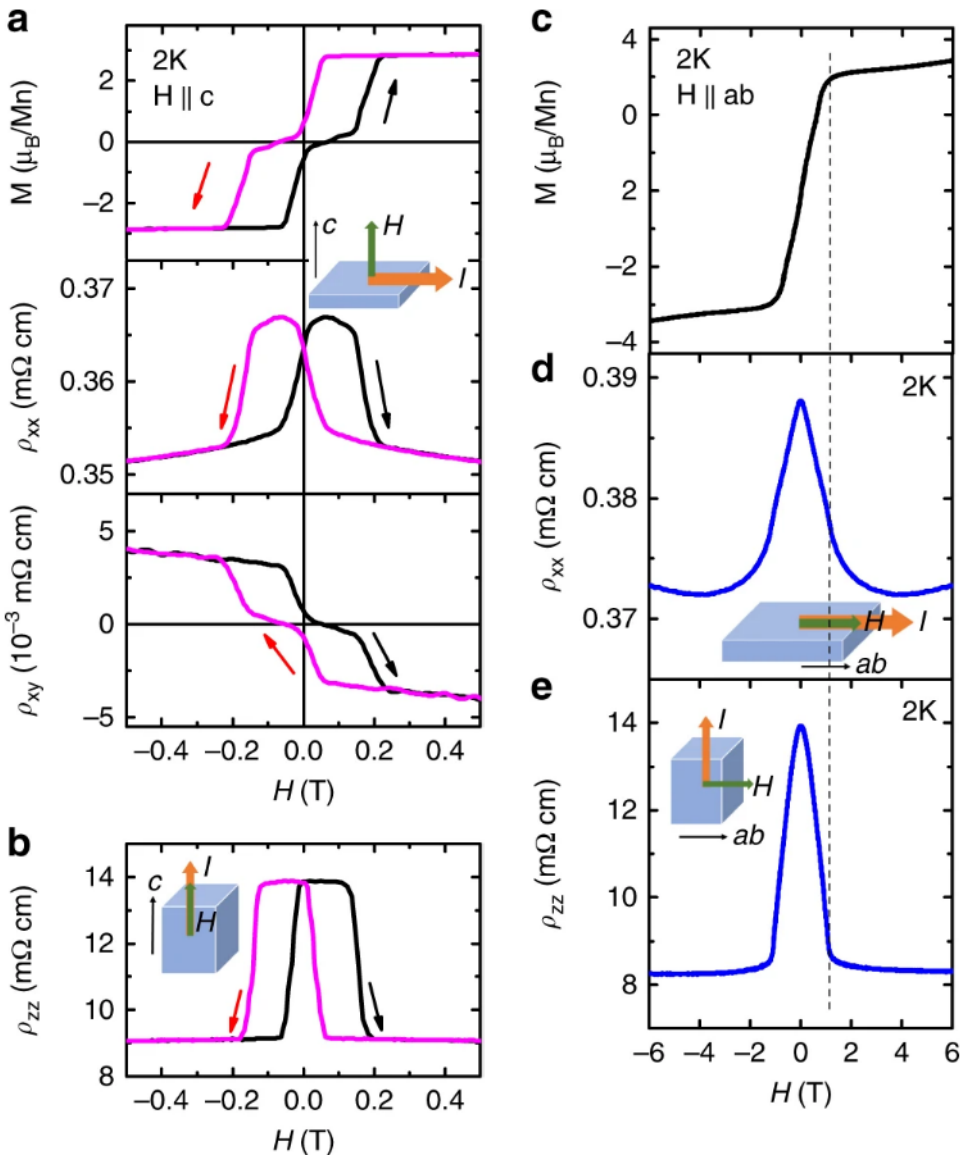

Figure 3.4: (a) Isothermal magnetization with $H \parallel c$, transverse magnetoresistivity ρ_{xx}, and Hall resistivity ρ_{xy} at 2 K with $I \| ab$ and $H \parallel c$. (b) The longitudinal magnetoresistivity of ρ_{zz}, at 2 K with $I \| H \parallel$ c. (c) Isothermal magnetization with $H \| ab$ at 2 K. (d) Longitudinal magnetoresistivity ρ_{xx}, at 2 K with $I \| H \| ab$. (e) Transverse magnetoresistivity ρ_{zz}, at 2 K with $I \| c$ and $H \| ab$.

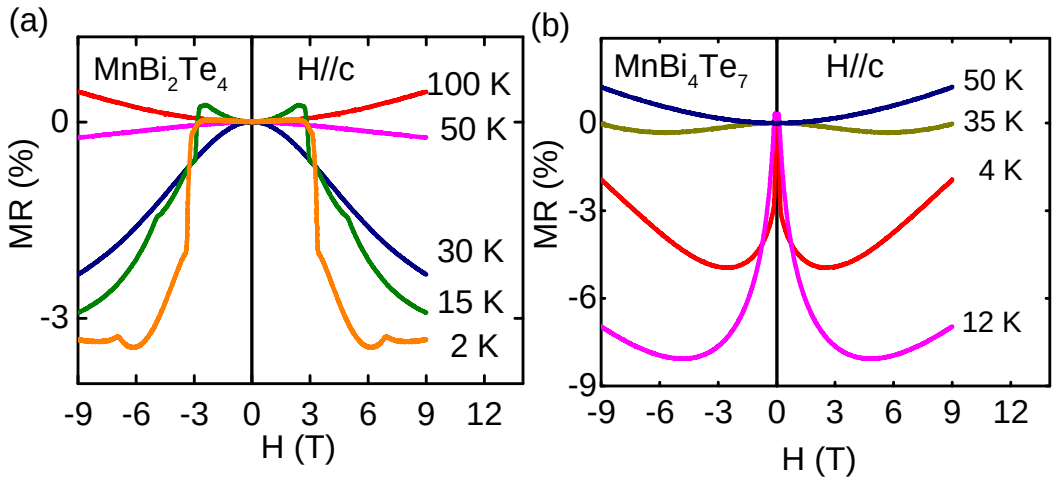

Figure 3.5: Transverse magnetoresistance measured with $H \parallel c$ and $I \parallel ab$ for (a) $MnBi_2Te_4$ and (b) $MnBi_4Te_7$ at various temperatures.

more prominent evidence of evolving magnetism. In Fig. 3.4 (b), the ρ_{zz} drops by about 50% above the saturation field for $H \parallel c$. In Fig. 3.4(c)-(e), we compare the ρ_{zz}, ρ_{xx}, and $M(H)$ for $H \parallel ab$. From zero field to 1.0 T, ρ_{zz} decreases by 39%. Our data show that the transition from AFM to FM spin alignment along the c axis has much stronger effect on ρ_{zz} than ρ_{xx}, because the spin-flip scattering along c is more affected due to its A-type magnetic structure. This provides us with an additional probe to understand the nature of the magnetism.

Figure 3.5 show the transverse magnetoresistance (TMR) for $MnBi_2Te_4$ and $MnBi_4Te_7$ at high field up to 9 T, defined as MR=(ρ_{xx} (H)-ρ_{xx} (0))/ ρ_{xx} (0). For $MnBi_2Te_4$ at lowest temperatures, the MR is slightly positive near the spin-flop field, and then negative above the spin-flop field beyond magnetic saturation. The negative MR persists above the transition temperature, and only become positive above 50 K. The similar feature of negative MR is seen in $MnBi_4Te_7$. For $MnBi_4Te_7$, the MR appears as the overall "W" shape of the TMR for all samples. In Fig. 3.5(b) for $MnBi_4Te_7$, the "W" shape becomes deeper with increasing temperature, with the largest negative TMR of 8% appearing at 12 K, which is close to T_N. Above T_N, it starts to become shallower and finally transforms into an ordinary parabolic shape at 50 K. The overall "W" shape can be understood in the framework of FM fluctuations. Above 50 K, the lack of magnetic fluctuations leads to the parabolic

TMR. Upon cooling, FM fluctuations begin to appear and become increasingly stronger and maximized around T_N. As a result, the summation of the positive parabolic TMR and the negative TMR arising from the FM fluctuations under fields leads to a progressively deeper "W" shape of TMR upon cooling. Below T_N, the FM fluctuations are reduced, but still with a strong presence, leading to the shallower "W" shape under field. The difference between the two figures again lies in the fact that the interlayer AFM exchange is a lot weaker in $MnBi_4Te_7$, so the magnitude of negative MR from the fluctuations are readily comparable at low field to the positive MR from the phonon contributions. So for $MnBi_2Te_4$, the magnetic fluctuations is much stronger and may require a field larger than 9 T to observe the "W" shape.

3.5 3D magnetism revealed by single crystal neutron scattering

To confirm the long-range magnetic order in $MnBi_4Te_7$, in collaboration with Huibo Cao's group at Oak Ridge National Lab, we have performed single crystal neutron diffraction and compared it with that of $MnBi_2Te_4$ [72]. Data were taken at the temperature above the transition for the nuclear structure, and below the transition for the magnetic structure refinement. The result provides direct evidence of the magnetic structure that we deduced from the magnetic and transport property measurements. The structural refinement using nuclear peak from the high temperature data are reported in [72]. Here we would like to still focus on the result on the magnetic peaks in $MnBi_2Te_4$ and $MnBi_4Te_7$.

A-type magnetic structure is confirmed for both compounds. For $MnBi_2Te_4$ with a space group of R-3m, its magnetic space group is R_I-3c and the propagation vector is (0, 0, 3/2). For $MnBi_4Te_7$ with space group P-3m1, its magnetic space group is P_c-3c1 and the propagation vector is (0, 0, 1/2).

The magnetic order parameters are shown in Figure 3.6. The critical behavior of the magnetic phase transitions can be analyzed using a power-law fit $I = A(\frac{T_M - T}{T_M})^{2\beta} + B$, where T_M is the critical temperature for magnetic phase transitions, β is the order parameter

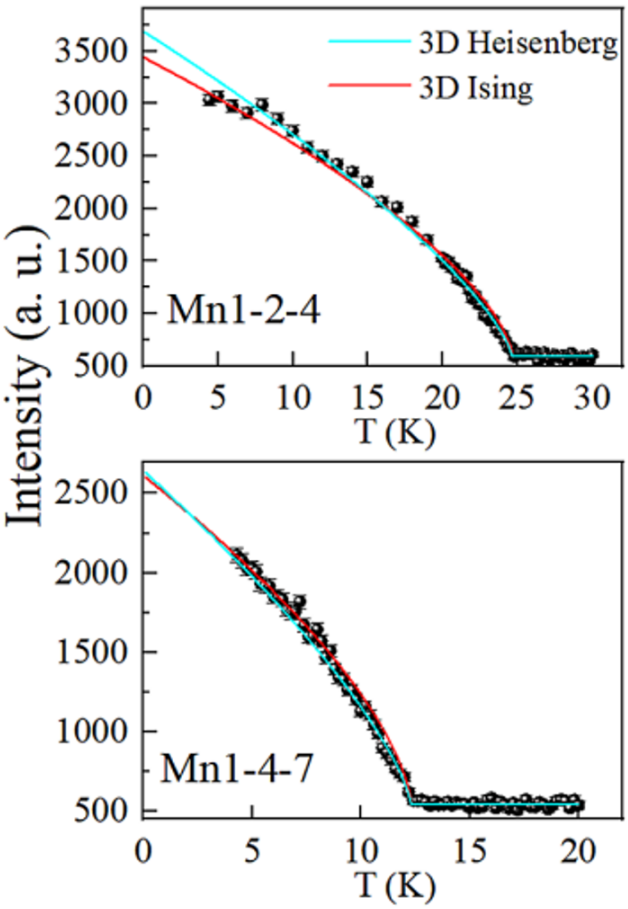

Figure 3.6: Magnetic order parameters upon warming at the magnetic reflections (-1, 0, 0.5), (0, 1, 1.5) for $MnBi_2Te_4$ and $MnBi_4Te_7$, respectively. Solid lines represent the fits using the 3D Heisenberg ($\beta = 0.367$) and 3D Ising ($\beta = 0.326$) models. The image is taken from [81].

critical exponent and A and B are just constants [82–84]. The fitting yields 3D critical exponents rather than 2D ones. For example, in Figure 3.6, for $MnBi_2Te_4$, the fitting results in $\beta = 0.367$ from 20 K to 30 K and 0.326 from 4 to 20 K. While the former agrees with the three dimensional Heisenberg model [82], the latter suggests the three dimensional Ising model (3DIM) [83].

At the first glance, a 3D feature of the magnetic model for the whole family compounds is unexpected given the fact that the crystal structure is characterized by the well-separated magnetic layers. However, a recent inelastic neutron scattering work on the powder $MnBi_2Te_4$ has disclosed that the magnetic interactions are Ising-like with strong interlayer exchange interactions [70]. This indicates that the interlayer magnetic interactions could be significant even though the inter-magnetic layers are considerably distant. The critical behavior of the 3DIM adopted in $MnBi_2Te_4$ and $MnBi_4Te_7$ is consistent with the Ising-like nature from the inelastic neutron scattering results [70, 85]. The power-law behavior can be extrapolated to the zero temperature limit for all the cases, allowing us to evaluate the ordered magnetic moment at zero temperature. Following the exponent parameters of the 3DIM and using the magnetic moment from the magnetic structure refinement at 4.5 K, we obtained the ordered magnetic moments of 4.9(1) μ_B and 4.6(1) μ_B for $MnBi_2Te_4$ and $MnBi_4Te_7$, respectively. These values are close to the expected totally ordered moment of 5 μ_B for Mn^{2+} ions.

3.6 Z_2 AFM TI revealed by DFT calculation

$MnBi_4Te_7$ crystallizes in the space group P-3m1 (No. 164). By taking into account the A-type AFM, the primitive cell doubles along the c axis, rendering a magnetic space group P_c-3c1 (No. 165.96) under the Belov-Neronova-Smirnova notation as shown in Fig. 3.2. This magnetic space group is derived from its nonmagnetic space group by adding an extra sublattice generated by an operation that combines time-reversal T with a fractional translation $\tau_{1/2}$. Then the full magnetic group is built as $GM = G + GS$, where S is a combinatory symmetry $S = T\tau_{1/2}$ with $\tau_{1/2}$ the half translation along the c axis of the AFM primitive

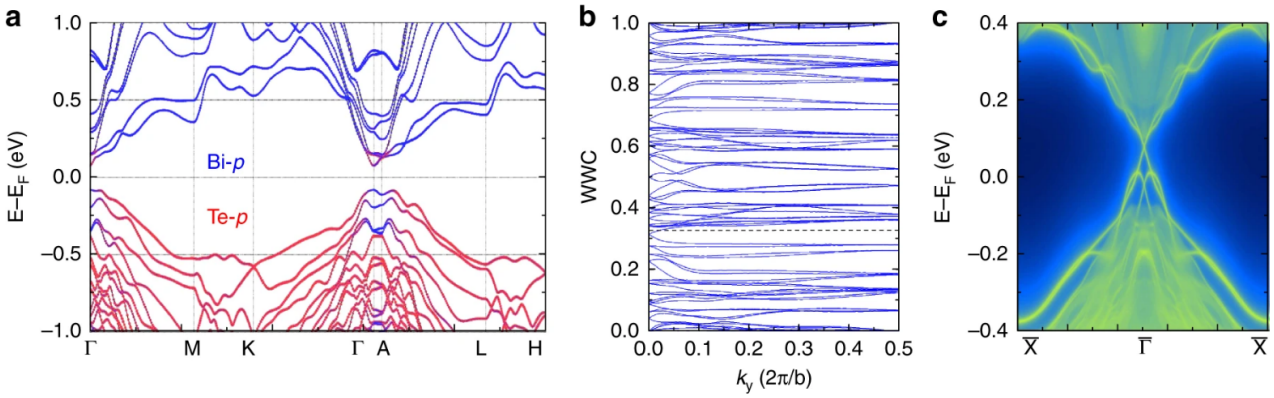

Figure 3.7: Topological properties of bulk AFM $MnBi_4Te_7$ predicted by first-principles calculations. (a) Band structure with the projection of Bloch eigenstates onto Bi-p (blue) and Se-p (red) orbitals. SOC is included. (b) Evolution of Wannier charge centers (WCCs) for $k_z = 0$, indicating a nontrivial topological invariant Z_2= 1. (c) Surface spectra of (010) side surface, showing a gapless Dirac cone protected by S symmetry.

cell. Although the explicit T-symmetry is broken, the S symmetry (also referred to nonsymmorphic time-reversal) still exists in bulk $MnBi_4Te_7$. In addition, $MnBi_4Te_7$ has inversion symmetry P, while the square of the symmetry operator PS equals -1 at an arbitrary k in momentum space. Therefore, analogous to TI with T-symmetry where Kramer's degeneracy is induced by T^2 = -1, in $MnBi_4Te_7$ the existence of the PS symmetry ensures an equivalent Kramer's degeneracy in the whole Brillion zone, and thus a Z_2 topological classification.

Figure 3.7(a) shows the calculated band structure of bulk AFM $MnBi_4Te_7$ with the presence of spin-orbit coupling. The conduction band minimum is located at the Γ point, while the valence band maximum in the vicinity of Γ shows a slightly curved feature. The calculated bulk band gap is about 160 meV. The projection of band eigenstates onto the p-orbitals of Bi and Te (as indicated by the blue and red coloring) clearly indicates an inverted order between several conduction and valence bands around the Γ point, which is strong evidence of the possible nontrivial topological nature. On the other hand, the Mn-3d^5 states form nearly flat bands far away from the Fermi level, indicating that the main effect of Mn is to break T-symmetry by introducing staggered Zeeman field into the low-energy

Hamiltonian.

To determine the topological properties of AFM $MnBi_4Te_7$, we first apply the Fu-Kane formula [86] to calculate the Z_2 invariant. The topological insulator phase of antiferromagnetic materials is protected by S symmetry, under which there are only four invariant k-points forming a 2D plane in the momentum space. Thus, analogous to weak Z_2 indices in nonmagnetic materials, the S symmetry indeed protects weak Z_2 topological phases in antiferromagnetic materials. In AFM $MnBi_4Te_7$, four TRIM points, including Γ(0,0,0) and three equivalent $M(\pi,0,0)$, need to be considered here with $k \cdot \tau_{1/2} = n\pi$. Due to the aforementioned band inversion at the Γ point, we find that the parities for the occupied bands at Γ are opposite to that of the other three M points, indicating a nontrivial $Z_2 = 1$. To verify our results, we also calculate the evolution of Wannier charge centers (WCCs) using the Wilson loop approach [87]. As show in Fig. 3.7(b), the largest gap function and the WCCs line cross each other an odd number of times through the evolution, confirming that $MnBi_4Te_7$ is indeed a Z_2 AFM topological insulator. Compared with TIs with T-symmetry, the protection of gapless surface states in AFM TIs requires that the cleaved surface respects S symmetry that contains translation along the c axis. Figure 3.7(c) clearly shows the gapless surface Dirac cone at the Γ point for the (010) surface, partially validating the bulk-surface correspondence of $MnBi_4Te_7$ as an AFM TI. The easy-cleaved (001) plane, where the S symmetry is broken, are measured by ARPES and compared with our theoretical calculations, as discussed in the following.

3.7 Surface and bulk states measured by ARPES

As mentioned earlier, unlike $MnBi_2Te_4$, $MnBi_4Te_7$ can terminate on two different sublattice surfaces on the (001) plane, i.e., the [Bi_2Te_3] QL termination and the [$MnBi_2Te_4$] SL termination, resulting in different surface states. ARPES with 47 eV, linear horizontal polarized light and a small beam spot reveals two different types of $E-k$ maps by scanning across different parts of the sample in real space, as plotted in Figs. 3.8(d,e) and Figs. 3.8(h,i). There are several distinguishing features between the two types of surface spectra:

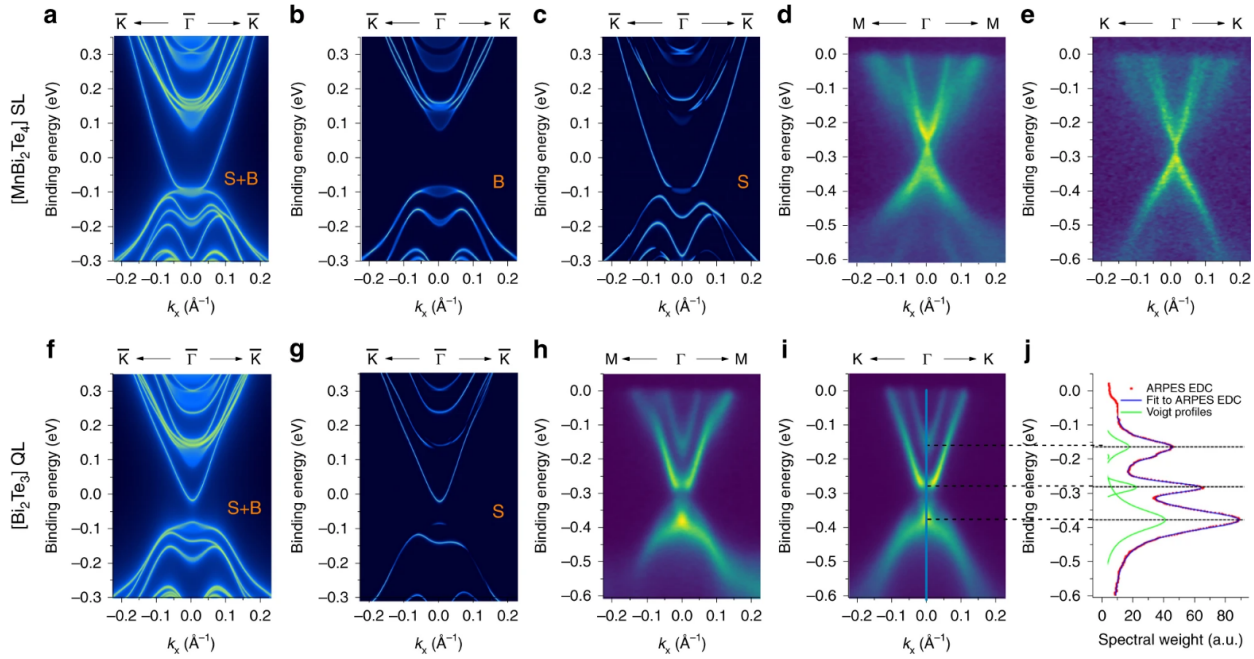

Figure 3.8: Comparison between ARPES-measured and DFT-calculated surface states. (a–c) The DFT-calculated $k-E$ map along $\overline{K} \longleftarrow \overline{\Gamma} \longrightarrow \overline{K}$ on the $[MnBi_2Te_4]$ SL termination: (a) surface and bulk (S+B) spectrum, (b) bulk only, and (c) surface only. (d, e) The experimental ARPES spectrum on the $[MnBi_2Te_4]$ SL termination obtained with 47 eV, linear horizontal light: (d) along $M \longleftarrow \Gamma \longrightarrow M$, (e) along $K \longleftarrow \Gamma \longrightarrow K$ high symmetry direction. (f, g) The DFT-calculated $k-E$ map along $\overline{K} \longleftarrow \overline{\Gamma} \longrightarrow \overline{K}$ on the $[Bi_2Te_3]$ QL termination: (f) surface and bulk (S+B) spectrum, (g) surface only. (h, i) The experimental ARPES spectrum on the $[Bi_2Te_3]$ QL termination obtained with 47 eV, linear horizontal light: (h) along $M \longleftarrow \Gamma \longrightarrow M$, (i) along $\overline{K} \longleftarrow \overline{\Gamma} \longrightarrow \overline{K}$ high symmetry direction. (j) The EDC plot at the Γ point (blue-line cut in i) showing three main peaks corresponding to the bulk conduction band, surface conduction band, and mixed surface/bulk valence band. The green curve shows the fitted Voigt profile peaks which sum to the blue curve.

Figs. 3.8(h,i) appear to show a gap with massive quasiparticles while Figs. 3.8(d,e) show a sharp Dirac-like crossing, possibly with a small gap. The spectra of Figs. 3.8(d,e) are reminiscent of recent high resolution ARPES spectra of the $MnBi_2Te_4$ compound [66, 68, 69, 74] that show Dirac-like spectra, and we assign these states to the [$MnBi_2Te_4$] SL termination, while we assign the other set of surface states to the [Bi_2Te_3] QL termination.

On these two terminations, symmetry operations combined with $\tau_{1/2}$ are not preserved. In the ideal case that the surface magnetic structure perfectly inherits the bulk property, due to the A-type out-of-plane magnetization of the Mn sublayers, the gapped surface states are described by adding an exchange term to the ordinary Rashba-type surface Hamiltonian for TI with T symmetry, i.e., $H_{surf}(k) = (\sigma_x k_y - \sigma_y k_x) + m_{S/Q}\sigma_z$, where σ is the Pauli matrix for spin, and $m_{S/Q}$ the surface exchange field that distinguishes the [$MnBi_2Te_4$] SL and [Bi_2Te_3] QL surfaces. Our calculation shows that the surface state terminated at the [Bi_2Te_3] QL has a massive Dirac cone with a surface gap around 60 meV (Fig. 3.8(f,g)), and an overall structure that agrees very well with the experimental data of Fig. 3.8(h,i), confirming the assignment of the experimental data as arising from the [Bi_2Te_3] QL termination. When comparing Fig. 3.8(i) with the bulk states calculated by DFT (Fig. 3.8 (b)), we can easily distinguish the surface states from the bulk states. To measure gap sizes in Fig. 3.8(i), we extract an energy distribution curve (EDC) at the Γ point and fit it to several Voigt profiles, as shown in Fig. 3.8(j). We find that despite the appearance of some spectral weight in the gapped region in Fig. 3.8(i), the EDC does not show any signature of a peak in the gapped region, indicating that the surface state is gapped by approximately 100 meV while the bulk gap is nearly 225 meV.

The equivalent calculation on the [$MnBi_2Te_4$] SL termination is shown in Figs. 3.8(a,c) and does not agree well with the experimental data of Fig. 3.8(d,e). While the theory shows that surface states merge with the bulk valence bands, the experiment suggests a Dirac-like structure inside the gap. By taking full account of experimental resolution functions in both momentum directions and in energy, the ARPES data are consistent with either no gap or a maximum gap size of 10 meV. A similar feature, i.e., nearly gapless surface Dirac

cone at the SL termination, was also observed in $MnBi_2Te_4$ single crystals [66, 68, 69, 74], where the deviation between ARPES and DFT calculation is suggested to be due to the surface-mediated spin reconstruction at the top layers of the [$MnBi_2Te_4$] SL termination.

Figure 3.9(a,b) show stacks of measured isoenergy surfaces for the [$MnBi_2Te_4$] SL and [Bi_2Te_3] QL terminations over a wide range of energies both above and below the Dirac point, while Fig. 3.9(c) shows equivalent calculations for the [Bi_2Te_3] QL termination. The six-fold symmetric isoenergy surfaces are seen in all cases, including the hexagonal warping or snow-flake effect [88]. We comment that while both terminations collapse to a single resolution-limited point in k-space in the middle panels in Figs. 3.9 (a,b), this is expected whether or not there is a gapless or gapped Dirac point, due to the broad energy band width of the nearby valence and conduction bands (Fig. 3.8(j)).

3.8 Summary and outlooks

We have shown $MnBi_4Te_7$ is a vdW AFM TI. It is a 1:1 superlattice composing the building blocks of AFM TI [$MnBi_2Te_4$] and T-invariant TI [Bi_2Te_3]. Our realization of the superlattice design has three advantages. As expected, [Bi_2Te_3] serves as a "buffer layer" that separates and thus effectively decreases the AFM coupling between the two neighboring [$MnBi_2Te_4$] SLs, reducing the necessary weaker magnetic field to trigger the QAH. Second, by interlayer coupling between [Bi_2Te_3] QL and the adjacent [$MnBi_2Te_4$] SLs, the SOC-induced nontrivial topology of [Bi_2Te_3] ensures the band inversion in the 2D limit. As a result, QAH is well expected in few-layer $MnBi_4Te_7$. Third, when $MnBi_4Te_7$ is exfoliated into the 2D limit, natural heterostructures are made, which provides more 2D configurations than $MnBi_2Te_4$ or Bi_2Te_3 single crystal since the latter ones are only stacked by one type of building block. One can exfoliate $MnBi_4Te_7$ with designed termination, with different film thickness and magnetization (require a low magnetic field). For example, two types of three-layer systems with distinct topological properties, [$MnBi_2Te_4$]/[Bi_2Te_3]/[$MnBi_2Te_4$] and [Bi_2Te_3]/[$MnBi_2Te_4$]/[Bi_2Te_3], should be easily obtained by exfoliation. Recent calculations show that [$MnBi_2Te_4$]/[Bi_2Te_3]/[$MnBi_2Te_4$] is a QAH insulator if a small mag-

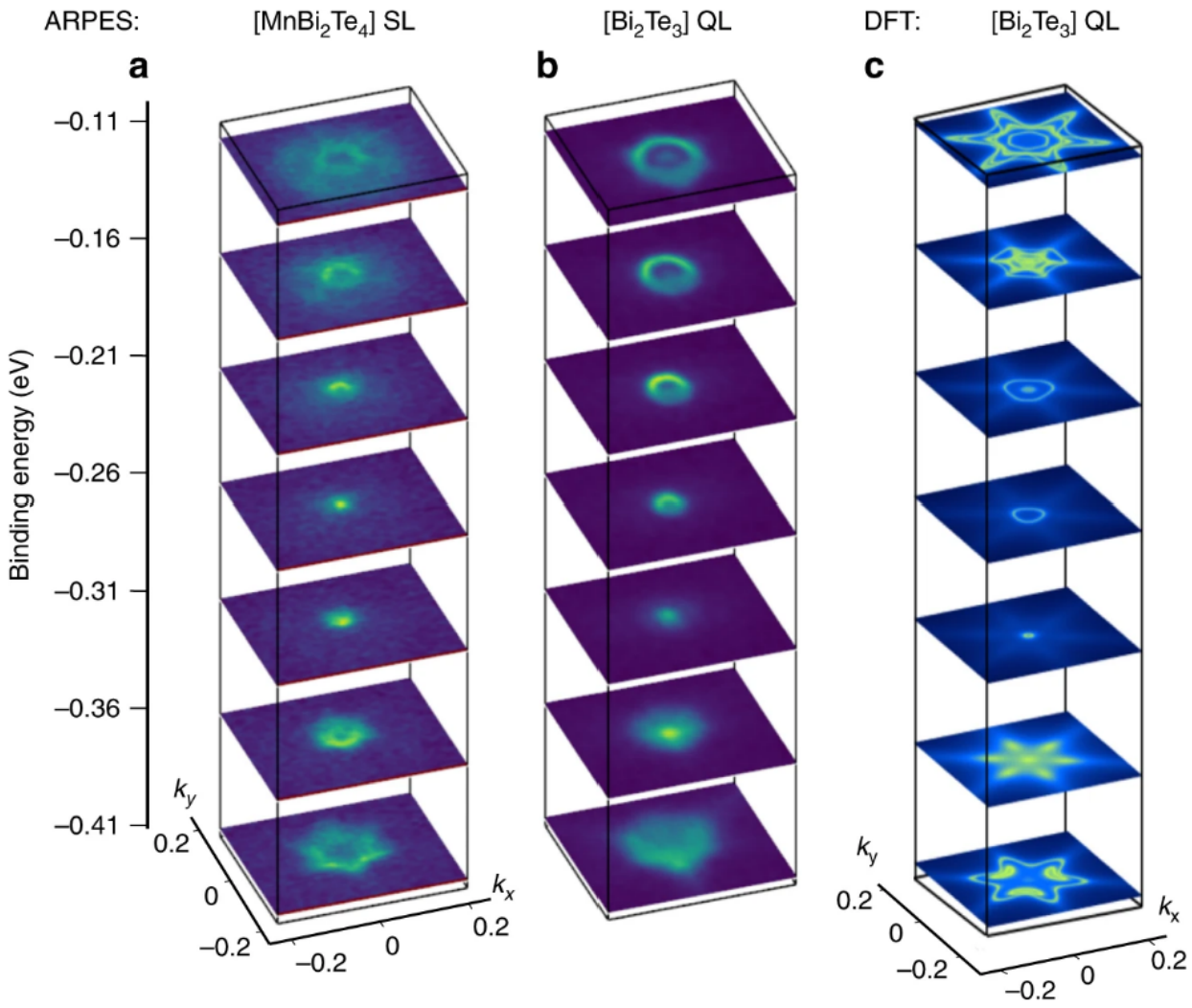

Figure 3.9: Experimental and theoretical constant-energy slices. (a, b) ARPES constant energy surfaces sliced at every 50 meV at SL and QL surface termination. (c) The same contours calculated by DFT for the QL termination. The six-fold symmetric snowflake-like surfaces are seen in all cases.

netic field around 0.2 T is applied to stabilize the forced FM phase. On the other hand, $[Bi_2Te_3]/[MnBi_2Te_4]/[Bi_2Te_3]$ is suggested to be a QSH insulator with time-reversal breaking which cannot be achieved from the thin films of either $MnBi_2Te_4$ or Bi_2Te_3. Therefore, the 2D version exfoliated from bulk vdW TI $MnBi_4Te_7$ may pave an avenue to chase the long-sought emergent properties such as QAH effect and QSH effect.

CHAPTER 4

The discovery of $MnBi_8Te_{13}$: the first intrinsic ferromagnetic axion insulator

This chapter is mostly adapted from [80]. This work was done in collaboration with Dan Dessau's group at University of Colorado, Boulder on ARPES measurements, Tay-Rong Chang's group at National Cheng Kung University on first-principles band structure calculations, Dongsheng Li's group from Pacific Northwest National Laboratory on STEM imaging, Huibo Cao's group at Oak Ridge National Lab on neutron diffraction measurements.

4.1 Introduction

Since the discovery $MnBi_2Te_4$ as the first intrinsic AFM TI, various attempts have been made to find related materials in order to reduce the AFM coupling and obtain FM topological materials. In Chapter 3, we show by creating natural heterostructures $MnBi_4Te_7$, we can achieve a weakly coupled AFM which can be easily polarized to FM state with merely 0.22 T. Although this value is 40 times smaller than that in $MnBi_2Te_4$, a finite field is still necessary to force the sample to enter the FM state for QAHE. This greatly hinders application with QAHE when one needs to couple QAHE with time reversal symmetry preserving systems such as s-wave superconductor to look for associated phenomena like Majorana modes. Therefore, it is still desirable to further reduce the interlayer coupling so the FM state can be obtained spontaneously without any field.

Motivated by our previous success in growing natural heterostructure $MnBi_4Te_7$, we take a step further in looking for higher-n members in $MnBi_{2n}Te_{3n+1}$, i.e. inserting more nonmag-

netic [Bi_2Te_3] layers in between [$MnBi_2Te_4$]. By this rational design, we made $MnBi_8Te_{13}$ for the first time. Through our studies, $MnBi_8Te_{13}$ was discovered to be the first intrinsic FM topological insulator. The evolution of crystal and magnetic structure of $MnBi_{2n}Te_{3n+1}$ from $n = 1$ to $n = 4$ are shown in Fig. 4.1.

In this chapter, we will first overview the growth and characterization of $MnBi_{2n}Te_{3n+1}$ (n = 3 and 4). We then compare the thermodynamic, transport and neutron diffraction measurements of $MnBi_8Te_{13}$ with $MnBi_6Te_{10}$. Our data show that while $MnBi_6Te_{10}$ is AFM with the ordering temperature of 11 K, $MnBi_8Te_{13}$ manifests long-range Ising ferromagnetism below 10.5 K with strong coupling between magnetism and charge carriers even when the adjacent [$MnBi_2Te_4$] is 44.1 Å apart. Our first-principles calculations and angle-resolved photoemission spectroscopy (ARPES) measurements further suggest that $MnBi_8Te_{13}$ is an intrinsic FM axion insulator. With the natural heterostructure nature of $MnBi_8Te_{13}$ that allows it to be exfoliated to different thin-film device, our finding may provide a superior material realization to explore zero-field QAH effect, quantized topological magnetoelectric effect, and associated phenomena.

4.2 Growth and Characterization

One of the big challenges of studying $MnBi_8Te_{13}$ lies in the crystal growth. Since $MnBi_{2n}Te_{3n+1}$ compounds are metastable phases, their crystal growths are limited to a temperature window of a couple of degrees. This situation becomes even more arduous with increasing n, for example, we found that the growth window for $MnBi_8Te_{13}$ is extremely narrow like half a degree and very close to the melting point of Bi_2Te_3 flux. Special techniques were employed to ensure the success of the synthesis. Like $MnBi_4Te_7$, $MnBi_6Te_{10}$ and $MnBi_8Te_{13}$ are grown by Bi_2Te_3 flux. Experimentally, we found that a growth involving mixing Mn, Bi, and Te at a ratio of MnTe:Bi_2Te_3=$x : 100 - x$ with 10< x <20 can all give a good yield [50, 62, 80, 89]. For a larger n, a smaller x is preferred so there can be enough flux. In general, x = 15 is used. The mixture first is placed in an alumina crucible and sealed under 1/3 atm of Ar inside a quartz tube. The ampule was heated first to 900 °C for

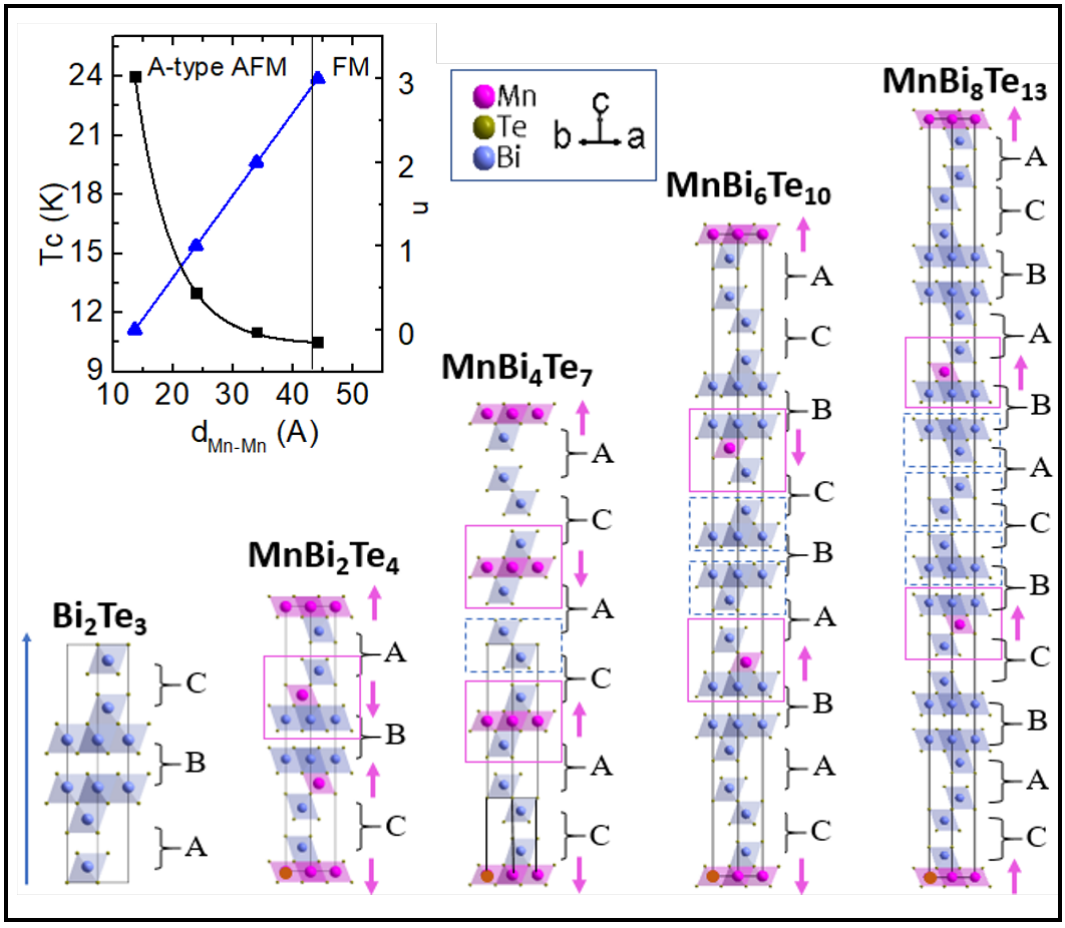

Figure 4.1: Schematic drawing of the crystal and magnetic structure of $MnBi_{2n}Te_{3n+1}$ (n = 0, 1, 2, 3 and 4) with the stacking sequence listed. A, B and C represents the bilayers of $BiTe_6$ octahedra whose bottom Te atoms, center Bi atoms and top Te atoms are on the cell edges, respectively. Magenta arrow: magnetic structure in the order state. Blue block: edge-sharing $BiTe_6$ octahedra; Magenta block: edge-sharing $MnTe_6$ octahedra, which are connected to the blue block via edge-sharing. Inset: Tc (The critical temperatures) vs. d_{Mn-Mn} (the interlayer distance between the adjacent Mn-Mn layers) and n vs. d_{Mn-Mn} in $MnBi_{2n}Te_{3n+1}$ (n = 1, 2, 3 and 4).

a few hours to ensure a good mixing, quickly cooled to 600 °C followed by slow cooling down the target decanting temperature T_d in 3 days. After dwelling at T_d for 3 days, cm-sized plate-like single crystals is separated from the flux using a centrifuge.

Because all $MnBi_{2n}Te_{3n+1}$ phases are thermodynamically metastable and only exist in a very limited temperature range, temperature control is the key to obtaining the right phase. In fact, the phase of the obtained single crystals depends solely on the decanting temperature T_d, whereas the x in the initial concentration only affects the morphology of the crystals. Therefore, the same furnace was used for all trials to avoid furnace-to-furnace temperature variations. The location in the furnace, the length of the quartz tube, and the height of the crucible within the tube, were also kept about the same for the same purpose when repeating a growth. If the use of a second furnace is desired, we need to perform a careful calibration first by an external thermocouple, and by performing a test growth for $MnBi_4Te_7$ to ensure that we hit the growth window.

The systematic way to determinate the growth window for each phase is as follows, taking $MnBi_8Te_{13}$ as an example. We first set the decanting temperature to be some T_1, and then decanted the growth by a pre-warmed centrifuge. If there is no liquid flux out during the centrifuging process, it meant T_1 is so low that all materials have been in the solid state at T_1. Then in the next growth, we increase the decanting temperature a little to T_2 (this could be done by carefully moving the synthesis in different locations inside the furnace), then if we get $MnBi_6Te_{10}$ or $MnBi_4Te_7$ after decanting, this means T_2 is too high and we miss the growth window of $MnBi_8Te_{13}$. Then we decrease the decanting temperature to be between T_1 and T_2. The trials continue until we hit the right temperature for $MnBi_8Te_{13}$. The ideal temperature for each phase is summarized in Table 4.1. This is only a relative guide, but again, the same trial process is needed when a new furnace is used.

In particular case of $MnBi_8Te_{13}$, we do not always see well-separated single crystals, but rather a few crystals on top of a chunk inside the crucible. This is because the decanting temperature is so close to the solidification temperature that during the process of decanting, only the liquid on the top was successfully separated from the $MnBi_8Te_{13}$ crystals. To achieve

Table 4.1: Summary table of the chemical, structural, magnetic, transport properties of $MnBi_{2n}Te_{3n+1}$ from $n = 1$ to 4. * The elemental ratio were determined by WDS. Anomalous Hall angle (AHA) are calculated from the transport data.

	$MnBi_2Te_4$	$MnBi_4Te_7$	$MnBi_6Te_{10}$	$MnBi_8Te_{13}$
Elemental ratio*	0.91(1):2.15(2):4	0.79(2):4.29(8):7	0.79(1):6.30(2):10	0.74(3):8.2(1):13
n	1	2	3	4
Space Group	R-3m	P-3m1	R-3m	R-3m
a (Å)	4.3243(2)	4.3716(3)	4.3710(5)	4.3714(1)
$d_{Mn\text{-}Mn}$ (Å)	13.629(1)	23.848(2)	33.944(4)	44.107(2)
T_{growth} (°C)	587	585	583	582
Magnetism	AFM	AFM	AFM	FM
T_N,T_C (K)	24	13	11	10.5
H_{sat}^{c} (T)	7.8	0.22	0.2	0.12
H_{sat}^{ab} (T)	11	1.2	1.2	1.2
M_{7T}^{c} (μ_B/Mn)	4.2(1)	4.2(1)	4.4(1)	5.1(2)
AHA	1%	0.8%	0.2%	0.1%

a better spin-out, some additional protocols were used to slow down the cooling during the centrifuge process. For example, the centrifuge cell was heated in a furnace shortly and quickly moved back to the centrifuge seconds before the growth ampule is dropped in. An additional quartz shell was painted with expired Ag paste to cover the sample quartz ampule to provide better thermal insulation.

Next, to find out the phase of single crystals from the growth, one quick way is to measure XRD on their flat $(00L)$ surfaces. Because Bi_2Te_3 and $MnBi_{2n}Te_{3n+1}$ each have very distinct lattice parameter c, their Bragg reflections on $(00L)$ are completely different.

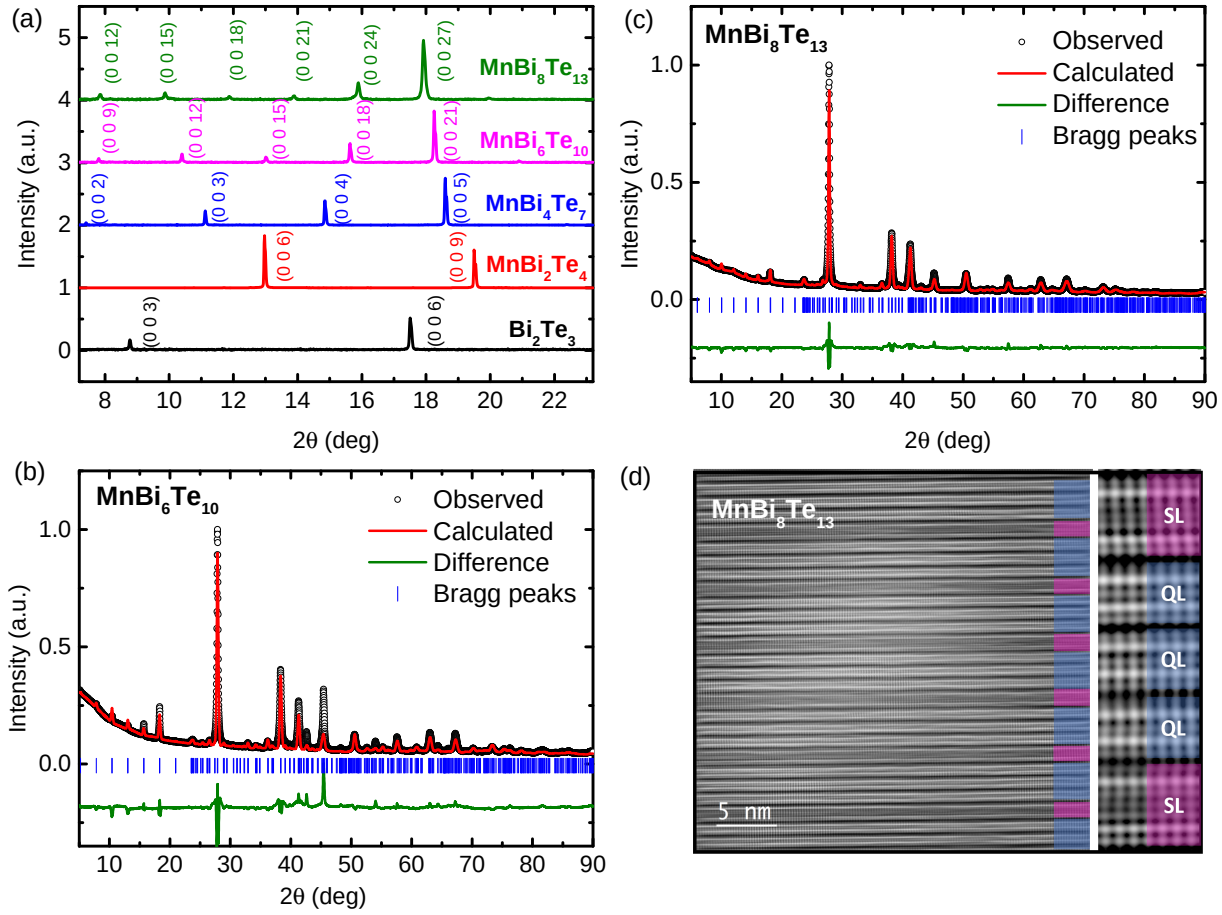

Figure 4.2: (a) Distinct X-ray reflections on the $(00L)$ surfaces of Bi_2Te_3, $MnBi_2Te_4$, $MnBi_4Te_7$, $MnBi_6Te_{10}$ and $MnBi_8Te_{13}$. (b, c) Powder X-ray diffraction and the refinement of $MnBi_6Te_{10}$ and $MnBi_8Te_{13}$ respectively. (d) STEM image of $MnBi_8Te_{13}$ made on a sample after being cut by focused-ion-beam. The purple and the blue blocks mark the $[MnBi_2Te_4]$ SL and$[Bi_2Te_3]$ QL respectively.

As c increase with n, the Bragg peaks become more densely packed, as shown in Fig. 4.2 (a). Therefore, a quick surface scan allows us to easily determine the phase of each piece. It is worth noting that especially since the growth window for $MnBi_{2n}Te_{3n+1}$ is narrow, the temperature may sometimes lie at the boundary of two windows and give an internally mixed phases that may not show up in the surface X-ray scan. For higher-n growth, the decanting temperature is closer to the melting point of flux, so the chance of the intergrowth between Bi_2Te_3 and $MnBi_{2n}Te_{3n+1}$ also increases. Therefore, extra care is needed to select the piece for measurement by powder XRD. In Figure 4.2 (b)-(c), we show the powder X-ray spectra and the refinements of $MnBi_6Te_{10}$ and $MnBi_8Te_{13}$ respectively. The refined lattice parameter table is summarized in Table 4.1. The detailed atomic positions determined by powder XRD is included in Tables B.2 and B.3. We also show in the summary table the chemical analysis performed by WDS. In general, $MnBi_{2n}Te_{3n+1}$ are deficient in Mn compared with the ideal chemical formula. In addition, we observe a reduction in Mn concentration with higher n which is consistent with our neutron scattering data that will be shown later.

From the refined structure, unsurprisingly, all $MnBi_{2n}Te_{3n+1}$ follow the same stacking rules, which are rationalized in [72]. The $MnBi_2Te_4$ layer is characterized by a monolayer of $MnTe_6$ octahedra sandwiched by two edge-sharing layers of $BiTe_6$ octahedra running along the c-axis. The Bi_2Te_3 are simply the two edge-sharing $BiTe_6$ octahedra stacked together. The distance between the nearest Mn-Mn interlayer is 13.6 $\AA$ for $MnBi_2Te_4$, 23.8 $\AA$ for $MnBi_4Te_7$ and 33.9 $\AA$ for $MnBi_6Te_{10}$, and 44.1 $\AA$ for $MnBi_8Te_{13}$, as shown in the inset of Fig. 4.1. Using Bi_2Te_3 as the starting point, along the c axis, the stacking of Bi_2Te_3 is -A-B-C-A-B-C-, where A, B and C represents the bilayers of $BiTe_6$ octahedra whose bottom Te atoms, center Bi atoms and top Te atoms are on the cell edges, respectively. "Mn" layer can replace "A" or "B" or "C" bilayers of $BiTe_6$ octahedra to make $MnBi_{2n}Te_{3n+1}$. For example, as shown in Fig. 4.1, for $MnBi_2Te_4$, the stacking is -Mn(B)-C-Mn(A)-B-Mn(C)-A-; for $MnBi_4Te_7$, the stacking is -Mn(B)-C-A-; for $MnBi_6Te_{10}$, the stacking is -Mn(B)-C-A-B-Mn(C)-AB-C-Mn(A)-B-C-A-; for $MnBi_8Te_{13}$, it is Mn(B)-C-A-B-C-Mn(A)-B-C-A-B-Mn(C)-A-B-C-A-. Therefore, with the stacking rule, we can easily assign the stacking

sequence for the yet-to-be-discovered higher n members of $MnBi_{2n}Te_{3n+1}$ or design new magnetic topological insulators with the QL and SL building blocks.

The formation of $MnBi_8Te_{13}$ is also visualized by the scanning transmission electron microscopy (STEM) image, as shown in Fig. 4.2 (d). The STEM image shows vdW structures, which is composed of repeating units of one SL block made of seven atomic layers and three consecutive QL blocks made of five atomic layers.

4.3 Magnetic and Transport properties of $MnBi_6Te_{10}$ and $MnBi_8Te_{13}$

4.3.1 Magnetic properties

The evolution of magnetism from AFM to FM in higher n $MnBi_{2n}Te_{3n+1}$ is well revealed in the magnetic and transport measurement. Figure 4.3 shows the measurement for $MnBi_4Te_7$, $MnBi_6Te_{10}$ and $MnBi_8Te_{13}$ as comparison. The magnetic properties for $MnBi_4Te_7$ have previously been described in Chapter 3. The same set of data are presented here in Fig. 4.3 (b), (e) and (h) for $MnBi_6Te_{10}$, and Fig. 4.3 (c), (f) and (i) for $MnBi_8Te_{13}$. We can observe an overall similarity between $MnBi_4Te_7$ and $MnBi_6Te_{10}$ data. Yet, sharp contrast was seen in $MnBi_8Te_{13}$. Firstly, the inset of Fig. 4.3 (b, c) present the specific heat data of $MnBi_6Te_{10}$ and $MnBi_8Te_{13}$. The specific heat anomaly associated with the magnetic phase transition marked by arrow suggest the ordering temperature to be 11.0 K for $MnBi_6Te_{10}$ and 10.5 K for $MnBi_8Te_{13}$, which are slightly lower than 13 K in $MnBi_4Te_7$. From the susceptibility curve in Fig. 4.3 (b), we observed a sharp cusp feature for $MnBi_6Te_{10}$ centering at 11.0 K in χ_c. Below that there is a small bifurcation between ZFC and FC curve under 9 K, similar to the ones in AFM $MnBi_2Te_4$ and $MnBi_4Te_7$. However, a much larger bifurcation of ZFC and FC data of χ_c appears below 10.5 K in $MnBi_8Te_{13}$ in Fig. 4.3 (c), where upon cooling the ZFC data decrease but the FC data increase, suggesting the formation of FM domains. Furthermore, at 2 K, the magnitude of the FC χ_c in $MnBi_8Te_{13}$ is by orders larger than that in AFM $MnBi_2Te_4$, $MnBi_4Te_7$ and $MnBi_6Te_{10}$. The evidence undoubtedly points to a distinct magnetic ground state in $MnBi_8Te_{13}$ compared to $MnBi_2Te_4$, $MnBi_4Te_7$ and

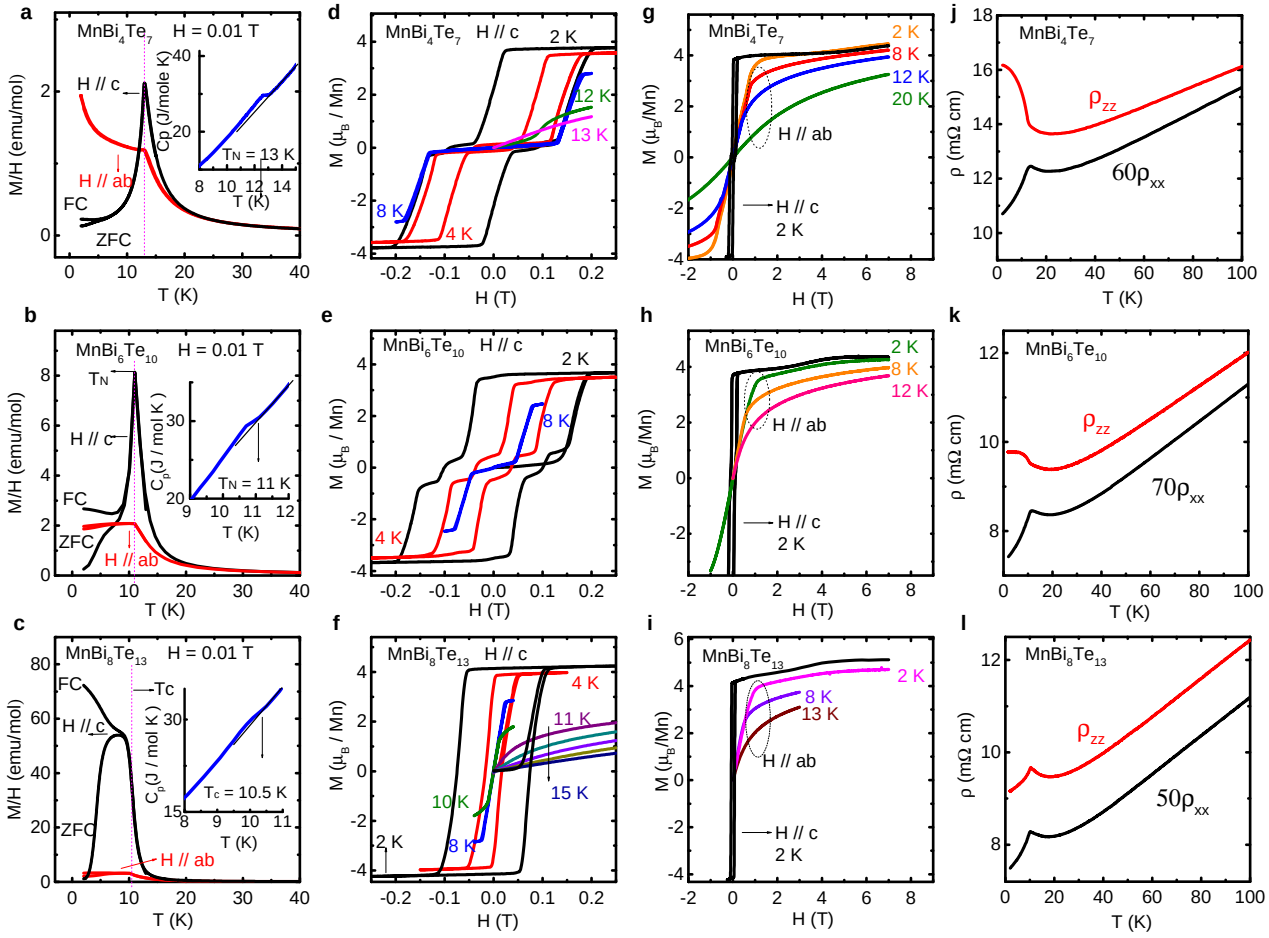

Figure 4.3: Temperature dependent magnetic, transport and specific heat properties of $MnBi_4Te_7$, $MnBi_6Te_{10}$ and $MnBi_8Te_{13}$. (a-c) The temperature dependent susceptibility taken at $H = 0.01$ T for $MnBi_{2n}Te_{3n+1}$ $(n = 2, 3, 4)$, respectively. Inset: The temperature dependent specific heat for the respective compound. The criterion to determine T_c and T_N are shown in the inset. (d-f) Magnetic hysteresis loop of isothermal magnetization under low field with $H \| c$ at various temperatures for the three compounds respectively. (g-i) Magnetic hysteresis loop of isothermal magnetization up to 7 T with $H \| ab$ and $H \| c$, for the three $MnBi_{2n}Te_{3n+1}$. (j-l) Temperature-dependent anisotropic resistivity, ρ_{xx} and ρ_{zz} for $MnBi_4Te_7$, $MnBi_6Te_{10}$ and $MnBi_8Te_{13}$.

$MnBi_6Te_{10}$, while $MnBi_6Te_{10}$ adopts the same magnetic structure as $MnBi_4Te_7$.

The ferromagnetism in $MnBi_8Te_{13}$ is further confirmed by the hysteresis loop of isothermal magnetization curves $M_c(H)$ ($H \| c$) shown in Fig. 4.3 (e, f) for $MnBi_6Te_{10}$ and $MnBi_8Te_{13}$. At 2 K, unlike the $M_c(H)$ data where multiple-step features are observed due to the spin-flop transition in $MnBi_2Te_4$ [53, 62] and spin-flip transition in $MnBi_4Te_7$ and $MnBi_6Te_{10}$, $M_c(H)$ in $MnBi_8Te_{13}$ shows a typical hysteresis loop for FM materials with the coercive field of H_c = 0.075 T and saturation remanence of M_r = 4.1 μ_B/Mn. Upon warming, H_c decreases as the hysteresis loop shrinks in area due to the enhanced thermal fluctuations. Figure 4.3(i) shows the $M_{ab}(H)$ and $M_c(H)$ of $MnBi_8Te_{13}$ up to 7 T, where a field about 1.1 T is required to force spins to saturate in the ab plane. This value is 1.13 T for $MnBi_6Te_{10}$ in Fig. 4.3 (h). The saturation moment measured at 7 T for $MnBi_8Te_{13}$ is M_s = 5.1(2) μ_B/Mn whereas it is 4.4(1) μ_B/Mn for $MnBi_6Te_{10}$. This suggests the mechanism causing the reduced Mn saturation moment is weaker in the FM state of $MnBi_8Te_{13}$—-in Chap 5 we will see the difference comes from the decreasing Mn_{Bi} formation with increasing n. The fitted Curie-Weiss temperatures of $MnBi_8Te_{13}$ are θ_w^{ab} = 12.8 K and θ_w^c = 12.1 K, confirming FM exchange interactions. The fitted effective moments are μ_{eff}^{ab} = 5.4μ_B/Mn and μ_{eff}^c=5.1μ_B/Mn, indicating weak single-ion anisotropy. Although the effective moment is smaller than 5.9 μ_B/Mn for a Mn^{2+} ion, it is similar to $MnBi_2Te_4$, $MnBi_4Te_7$ and $MnBi_6Te_{10}$.

4.3.2 Transport properties

Figures 4.3 (j)-(l) present the temperature-dependent in-plane ($\rho_{xx}(H)$) and out-of-plane resistivity ($\rho_{zz}(H)$) of $MnBi_4Te_7$, $MnBi_6Te_{10}$ and $MnBi_8Te_{13}$. Above 20 K, all ρ show a typical metallic behavior and decrease with lower temperature. Upon further cooling, when approaching the transition temperature, because of the stronger scattering from enhanced spin fluctuations, all curves values increase with lower T. $\rho_{xx}(H)$ decreases below transition temperature in all three plots. In addition for $MnBi_8Te_{13}$, a sharp drop appears in $\rho_{zz}(H)$ too below 10.5 K, suggesting the loss of spin scattering along the c axis below the ordering temperature. The drop in $\rho_{zz}(H)$ below T_c is distinct from that in $MnBi_4Te_7$ and $MnBi_6Te_{10}$,

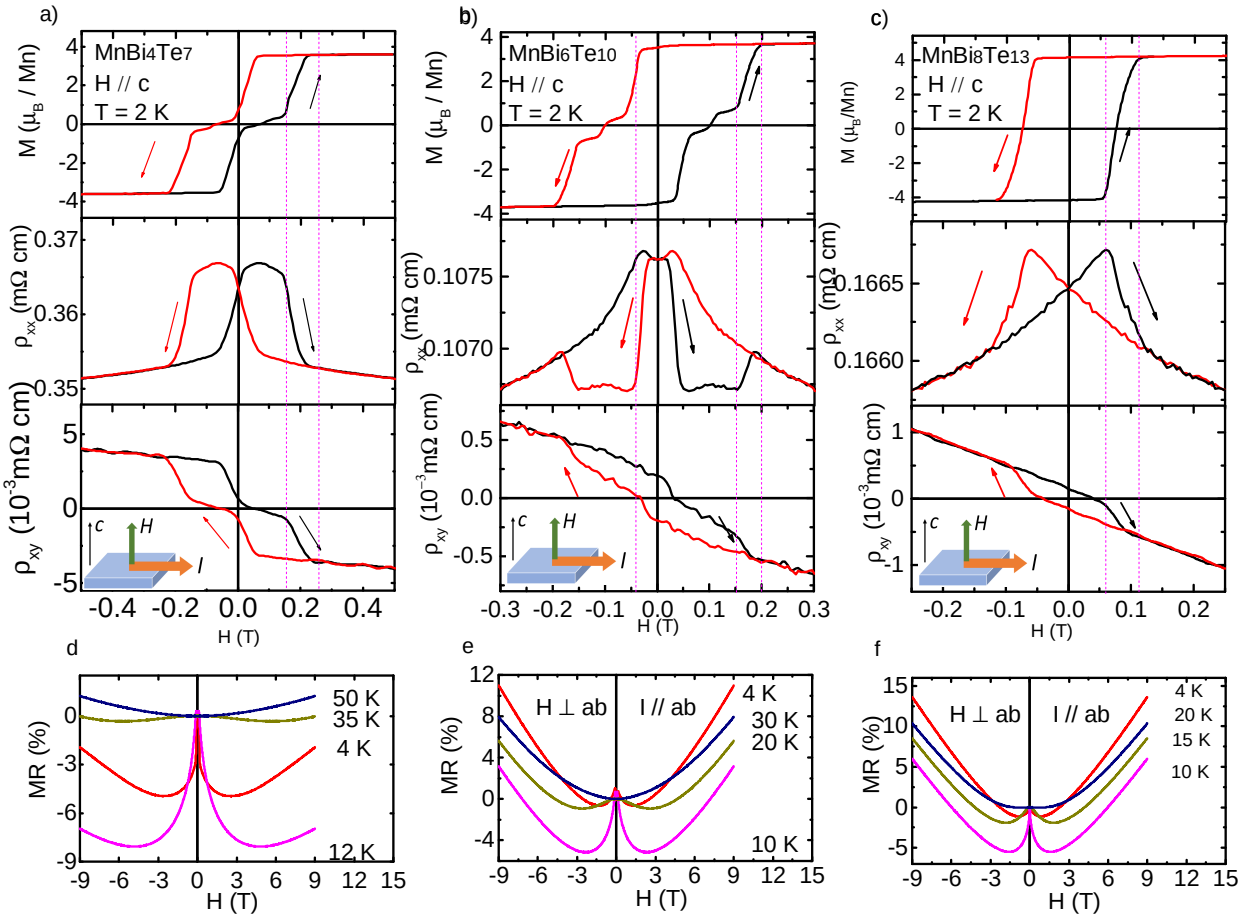

Figure 4.4: (a-c) The field-dependent magnetization M (top) with $H \| c$, transverse magnetoresistivity ρ_{xx} (middle) and Hall resistivity ρ_{xy} (bottom) at 2 K with $I \| ab$ and $H \| c$ for $MnBi_4Te_7$, $MnBi_6Te_{10}$ and $MnBi_8Te_{13}$, respectively. (d-f) Transverse magnetoresistivity ρ_{xx} with $I \| ab$ and $H \| c$ up to 9 T at various temperatures for $MnBi_4Te_7$, $MnBi_6Te_{10}$ and $MnBi_8Te_{13}$, respectively.

where the antiparallelly aligned Mn moments enhance resistivity via the spin-flip scattering. Therefore, the drop in $\rho_{zz}(H)$ again suggests FM ordering in $MnBi_8Te_{13}$ because the parallelly aligned Mn moments along the c axis eliminate such spin-flip scattering and thus reduce electrical resistivity.

Strong coupling between charge carriers and magnetism is observed in all $MnBi_4Te_7$, $MnBi_6Te_{10}$ and $MnBi_8Te_{13}$ through the magnetotransport measurements, as shown in Fig. 4.4 for $H\|c$ and Fig. 4.5 for $H\|ab$. $\rho_{xx}(H)$, and $\rho_{xy}(H)$ follow the same hysteresis as that in $M(H)$. Using $n = \frac{1}{e}\frac{dH}{d\rho_{xy}}$, our 50 K data correspond to an electron carrier density of 4.92×10^{20} cm^{-3} and 1.66×10^{20} cm^{-3} for $MnBi_6Te_{10}$ and $MnBi_8Te_{13}$ respectively, which are on the same order of the values for $MnBi_2Te_4$ and $MnBi_4Te_7$. We can again extract the anomalous Hall resistivity by $\rho_{xy} = R_0H + \rho_{xy}^A$ to compute the anomalous Hall angle AHA $= \rho_{xy}^A / \rho_{xx}$. The result is found to be 0.2% and 0.1% for $MnBi_6Te_{10}$ and $MnBi_8Te_{13}$. Both are much smaller than that for $MnBi_2Te_4$ and $MnBi_4Te_7$.

Figures 4.4 (d)-(f) show the $\rho_{xx}(H)$ curves up to 9 T at various temperatures for the three samples. The overall "W" shape previously seen in $MnBi_4Te_7$ in Chapter 3 is universal in $MnBi_6Te_{10}$ and $MnBi_8Te_{13}$ too, which was suggested to be a combination of nonmagnetic parabolic MR contribution and negative MR originating from FM fluctuations. The same W-shaped TMR at high field in $MnBi_4Te_7$ was seen up to 50 K. Here, the threshold temperature to observe the shape is only 30 K and 20 K for $MnBi_6Te_{10}$ and $MnBi_8Te_{13}$ respectively. This is in line with the overall weaker magnetism and fluctuations above T_c in $MnBi_6Te_{10}$ and $MnBi_8Te_{13}$.

For H$\|ab$, we can also identify the coupling of magnetic structure and transport in Figure 4.5. The effect is prominent in $\rho_{zz}(H)$. For all three MBT, the saturation field in ab plane is about 1.2 T as marked by the dashed line in the figures. The percentage drop at the saturation field is the highest in $MnBi_4Te_7$ at about 50%, but is down to to 12% in $MnBi_6Te_{10}$ due to fewer Mn and a weaker AFM state. The value is only 6% for $MnBi_8Te_{13}$, in which case the drop only comes from the suppression of opposite FM domains.

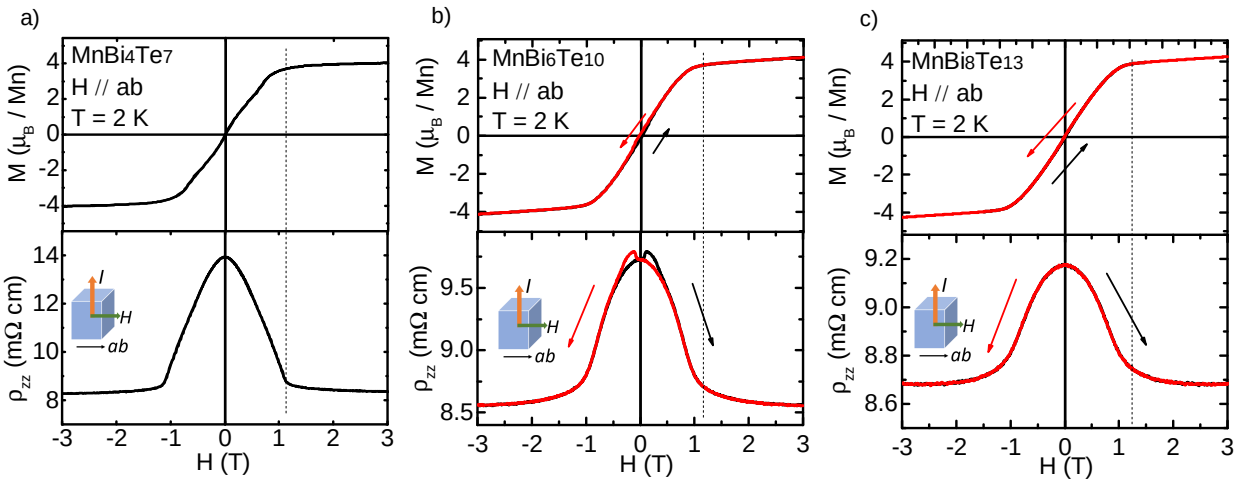

Figure 4.5: (a-c) The field-dependent magnetization M (top) with $H \| ab$, longitudinal magnetoresistivity ρ_{zz} (bottom) at 2 K for $MnBi_4Te_7$, $MnBi_6Te_{10}$ and $MnBi_8Te_{13}$ respectively.

4.4 Neutron scattering

Both $MnBi_6Te_{10}$ and $MnBi_8Te_{13}$ have the same crystal space group as $MnBi_2Te_4$. As a result, the AFM in $MnBi_6Te_{10}$ gives the same magnetic diffraction peaks as $MnBi_2Te_4$. Figure 4.6 shows the order parameter of a superlattice peak (0, 1, 1.5) below the ordering temperature. On the contrary, no additional Bragg peaks are observed in $MnBi_8Te_{13}$ because FM does not break any translation symmetry. Upon cooling below T_c about 10 K, the Bragg peak intensity of the nuclear peaks gain additional intensity, indicating the development of long-range magnetic ordering with the propagation vector $k = 0$. Starting from the nuclear space group R-3m with Mn atoms occupying the Wyckoff position (0, 0, 0) and $k = 0$, through symmetry analysis, we obtained the k-maximal magnetic subgroup as R-3m' whose symmetry only allows the presence of a FM arrangement with the Mn spins along the c axis.

The power law $I = A(\frac{T_M - T}{T_M})^{2\beta} + B$ was used to fit the intensity of magnetic reflection two reflections in $MnBi_6Te_{10}$ and $MnBi_8Te_{13}$ as a function of temperature. The fitting can be made satisfactorily with both 3D Heisenberg and 3D Ising models over the entire temperature range. With the 3D Heisenberg fitting and refinement at 4K, we determine the ordered Mn moment in the zero-temperature limit. The estimated magnetic moments are 4.4(5) μ_B and

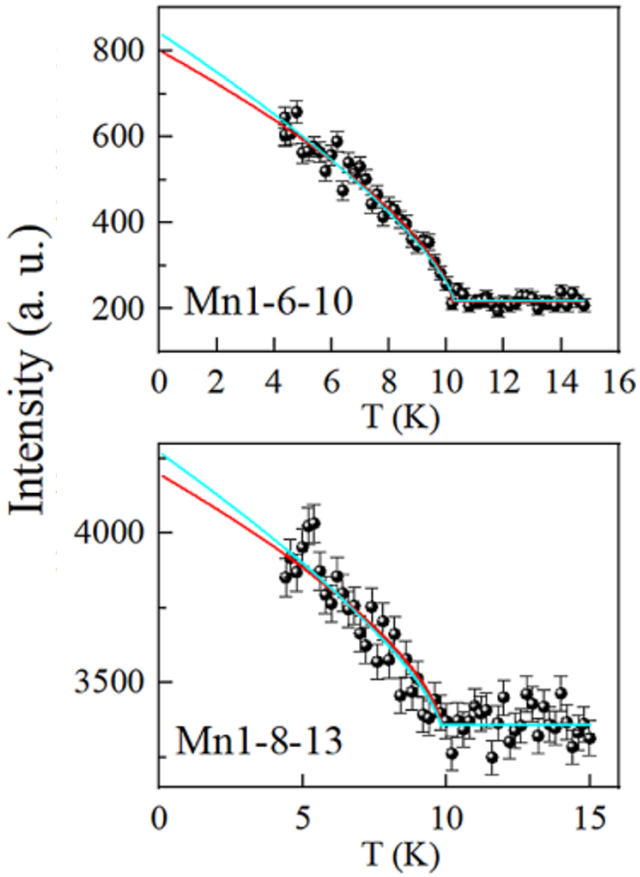

Figure 4.6: Magnetic order parameters upon warming at the magnetic reflections (0, 1, 1.5) and (1, 0, 1) for $MnBi_6Te_{10}$ and $MnBi_8Te_{13}$, respectively. The solid blue and red lines represent the fits using the 3D Heisenberg ($\beta = 0.367$) and 3D Ising ($\beta = 0.326$) models. The image is taken from [81].

4.9(2) μ_B for $MnBi_6Te_{10}$ and $MnBi_8Te_{13}$ respectively. Both values are close to the expected totally ordered moment of 5 μ_B for Mn^{2+} ions.

4.5 Ferromagnetic axion state revealed by DFT calculation

To investigate the band topology of $MnBi_8Te_{13}$, we calculated the electronic band structure in the FM configuration with the spin oriented along the c axis. Using the experimentally determined lattice parameters and atomic positions, our calculation shows only a continuous bulk energy gap. In contrast, using the experimental lattice parameters with relaxed atomic positions, our calculation indicates a 170 meV global energy band gap (Fig. 4.7(b)). By comparing our DFT calculation with the experimental ARPES data, the one with relaxed atomic positions describes the material well.

To highlight the spin-splitting in the presence of FM ordering, we present the $< S_z >$ resolved band-structure in Figure 4.7 (c). The band structure projected on the Bi p and Te p orbitals shows that the bands near the Fermi level mostly originate from the Bi p and Te p orbitals. As shown in Fig. 4.7(d), there are clear band inversions between the Bi p_z and Te p_z states. In fact, the Bi p_z orbitals reach deep into the valence bands, indicating multiple possible band inversions that originate from the different $[Bi_2Te_3]$ QL and $[MnBi_2Te_4]$ SL of $MnBi_8Te_{13}$.

The presence of clear band inversions around the Γ point hints towards a topological phase. To unravel the exact topology of this system, we first compute the Chern number in the $k_z = 0$ and $k_z = \pi$ planes. In both planes the Chern number is found to be zero. Next, we compute the parity-based higher-order Z_4 invariant, which is given by

$$Z_4 = \sum_{i=1}^{8} \sum_{n=1}^{n_{occ}} (1 + \eta_n(\Gamma_i))/2 \bmod 4 \tag{4.1}$$

Here, $\eta_n(\Gamma_i)$ is the parity of the nth band at the ith TRIM point Γ_i , and n_{occ} is the number of occupied bands. The Z_4 invariant is well defined for an inversion symmetric system, even in the absence of time reversal symmetry [46, 90, 91]. The odd values of Z_4 (1,

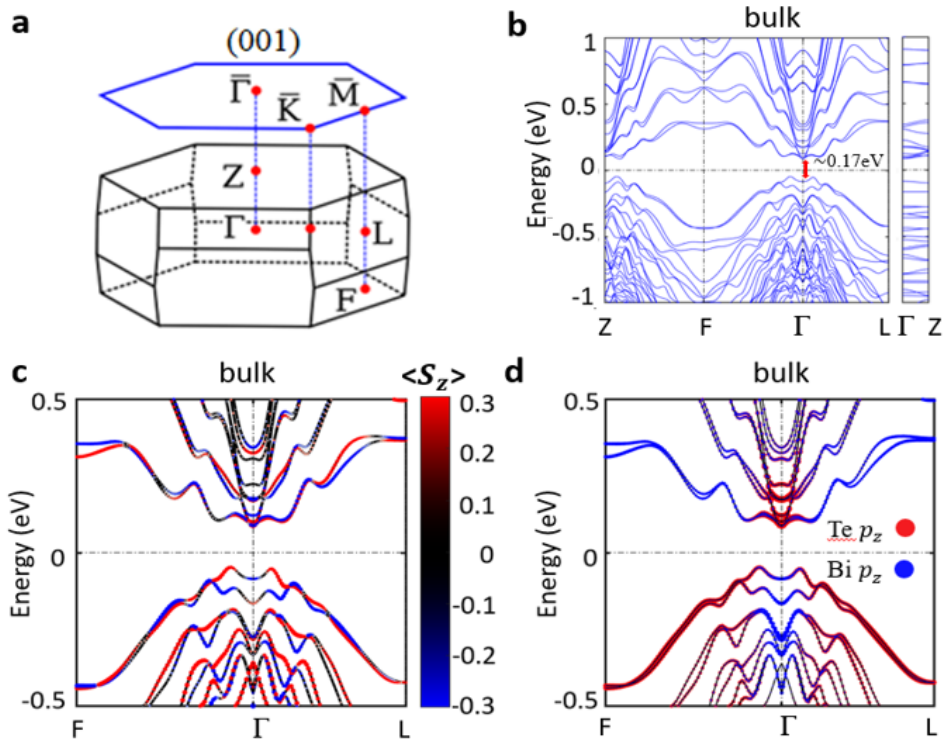

Figure 4.7: DFT band structure of bulk $MnBi_8Te_{13}$. (a) Bulk Brillouin zone (BZ) and the (001) surface BZ of $MnBi_8Te_{13}$ with the high symmetry points marked. (b) Bulk band structure of $MnBi_8Te_{13}$ in the out-of-plane FM configuration, with spin-orbit coupling and correlation parameter U included. (c) Spin-resolved band structure zoom in around the Γ point. (d) Orbital-resolved band structure zoom in around the Γ point. The red and blue dots indicate Te p_z and Bi p_z orbitals, respectively. There are clear band inversions between the Te p_z and Bi p_z states at the Γ point.

Table 4.2: The number of occupied bands of + and - parity eigenvalues at eight TRIM points of $MnBi_8Te_{13}$.

Γ_i	(0,0,0)	(π,0,0)	(0,π,0)	(0,0,π)	(π,π,0)	(0,π,π)	(π,0,π)	(π,π,π)
n^+_{occ}	65	67	67	67	63	63	63	67
n^-_{occ}	60	58	58	58	62	62	62	58

3) indicate a Weyl semimetal phase, while Z_4 =2 implies an insulator phase with a quantized topological magnetoelectric effect (axion coupling $\theta = \pi$) [36]. A detailed list of the number of occupied bands with even (n^+_{occ}) and odd (n^-_{occ}) parity eigenvalues at the eight TRIM points are shown in Table 4.2. Based on this, the computed Z_4 invariant is found to be 2, which demonstrates that $MnBi_8Te_{13}$ is an intrinsic FM axion insulator.

It is noted that, in calculations with or without atomic relaxation, the characteristics of band inversion and the topology of whole system remain the same, i.e., an FM axion state. In addition, we have investigated the evolution of the band structures by changing lattice constants a, b (in-plane) and c (out-of-plane) simultaneously. Within the range from -3% to +3% in $MnBi_8Te_{13}$, we did not find any crossing point or the additional band inversion feature. Our calculation reveals that the axion phase in $MnBi_8Te_{13}$ is quite stable.

4.6 Surface state revealed by ARPES and DFT

To investigate if surface states appear in $MnBi_8Te_{13}$, our collaborators in Dan Dessau's group at CU-Boulder performed small-spot (20 μm $\times$ 50 μm) ARPES scanned across the surfaces of $MnBi_8Te_{13}$. According to the crystal structure of $MnBi_8Te_{13}$, four different terminations are expected during the cleave, as visualized in the cartoon pictures on the top of Figure 4.8. Our ARPES data and DFT calculations indeed reveal distinguishing surface states for the four different terminations of $MnBi_8Te_{13}$, which are summarized in Figure 4.8.

Figures 4.8(a-d) show the isoenergy surfaces at the Fermi level which uniquely fingerprints each of the four possible terminations of $MnBi_8Te_{13}$. The measurements were done using 26

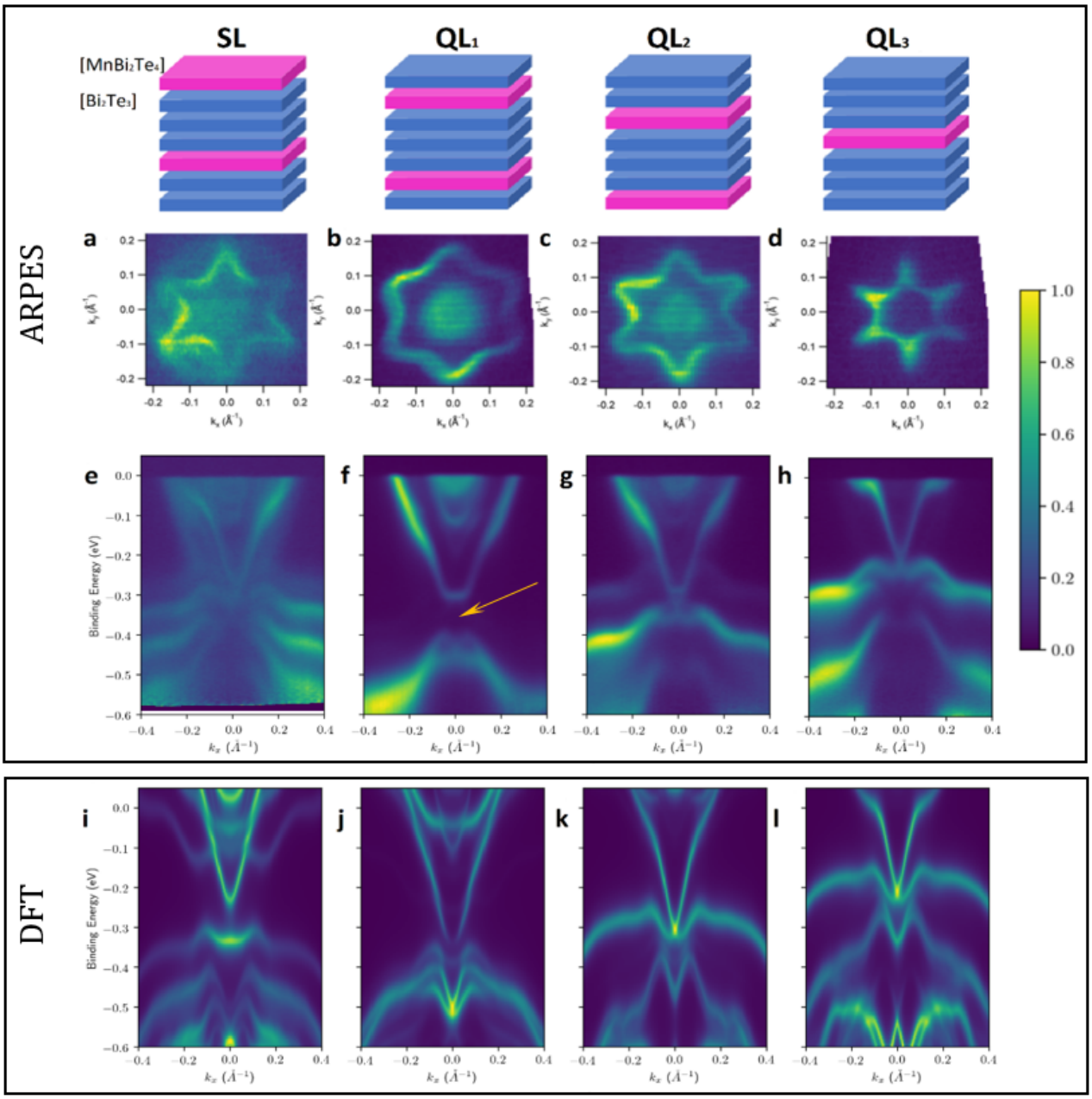

Figure 4.8: The comparison of ARPES data and DFT calculation on $MnBi_8Te_{13}$ under surface termination of SL, QL1, QL2, and QL3. (a-d) ARPES isoenergy surfaces at the Fermi level . (e-h) Experimental ARPES E-k spectrum cut along the $M \longleftarrow \Gamma \longrightarrow M$ high symmetry direction for various terminations. (i-l) Calculated DFT $E-k$ spectrum cut along the $M \longleftarrow \Gamma \longrightarrow M$ high symmetry direction for various terminations.

eV, 20 $\mu m \times$ 50 μm spot-sized linear horizontal light at 12 K. We identify a unique circular Fermi surface for the SL termination which has been observed in other $MnBi_{2n}Te_{3n+1}$ (n = 1, 2, 3) [50,89,92,93]. We find that the QLn terminations show a dominant six-fold symmetric Fermi surface with decreasing cross-sectional area from QL1 to QL3. Our assignment of the isoenergy surfaces to the respective terminations for $MnBi_8Te_{13}$ is consistent with previous measurements on the simpler $MnBi_2Te_4$, $MnBi_4Te_7$, and $MnBi_6Te_{10}$ compounds. Figures 4.8(e-h) present the experimental ARPES $E-k$ maps along the M-Γ-M high symmetry direction. Different types of surface states are observed for each of the four terminations. For the SL termination, a gapless or nearly gapless surface state appears (Fig. 4.8e), consistent with the gapless surface state observed on the SL termination in previous ARPES measurements of $MnBi_2Te_4$, $MnBi_4Te_7$, and $MnBi_6Te_{10}$ [50, 66, 89, 92, 93]. The QL3 termination, which is unique to $MnBi_8Te_{13}$, shows mass renormalization near the Fermi level (Fig. 4.8h). Furthermore, a large surface gap of about 105 meV centering around the charge neutrality point of -0.35 eV is clearly revealed in the QL1 termination and is highlighted by the arrow (Fig. 4.8f). It is noted, we find that the spectra taken below and above the transition temperature are very similar in terms of the size of the gap, except for thermal broadening of the electrons. This has been observed in various magnetic topological insulators, including $MnBi_2Te_4$, $MnBi_4Te_7$, $MnBi_6Te_{10}$ and the origin of it is under debate [66,94].

In order to confirm the topological nature of $MnBi_8Te_{13}$, we calculated the surface spectral weight throughout the (001) surface BZ using the semi-infinite Green's function approach for SL, QL1, QL2, and QL3 terminations correspondingly. The result is shown in Fig. 4.8(i-l). Each state is plotted with a color corresponding to the integrated charge density of the state within the topmost QL or SL. In addition, we shift the Fermi level to match the experimentally observed Fermi level.

Excellent agreement between the experimental ARPES data and DFT calculation is achieved for the QLn terminations as shown in Fig. 4.8. Our calculation suggests that the sizable surface band gap presented in the QL1 termination around -0.35 eV is a hybridization gap induced from the hybridization effect between the topmost QL and the nearest-

neighboring SL. Although the calculated band gap value is smaller than that from ARPES, it is a well-known problem in that GGA generally underestimates the band gap in semiconductors and insulators [95, 96].The hybridization gap seems universal in $MnBi_{2n}Te_{3n+1}$, which has been suggested for $MnBi_6Te_{10}$ [97] and $MnBi_4Te_7$ [98]. However, until now, it is unclear if the hybridization gap exists and supports QAH in the 2D limit. To settle down this issue, we have performed DFT calculation on a 7-layered finite-size slab model with the arrangement of vacuum-[QL-SL-QL-QL-QL-SL-QL]-vacuum, i.e. a structure that has the QL1 termination on both surfaces. The main features of the slab result shown in Fig. 4.9(a) are consistent with our semi-infinite Green's function approach. We then calculate the Chern number of this slab model based on the Wilson loop method [99]. Our result shows a nontrivial Chern number ($C = 1$) in this hybridization gap (Fig. 4.9(b), demonstrating that $MnBi_8Te_{13}$ is indeed a QAH insulator in its 2D limit if the Fermi level is gated to the middle of the large hybridization gap.

As a consequence of strong exchange fields from the Mn magnetic layer in the SL termination, our calculation on the SL termination results in a parabolic large gapped surface band dispersion in the bulk energy gap (Fig. 4.8i). This is in sharp contrast with the gapless Dirac surface state revealed by the ARPES (Fig. 4.8e). For the SL termination, the deviation between ARPES and DFT calculation as well as the gapless Dirac surface state are universal in the $MnBi_{2n}Te_{3n+1}$ family (n = 1, 2, 3) [66,89,92,93]. The unexpected gapless surface state is argued to be caused by the surface spin reconstruction when the magnetic [$MnBi_2Te_4$] layer is at the vacuum-sample interface [66, 92, 93]. Further experiments in identifying the spin reconstruction on the SL termination are urged to settle down this issue.

4.7 Summary and outlooks

We have presented the realization of the first intrinsic ferromagnetic topological material, $MnBi_8Te_{13}$. Our work has several implications. First, our theoretical calculations show that $MnBi_8Te_{13}$ is a ferromagnetic axion insulator. Such a topological axion state suggests a quantized magnetoelectric coupling and an emergent axion electrodynamics. Therefore, the

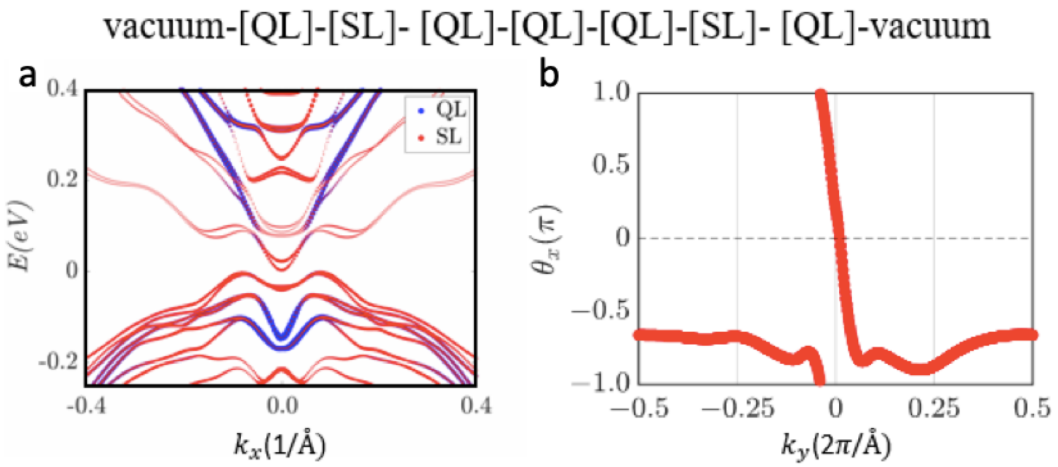

Figure 4.9: DFT band structure of $MnBi_8Te_{13}$ in a seven-layered finite-sized slab model corresponding to the QL1 surface arrangement, i.e., with vacuum-[QL-SL-QL-QL-QL-SL-QL]-vacuum. (a) Band structure of this slab model. The sizes of the blue and red dots represent the fraction of electronic charge residing in the topmost QL and the nearest-neighboring SL, respectively. (b) Evolution of the sum of Wannier charge centers (WCCs) along ky in the $k_z = 0$ plane. The trajectory of WCC is an open curve traversing the whole BZ once, indicating the Chern number $C = 1$ in the $k_z = 0$ plane.

optical responses of $MnBi_8Te_{13}$, especially in the terahertz regime, may be of great interest. Second, the intrinsic ferromagnetism paves the way for the realization of QAH state at zero magnetic field. Third, when it is exfoliated into the 2D version, the superlattice nature and the stacking of vdW $MnBi_8Te_{13}$ makes it possible to fabricate richer combinations of natural heterostructures than those from AFM $MnBi_{2n}Te_{3n+1}$ ($n = 1, 2, 3$). Various emergent properties such as QAH state and QSH state are proposed for such heterostructures. Furthermore, the observation of long-range magnetic order is striking considering the extremely large separation of 44.1 Å between the adjacent $[MnBi_2Te_4]$ SLs; further investigations will shed light on the mechanism of the long-range magnetic ordering in $MnBi_8Te_{13}$ and will advance our understanding on the magnetism in vdW materials. Finally, our work here in general establishes natural heterostructure as a powerful way to rationally design and control magnetism and other broken symmetry states in layered vdW materials.

We have shown the structural and magnetic and topological properties of the magnetic topological material series $MnBi_{2n}Te_{3n+1}$. We were able to implement our structural design of inserting the nonmagnetic QL layer between the magnetic $[MnBi_2Te_4]$ SL layer. Such rational design and great tunability of the structure of SL and QL layers allow $MnBi_{2n}Te_{3n+1}$ to have various magnetic ground state. By such, we obtained weakly interlayer coupled A-type AFM $MnBi_4Te_7$ and $MnBi_6Te_{10}$, and FM $MnBi_8Te_{13}$. In terms of topology, we demonstrated $MnBi_4Te_7$ is an AFM TI; similar is expected and reported for $MnBi_6Te_{10}$. Finally, we revealed that $MnBi_8Te_{13}$ is an intrinsic FM axion insulator, and similar is expected for $n > 4$ sample. As the foundation of engineering 2D heterostructures, such a highly tunable topological vdW material systems could open up unprecedented opportunities in discovering novel fundamental physics as well as making new quantum devices.

Now, in order to observe these exotic states predicted by theory based on $MnBi_{2n}Te_{3n+1}$, such as QAHE, it is essential to have the Fermi level to near the Dirac point or the bulk and surface gap to observe the edge or surface states. In reality, this is not the case in the bulk crystals due to the presence of various defects. Other than gate-tuning and other post treatment that can tune the Fermi level in the thin-film sample to a certain extent, it

remains a challenge to grow an intrinsically low-carrier bulk sample. This motivates further studies on the defects and growth optimization. To that end, ongoing studies are carried out in the field. We will discuss our studies on the role of Sb doping in Chapter 5 and how the growth optimization can help in Chapter 7, respectively.

CHAPTER 5

Tuning magnetism and band topology through antisite defects in Sb-doped $MnBi_4Te_7$

This chapter is adapted from [100]. This work was done in collaboration with Tay-Rong Chang's group at National Cheng Kung University on first-principles band structure calculations, Igor I. Mazin at George Mason University on the phenomenological magnetic model, and Huibo Cao's group at Oak Ridge National Lab on neutron diffraction measurements.

5.1 Introduction

In the previous chapters, we have seen $MnBi_2Te_4$ is a Z_2 AFM TI with A-type magnetic structure where spins antiferromagnetically couple strongly along the c axis and ferromagnetically align in the ab plane. Then we could effectively reduce the interlayer coupling by increasing n and thus the interlayer Mn-Mn distance in $MnBi_{2n}Te_{3n+1}$ which evolves from a Z_2 AFM TI with saturation fields of 7.7 T in $MnBi_2Te_4$ ($n = 1$) [53, 62, 75], 0.22 T in $MnBi_4Te_7$ ($n = 2$) [50, 101] and 0.18 T in $MnBi_6Te_{10}$ ($n = 3$) [89, 92, 102, 103], to a FM axion TI in $MnBi_8Te_{13}$ ($n \geq 4$) [80, 104], leading to a highly tunable intrinsic natural heterostructural topological insulator series which are excellent candidates to realize QAHE and QME.

However, n is a discrete tuning parameter which cannot lead to continuous change of interlayer Mn-Mn coupling and thus provides less insight in the rich competition between various ground states. Meanwhile, chemical doping serves as a continuous tuning parameter. Compared to the case of trivial magnetic metal, in small-gap MTI $MnBi_{2n}Te_{3n+1}$, chemical

doping may not only tune their magnetism but also their band topology and carrier density. Profound effects of Sb doping has been observed in $Mn(Bi_{1-x}Sb_x)_2Te_4$ single crystals. Besides an electron-carrier to hole-carrier change [65, 105], the series evolve from AFM $MnBi_2Te_4$ to ferrimagnetic $MnSb_2Te_4$ [105–107]. This evolution suggests complicated doping mechanism and defect chemistry in this series. Although single crystal neutron scattering study on $MnBi_2Te_4$ indicates Bi atoms substitute on Mn sites with no discernable Mn atoms on Bi sites [72], similar measurements on $MnSb_2Te_4$ reveal substantial antisite disorder between Mn and Sb 6*c* sites [106, 107], resulting in two Mn sublattices. The delicate energy-scale competition was demonstrated in a recent study on $MnSb_2Te_4$ [107]. While these two Mn sublattices always couple antiferromagnetically, in samples with slightly lower antisite disorder, each Mn sublattice orders antiferromagnetically; in samples with slightly higher antisite disorder, each Mn sublattice orders ferromagnetically.

Compared to $MnBi_2Te_4$, the members with $n \geq 2$ has extra spacer [Bi_2Te_3] layers and thus much larger Mn-Mn interlayer distances. Therefore, the AFM and FM ground states can be closer in energy, so these high n members are more sensitive to perturbations. Here we report a systematic study of the effect of Sb doping on $MnBi_4Te_7$ and reveal the important role of the Mn/Sb antisite disorder caused by Sb-doping in governing the magnetism.

5.2 Growth and Characterization

Single crystals were grown using the flux method [50, 62]. Elemental forms of Mn, Bi, Sb and Te are mixed at the ratio of MnTe:$(Bi_{1-x}Sb_x)_2Te_3$=15:85 in an alumina crucible sealed in a quartz ampule under 1/3 atm of argon. The quartz ampule is quickly heated to 900°C and stays for 5 h, followed by a quick cooling to 10° above the targeted spin-out temperature. Then it is slowly cooled to the spin-out temperature over three days and stays for another three days before the spin out. Since the growth window is narrower than the undoped growth and different for each doping level, similar trial-and-error strategy (See Chapter 4)) was employed to determine the spin-out temperature for the 147 phase for the doping level.

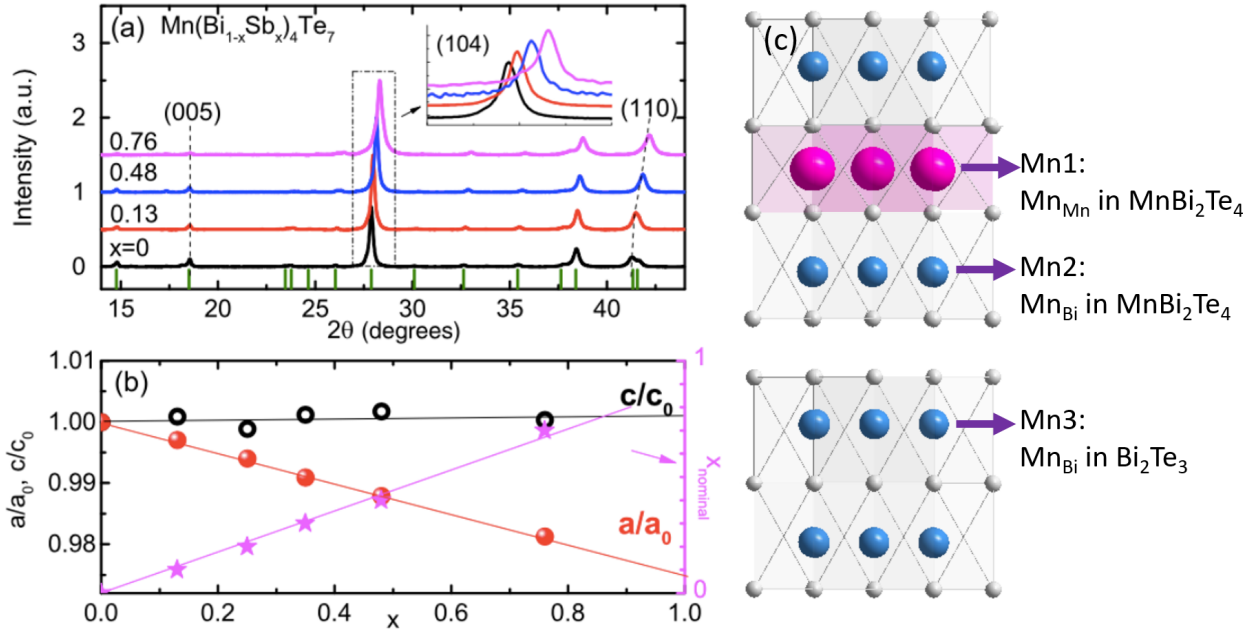

Figure 5.1: (a) PXRD of $Mn(Bi_{1-x}Sb_x)_4Te_7$ for the pieces for which the data in the paper were collected. The peak positions of the 147 phase are marked. Inset: the zoom-in plot of the (104) PXRD peaks. (b) The doping-dependent relative lattice parameters a/a_0, c/c_0 and nominal concentration xnominal used in the growth. a_0 and c_0 are the lattice parameters for $MnBi_4Te_7$. (c) Crystal structure of $Mn(Bi_{1-x}Sb_x)_4Te_7$ viewed from [1 -1 0] direction, marked with potential Mn sites labelled as Mn1, Mn2 and Mn3.

Both the PXRD and chemical analysis via WDS indicate that Sb was successfully doped into $MnBi_4Te_7$ and the results are summarized in Fig. 5.1 and Table 5.1. Figure 5.1(a) shows the PXRD patterns for various doping levels. All peaks can be indexed by the 147 phase. If there is 023 phase impurity, a clear hump will appear at the left shoulder of the (104) peak. As shown in the inset of Fig. 5.1(a), the 023 phase is indiscernible or less than 5% if there is. With Sb doping, the (005) peak roughly stays at the same angle while the (104) peak shifts moderately and the (110) peak shifts much to higher angles, indicating distinct in-plane and out-of-plane lattice response to the Sb doping. Figure 5.1(b) shows the doping-dependent lattice evolution. The lattice parameter a decreases linearly by 2% up to our highest doping level $x = 0.76$ while the lattice parameter c remains almost the same. This lattice evolution is similar to that in $Mn(Bi_{1-x}Sb_x)_2Te_4$ [105].

WDS reveals the real doping level of Sb as well as a universal deficiency of Mn in all compounds as seen in Table 5.1. The total Mn concentration is near 0.8 for all but slowly increases with x. This is because when Sb substitutes Bi, it also introduces the preferable Mn_{Sb} antisites [105–108] (high-spin Mn^{2+} ionic radius, 99 pm, is closer to that of Sb^{3+}, 90 pm, than to Bi^{3+}, 117 pm [109]). Therefore, upon Sb doping, more and more Mn can enter into the Bi/Sb sites. In contrast to the $Mn(Bi_{1-x}Sb_x)_2Te_4$ series where two Mn sublattices exist due to the $Mn_{(Bi,Sb)}$ antisite formation, Sb doping in $MnBi_4Te_7$ gives rise to a more complex antisite chemistry, where three Mn sublattices appear. We denote the Mn atoms occupying the Mn site as Mn1 sublattice, the Mn atoms on the Bi site within SLs as Mn2 sublattice, and the Mn atoms on the Bi site in QLs as Mn3 sublattice in the structure plot in Figure 5.1. In this study, we will show while the Mn2 and Mn3 antisites are much less concentrated than Mn1, they do make a big impact on the overall magnetism and band topology.

5.3 Evolution of magnetic properties with chemical doping

The evolution of magnetic structure in the series can be well traced in the temperature-dependent susceptibility with $H\|c$ ($\chi^c(T)$), the temperature-dependent resistivity with $I\|ab$

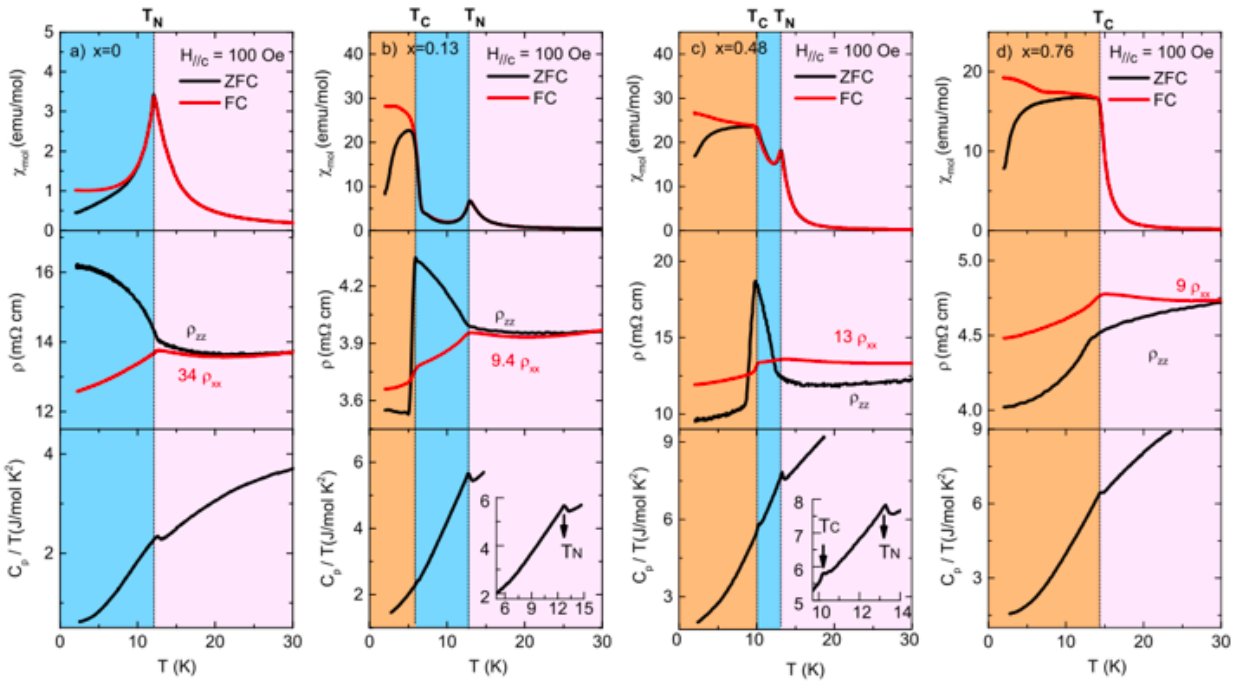

Figure 5.2: The evolution of magnetism with temperature in $Mn(Bi_{1-x}Sb_x)_4Te_7$ from $x = 0$ to x =0.76: (a)-(d) Top panel: $\chi^c(T)$, the temperature-dependent ZFC and FC magnetic susceptibility under 0.01 T with $H\|c$. Middle panel: $\rho_{xx}(T)$ and $\rho_{zz}(T)$, the temperature-dependent electrical resistivity with the current along the ab plane and the c axis. Bottom panel: $C_p(T)$, the temperature-dependent specific heat and the zoom-in of $C_p(T)$ near transitions (inset).

($\rho_{xx}(T)$) and $I \| c$ ($\rho_{zz}(T)$), as well as the temperature-dependent specific heat ($C_p(T)$) data in Figure 5.2. For $x = 0$, at $T_N = 12.7$ K, the sharp cusp in $\chi^c(T)$ and the kink in $C_p(T)$ signal the PM to AFM phase transition. Furthermore, below T_N, the sudden increase of $\rho_{zz}(T)$ and drop of $\rho_{xx}(T)$ are indicative of the gain (loss) of the spin-disorder scattering along the c axis (ab plane). This suggests spins parallel in the ab plane but anti-parallel along the c axis, consistent with the A-type AFM structure revealed by neutron data [72, 103].

For $x = 0.13$, in addition to a sharp cusp at $T_N = 12.8$ K in $\chi^c(T)$ suggesting AFM transition like the parent compound, a second transition occurs at $T_C = 6.0$ K marked by a sudden increase and a large bifurcation in the ZFC and FC data of $\chi^c(T)$. From T_N to T_C, $\rho_{zz}(T)$ increases sharply and $\rho_{xx}(T)$ drops, analogous to that of the $x = 0$ sample, while below T_C, $\rho_{zz}(T)$ decreases sharply due to the loss of spin scattering like that in the FM $MnBi_8Te_{13}$ [80]. Meanwhile, since Mn1 and Mn2 sublattices in the SL plane are strongly AFM coupled to each other through superexchange interaction [107], Mn2 sublattice most likely orders simultaneously and antiferromagnetically with Mn1 at T_N. Therefore, we argue that from T_N to T_C, Mn1 and Mn2 sublattices each adopts A-type AFM, while they also AFM coupled to each other. Below T_C, while Mn1 and Mn2 sublattices are still AFM coupled to each other, they are FM within themselves. We denote these two magnetic structure as Ferri^{AFM} and Ferri^{FM}, as depicted in Fig. 5.3(a).

For $x = 0.48$, the shapes of the $\chi^c(T)$, $\rho_{zz}(T)$ and $\rho_{xx}(T)$ curves are similar to those of the $x = 0.13$ compound, manifesting a Ferri^{AFM} state between $T_N = 13.3$ K and $T_C = 10.2$ K and a Ferri^{FM} state below T_C. However, in sharp contrast to the $x = 0.13$ sample where specific heat anomaly only appears at T_N, an additional small specific heat anomaly emerges at T_C for $x = 0.48$, indicating an entropy release which is not directly originated from the AFM-FM transition of the Mn1 and Mn2 sublattice at T_C. Since it is natural to believe that Mn3 concentration is higher in this doping level than that in the $x = 0.13$ sample. This additional specific heat release is very likely to be related to the increasing amount and the magnetic state of the Mn3 sublattice.

For $x \geq 0.58$ like Fig. 5.2(d), only one phase transition is observed. As a representative,

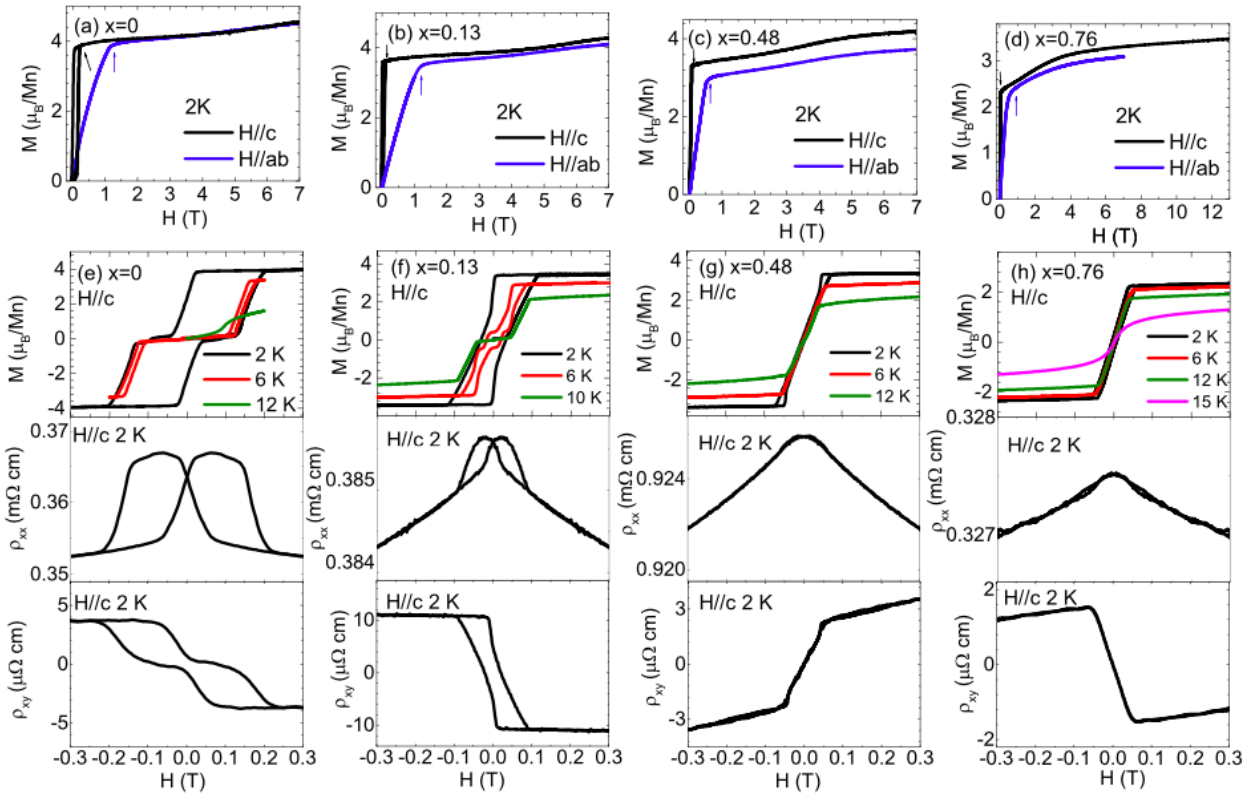

Figure 5.3: The evolution of magnetism with field in $Mn(Bi_{1-x}Sb_x)_4Te_7$ from $x = 0$ to x =0.76: (a-d) The isothermal magnetization $M(H)$ at 2 K with $H\|c$ and $H\|ab$. The unit is chosen as μ_B/Mn where the Mn concentrations via WDS data are used. (e-h): The hysteresis of $M(H)$ (top), $\rho_{xx}(H)$ (middle) and $\rho_{xy}(H)$ (bottom) with $H\|c$ at 2 K (unless noted otherwise). At 2 K, the hysteresis of the $M(H)$ curve goes from AFM type ($x = 0$) to FM type ($x = 0.76$).

the data for $x = 0.76$ is shown in Figure 5.2 (d). The $\chi^c(T)$, $\rho_{zz}(T)$ and $\rho_{xx}(T)$ are reminiscent of those of the $x = 0.13$ and 0.48 compounds in the Ferri^{FM} state, suggesting Mn1 and Mn2 sublattices order simultaneously at 14.5 K into the Ferri^{FM} state.

Figures 5.3(a)-(d) present the isothermal magnetization data at 2 K under $H\|ab$ and $H\|c$. The data suggest an easy-c axis for the whole series. It also allows us to estimate the uniaxial anisotropy SD via $SD = (1/2)g\mu_B H_{ab} - g\mu_B H_c$ [105], where $g = 2$ and H_{ab} and H_c are the field marked by the arrows in the figures. The obtained SD is summarized in Table 5.1. As we can see that SD decreases with high Sb doping, similar to the case of Sb-doped

$MnBi_2Te_4$ [105]. Figures 5.3(e)-(h) show the magnetic hysteresis loop, the field-dependent electrical resistivity ($\rho_{xx}(H)$) and Hall resistivity ($\rho_{xy}(H)$) with $H\|c$. A spin flip transition with hysteresis was observed at 0.15 in the $x = 0$ sample. The envelopes of the $M(H)$ curves in the Ferri^{FM} ground state are nontrivial. Instead of a standard FM hysteresis loop, a bow-tie-shaped hysteresis loop can be clearly observed at 2 K. A recent magneto-optic study suggests this bow-tie-shaped hysteresis may be related to the formation of low-field fine-structured isotropic domains and high-field less isotropic sea-urchin-shaped domains [110]. We also note that the multi-step feature of the $M(H)$ curve at 6 K for the $x = 0.13$ compound is reminiscent of that of the $MnBi_6Te_{10}$ compound [110]. This may suggest the existence of small amount of FM domains in the AFM state of $MnBi_6Te_{10}$. Therefore, close energy scales of FM and AFM is universal in the $n \geq 2$ $MnBi_{2n}Te_{3n+1}$ members. This explains the controversies on the magnetic ground states of $MnBi_4Te_7$ obtained from different growth methods, while the first-principle calculations suggest an AFM ground state [50, 101]. This is all because slight site defects are enough to tune the exchange energy to surrender one and boost the other.

Magnetism and charge carriers are strongly coupled in the series. At $x = 0$, a sharp drop in $\rho_{xx}(H)$ can be observed at the spin-flip field around 0.15 T due to the loss of spin-disorder scattering. On the other hand, $\rho_{xx}(H)$ shows subtle decrease for the $x = 0.13$, 0.48 and 0.76 samples, consistent with their Ferri^{FM} ground state. In the Hall resistivity panels, anomalous Hall effect arising from the internal magnetization can be seen in all concentrations. Furthermore, a clear sign change of ordinary Hall resistivity appears at x =0.48. We then determine the carrier density using $n = \frac{1}{R_H e}$ where the Hall coefficient R_H is the slope of $\rho_{xy}(H)$ at 20 K in Figure 5.4. After interpolating the carrier density with doping level, an estimated charge neutrality point is found near $x = 0.36$, as shown in Figure 5.4(b).

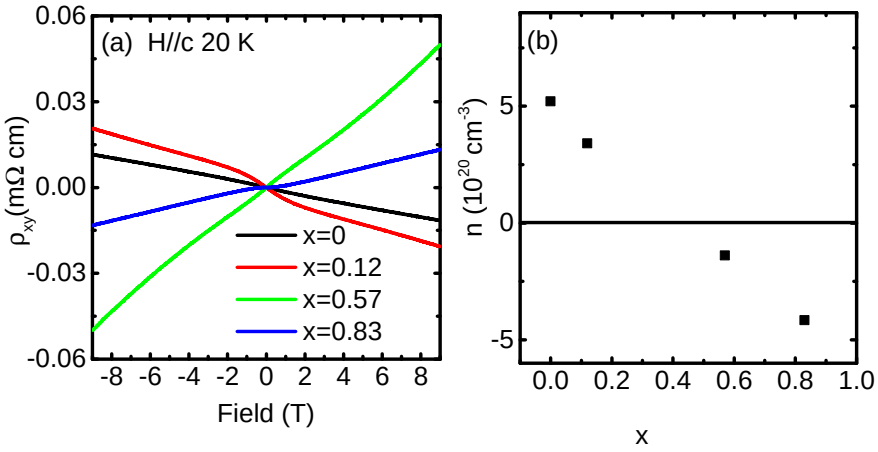

Figure 5.4: Hall resistivity and carrier concentration. (a) Hall resistivity measured at 20 K with $I \| ab$. (b) Doping-dependent carrier density.

5.4 Estimating Mn_{Bi} antisites using magnetic and neutron scattering data

Based on our aforementioned discussions about Fig. 5.1, we have hypothesized the magnetic structures of the Mn1 and Mn2 sublattices. However, a few important questions remain unclear for this doping series. What are the concentrations of the Mn1, Mn2 and Mn3 sublattices? Does the Mn3 sublattice order? If yes, what is its ordering state? If not, is it glassy or fluctuating? Single-crystal neutron scattering measurements were performed on the $x = 0.76$ sample. Together with the high-field $M(H)$ data which provides an alternative way to estimate the concentrations of the three Mn sublattices, they shed light on these questions.

The preliminary refinement of the single-crystal neutron data with all fitting parameters free indeed indicates a Ferri^{FM} state of the Mn1 and Mn2 sublattice at 5 K, consistent with Fig. 5.5(a). The refinement further suggests the moment contributed from Mn3 atoms is $0.13(10)\mu_B$/f.u. This small moment either implies negligible Mn3 concentration, or Mn3 sublattice is glassy/fluctuating. To differentiate these two scenarios, let us focus on the high-field $M(H)$ data with $H \| c$ shown in Figs. 5.3(a)-(d). Above a sharp increase caused by the Mn1+Mn2 complex below 0.2 T, a universal, subtle, but clear medium-field magnetization

Table 5.1: Chemical composition of $Mn(Bi_{1-x}Sb_x)_4Te_7$, the estimation of defects concentration with m, n, and l representing the Mn occupancy on Mn2 sites, Mn3 sites, and Mn1 sites respectively. The magneocrystalline anisotropy parameter is estimated from the saturation field of the dominant Mn1 sublattice $(H_{sat}^{ab})_{\mathrm{Mn1}}$ (see text).

	x_{nominal}	Mn:Bi:Sb:Te	Sb/(Bi+Sb)	m	n	l	SD (meV)
WDS	0	0.78(3):4.27(7):0:7	0	0.015(5)	0.03(1)	0.73(3)	0.052
	0.1	0.79(2):3.70(3):0.57(1):7	0.13(1)	0.020(5)	0.04(1)	0.70(3)	0.053
	0.4	0.81(4):2.19(5):2.04(1):7	0.48(1)	0.025(5)	0.055(10)	0.65(3)	0.026
	0.7	0.82(1):1.00(3):3.08(2):7	0.76(1)	0.060(5)	0.07(1)	0.56(3)	0.015
neutron	0.7	0.88(3): 1.15(6):2.96(6):7	0.72(2)	0.06(1)	0.07	0.62(1)	0.015

increase appears around 1-5 T in the whole doping series. Because the coupling between Mn1 and Mn3 is weaker than that between Mn1 and Mn2, Mn3 should polarize at a lower field than Mn2. Therefore, this medium-field magnetization increase should arise from the polarization of the Mn3 sublattice since the Mn2 sublattice will flip at a much higher fields. Indeed, for $x = 0.76$, $M(H)$ is only 3.4 μ_B/Mn at 13 T. Despite reaching a plateau, it is still much smaller than 5 μ_B/Mn, the theoretical value for Mn^{2+}. This strongly indicates the flipping of Mn2 will happen at a field higher than 13 T. As a reference, in $MnBi_2Te_4$, the flipping process of the Mn2 sublattice starts at 20 T and ends at 60 T [111].

Such a field-dependent magnetic structure evolution is depicted in Fig. 5.5(b), which allows us to separate the contribution of magnetization from each Mn sublattices in the $M(H)$ curve with $H\|c$ (Figs. 5.3(a)-(d)). Right before the sizable polarization of Mn3 sublattice, the sample is in the state I depicted in Fig. 5.5(b) and we denote the moment to be α. Then with increasing field, more and more Mn3 atoms are polarized into the state II as pictured in Fig. 5.5 (b), leading to a plateau in $M(H)$ with the moment of β. With even higher fields, Mn2 will be polarized and finally all three Mn sublattices stay in state III as drawn in Fig. 5.5 (b), resulting in a moment of γ. Therefore, the difference in α and β can tell us the total moment contributed by Mn3 atoms under field. For $x = 0.76$, this value is $\sim 0.8(1)$

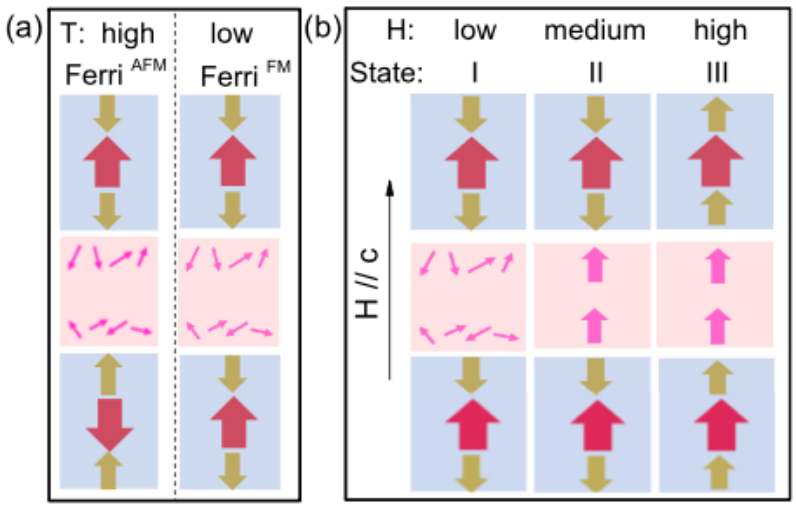

Figure 5.5: (a) The depiction of the Ferri^{AFM} and Ferri^{FM} states. Red, olive and pink arrows represent the Mn1, Mn2 and Mn3 spins. (b) Ferri^{FM} state with $H\|c$ at low, medium and high field: the depiction of the process of the polarization of Mn3 and the spin-flipping of Mn2.

μ_B/Mn, suggesting the Mn3 spins contribute significantly to the ordered moment under fields and thus Mn3 concentration is not negligible. Together with the neutron scattering data which reveal all Mn3 atoms only contribute $0.13(10)\mu_B$/f.u. at zero field, we conclude that Mn3 atoms are in the glassy/fluctuating state at 5 K. Furthermore, considering that Mn3 atoms need above 1 T to be polarized while the recent ac susceptibility measurements of the $x = 0.76$ sample only show relaxation behavior below 500 Oe [110], it is likely that at 5 K the Mn3 atoms are not in the glassy state, but rather fluctuating in the paramagnetic state. Future site-sensitive nuclear magnetic resonance measurements can help clarify the magnetic state of the Mn3 sublattice.

According to the sequential field-induced processes illustrated in Fig. 5.3 (b), we can quantitatively estimate the concentration of the three Mn sublattices based on the $M(H)$ data. If we set the amount of the Mn2 and Mn3 antisites and the Mn occupancy on the Mn1 site to be m, n and l respectively, then the concentration of the Mn1, Mn2 and Mn3 sublattices is $1-l$, $2m$ and $2n$ with $2m+2n+(1-l) = Mn^{\mathrm{WDS}}$ where $\mathrm{Mn}^{\mathrm{WDS}}$ is the total Mn

concentration determined by the WDS measurement. Assuming the ordered-moment/Mn for Mn1, Mn2 and Mn3 is the same, we can readily write down a set of equations based on Fig. 5.3(b):

$$(l - 2m)/\mathrm{Mn}^{\mathrm{WDS}} = \alpha/\gamma \tag{5.1}$$

$$(l - 2m + 2n)\mathrm{Mn}^{\mathrm{WDS}} = \beta/\gamma \tag{5.2}$$

$$(2m + 2n + l)/\mathrm{Mn}^{\mathrm{WDS}} = 1 \tag{5.3}$$

For the $x = 0.76$ sample, $\mathrm{Mn}^{\mathrm{WDS}} = 0.82$. We take the moment at 1 T as α where the subtle slope change in $M(H)$ suggests the onset of the polarization process of the Mn3 sublattice. We then take the moment at 13 T as β and assume $\gamma = 5\ \mu_B$/Mn. Using these values, we estimate m, n and l to be 0.060(5), 0.07(1) and 0.56(3). For the other dopings, since $M(H)$ was only measured up to 7 T, we set β to be the moment at 7 T plus $0.1\mu_B$/Mn. The obtained m, n and l are summarized in Table 5.1.

Keeping the afore discussed defect estimation in mind, next let us switch gear back to the neutron data. Quantitatively, since this is a doped system with multiple types of defects, we have to make several assumptions for the refinement. Firstly, for the magnetic reflection data taken at 5 K, we fix the ordered moment of Mn3 as 0 and the concentration of Mn3 as 0.07; we then assume a fixed moment of 4.6 μ_B/Mn for Mn1 and Mn2, the same value as that of the parent $MnBi_4Te_7$ obtained from neutron scattering [81]. By these restrictions, Mn1 and Mn2 occupancy are refined. Secondly, the Mn1 and Mn2 occupancies are then used for a more comprehensive structural refinement for the scattering data at 50 K to better determine the atomic coordinates and the Sb and Bi level. Such information is then fed back to the magnetic refinement of the 5 K data. A recursive process is repeated until all values converge. Eventually, the refinement with 27 reflections at 5 K yielded R_F=3.03% and $\chi^2 = 1.99$; the refinement with 118 reflections at 50 K yielded R_F=2.16% and $\chi^2 = 1.46$. The refinement result is summarized in Table 5.2 and Table 5.1. Our refinement unambiguously shows site mixing. Opposite magnetic moments are observed in Mn1 and Mn2 sites, suggesting the $\mathrm{Ferri}^{\mathrm{FM}}$ state. m is 0.06(1), l is 0.62(1) and the total Mn concentration is 0.88(3). Considering that the Mn3 concentration is fixed with no error in the neutron refinement which will lead to

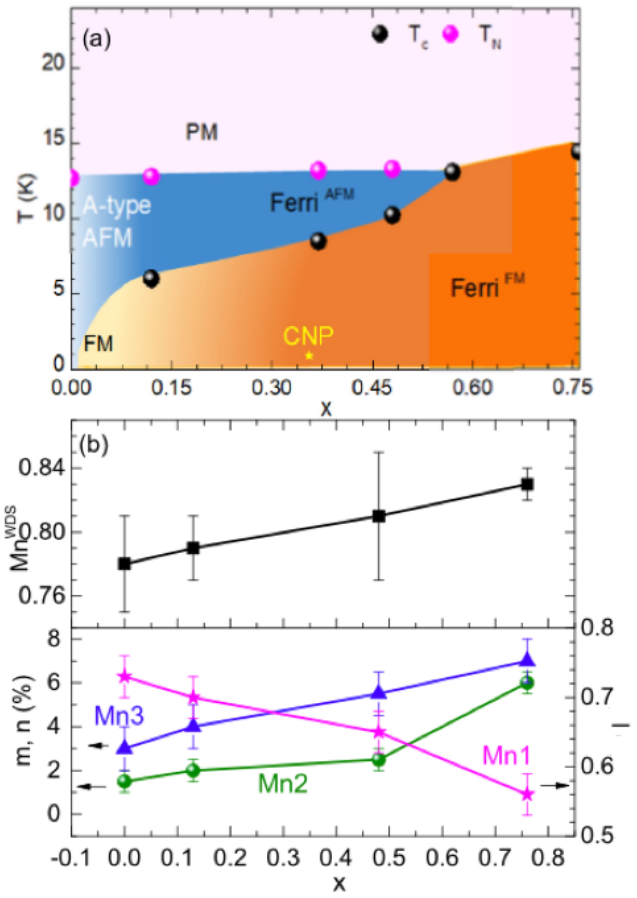

Figure 5.6: (a) The temperature-doping (T-x) phase diagram. With increasing x, the carrier-type changes from electron to hole. A linear fitting with the carrier density data in Figure 5.4 yields a charge neutrality point (CNP) near x= 0.36. (b) The doping-dependent Mn^{WDS}, m, n and l.

a smaller error bar in the total Mn concentration, these defect concentrations are consistent with the ones obtained from the $M(H)$ and WDS data. In addition, Sb atoms are found to be inhomogeneously doped in each site. The Sb has an overall higher concentration in the SLs than in QLs. In the Mn1 site, no Bi is found at all.

Table 5.2: Refined structural parameters for the $Mn(Bi_{1-x}Sb_x)_4Te_7$ for x =0.76 based on single crystal neutron diffraction measurement at 50 K and 5 K.

Name	x	y	z	occ.	Moment at 5 K
Mn1	0	0	0.5	0.623(4)	4.6 μ_B/Mn
Bi1	0	0	0.5	0	
Sb1	0	0	0.5	0.377(4)	
Bi2	0.333	0.667	0.342(1)	0.21(2)	
Sb2	0.333	0.667	0.342(1)	0.73(2)	
Mn2	0.333	0.667	0.342(1)	0.06(1)	-4.6 μ_B/Mn
Bi3	0.333	0.667	0.0842(1)	0.37(2)	
Sb3	0.333	0.667	0.0842(1)	0.56(2)	
Mn3	0.333	0.667	0.0842(1)	0.07	0
Te1	0	0	0	1	
Te2	0.333	0.667	0.155(1)	1	
Te3	0	0	0.273(1)	1	
Te4	0.333	0.667	0.430(1)	1	

5.5 Understanding the doping and temperature-dependent magnetic evolution

We argue that the AFM to FM transition of the dominate Mn1 sublattice arises from the delicate competitions between the direct Mn1-Mn1 AFM interlayer interaction and Mn3-assisted Mn1-Mn1 FM interlayer coupling. The magnetic Hamiltonian may be approximated as follows. The Mn1 sublattice itself has strong FM intralayer couplings J_0 and weak interlayer AFM interactions J_1. The Mn2 and Mn3 sublattices are so sparse that the interactions among themselves are negligible, but they couple to Mn1 through strong superexchange interactions J_2 and J_3 due to their proximity. Finally, there is Mn2-Mn3 coupling, which modifies J_3 into J_3^{eff}. Note that the sign of J_3^{eff} can vary from site to site (for instance, depending on whether the closest Mn neighbor to a Mn is Mn1 or Mn2).

Now, while Mn2 just follows Mn1 and does not affect the overall Mn1-Mn1 interlayer ordering, Mn3 introduces an effective FM interlayer coupling when they couple to the neighboring Mn1 layers above and below:

$$H_{\text{interlayer}} = J_1\langle \mathbf{M}_1 \cdot \mathbf{M}_1' \rangle + \langle J_3^{\text{eff}}(\mathbf{M}_1 \cdot \mathbf{M}_3 + \mathbf{M}_1' \cdot \mathbf{M}_3)\rangle, \tag{5.4}$$

where $\mathbf{M}_1$ and $\mathbf{M}_1'$ are the local magnetization of the two neighboring Mn1 layers, $\mathbf{M}_3$ is the local magnetization of the Mn3 bilayer between these Mn1 layers, and the brackets denote the average of the *ab* plane. The second term equals 0, if the Mn1 sublattice is AFM, and $-2\langle|J_3^{\text{eff}}M_3M_1|\rangle$, if the Mn1 sublattice is FM, regardless of the sign of J_3^{eff}; thus it always favors the FM ordering of the Mn1 sublattice (that is, the Mn3 mediates FM interlayer coupling of the Mn1 sublattice). We can see that if $|2c_3J_3^{\text{eff}}M_3| > c_1J_1M_1$, the system orders into the Ferri^{FM} state with the energy $E_1 = c_1J_1M_1^2 - 2c_3|J_3^{\text{eff}}M_3M_1|$, and otherwise into the Ferri^{AFM} state with $E_2 = -c_1J_1M_1^2$,where c_1 and c_3 are the concentrations of the Mn1 and Mn3 sublattice.

This consideration implicitly implies that the susceptibility of the Mn3 subsystem is infinite, which would be true at $T = 0$, and if the Mn3-Mn3 interaction can be neglected. Our neutron scattering indicates that Mn3 spins are strongly fluctuating, which suggests that

the susceptibility of this subsystem, χ_{Mn3}, is finite. This does not change the conclusions qualitatively; the only change is that if χ_{Mn3} is relatively small, the net Mn3 subsystem magnetization M_3 becomes proportional to $M_1\chi_{\mathrm{Mn3}}(T)$, and thus explicitly T-dependent.

With this in mind, we can explain both the temperature and doping evolution of the magnetism. Because of the Mermin-Wagner physics, M_1 only weakly depends on T except close to T_N. Meanwhile, as long as the concentration of Mn3 remains low, Mn3 can be treated as free spins in an external field (the molecular field induced by Mn1) with $M_3 \propto \chi_{\mathrm{Mn3}}(T) \propto 1/T$. Thus, upon cooling, the effective FM interaction increases much faster than the AFM, resulting in a Ferri^{AFM} to Ferri^{FM} transition at $T_C < T_N$ once $|2c_3J_3^{\mathrm{eff}}M_3| > c_1J_1M_1$. Furthermore, Fig. 5.6(b) and the comparison of the neutron refinements of the $x = 0$ [72] and $x = 0.76$ samples all indicate that c_3 increases and c_1 decreases with Sb doping. Therefore, inevitably, in the $T - x$ phase diagram, three doping regimes can appear: low doping region where the Ferri^{AFM} state is stable at any temperature, high doping region when only the Ferri^{FM} state is stable, and intermediate doping region, where the Ferri^{FM} state is stable only up to some $T_C < T_N$ with T_C increasing with x. This doping dependence is exactly what we have observed in Fig. 5.6(a).

We note that l decreases with increasing x, so besides the formation of antisites, Sb doping also leads to the magnetic dilution effect of the Mn1 sublattice. Future doping studies, such as Pb, Sn or Ge substitution on Mn site, if they will not cause antisite defects as the Sb doping does, may provide a cleaner platform to investigate the magnetic dilution effect on the magnetism in the $MnBi_{2n}Te_{3n+1}$ family.

5.6 Band topology

In Chapter 3, we find that $MnBi_4Te_7$ is an antiferromagnetic topological insulator.

For the doped compounds with FM ground states, we discuss two limiting cases. In case I, no defect is considered and FM configuration is used. In case II, a large amount of antisites are studied and the Ferri^{FM} order is used. For the sake of feasibility, in case II, we assume

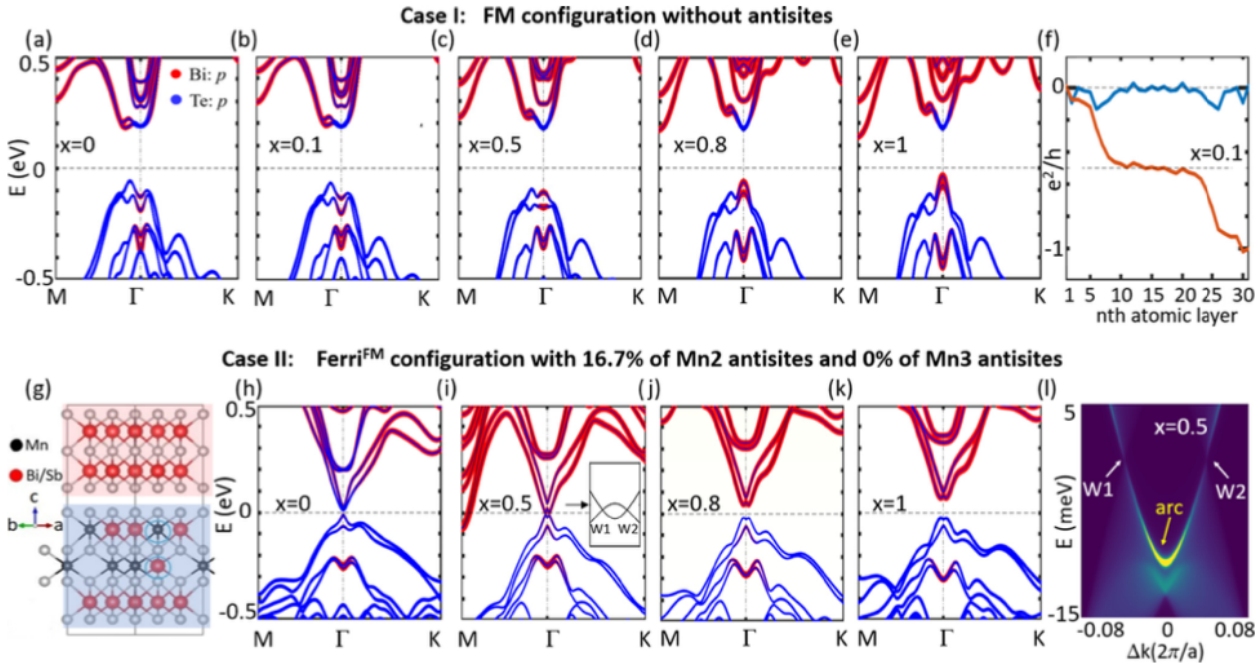

Figure 5.7: (a-f) DFT calculations in the defect-free and FM configuration case: (a-e) Bulk band structures. The red and blue dots indicate (Bi,Sb)-p and Te-p orbitals, respectively. (f) Layer-resolved AHC for $x = 0.1$ sample. Partial AHC of each atomic layer (blue line); Integral of the partial AHC (red line). (g-l) DFT calculations in the 16.7% of periodic Mn2 antisites and Ferri^{FM} configuration case: (g) The depiction of the structure model used. (h-k) Bulk band structures. (l) Surface band structure ($x = 0.5$) along the momentum space cut that goes through a direct pair of Weyl nodes W1 and W2.

only Mn1 and Mn2 sublattices exist and 16.7% of Bi/Sb atoms in the SLs exchange with the Mn atoms on the same layer to form Mn2 antisites. The value is close to the antisite concentration in $MnSb_2Te_4$ [107], but much larger than that in our samples. Hence this will give an exaggerated effect of antisites.

5.6.1 Case I: the defect-free scenario

We first construct a tight-binding Hamiltonian for both FM $MnBi_4Te_7$ and $MnSb_4Te_7$ using our experimental lattice parameters in Fig. 5.1. Then the electronic structures of the doped compounds are calculated by a linear interpolation of tight-binding model matrix

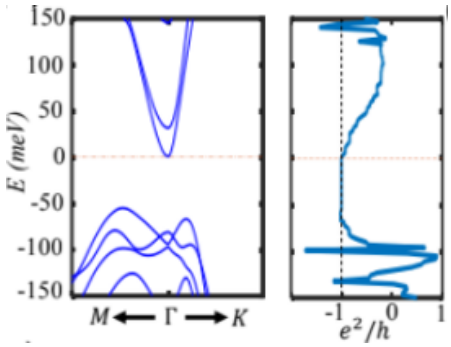

Figure 5.8: Band structures of the vacuum-[SL-QL-SL-QL-SL]-vacuum atomic layer finite-sized slab model for defect-free case and the corresponding anomalous Hall conductivity (AHC) for $x = 0.1$.

elements of the Hamiltonians. This approach was successfully applied to investigate the evolution of band topology in $BiTlSe_{1-x}S_x$ TI and $Mo_xW_{1-x}Te_2$ Weyl semimetal [112, 113]. By that, the calculated band structure without defects is shown in Figs. 5.7(a)-(e).

For all doping levels, a sizable band gap of 200–300 meV opens, with a band inversion between the (Bi, Sb)-p and Te-p states in the vicinity of E_F. Our topological invariant calculations show the Chern numbers to be zero both in the $k_z = 0$ and $k_z = \pi$ planes. Next, we compute the parity-based higher-order Z_4 invariant, which is defined by $Z_4 = \sum_{i=1}^{8} \sum_{n=1}^{n=occ}[(1 + \xi_n(\gamma_i)]2 \; mod \; 4$, where $\xi_n(\gamma_i)$ is the parity eigenvalue (+1 or -1) of the n-th band at the i-th time reversal invariant point Γ_i and n = occ is the number of occupied bands [46]. The Z_4 invariant is well defined for an inversion symmetric system, even in the absence of time reversal symmetry. The odd values of Z_4 (Z_4=1,3), indicate a Weyl semimetal phase, while $Z_4 = 2$ corresponds to an insulator phase with a quantized topological magnetoelectric effect (axion coupling $\theta = \pi$) [80, 114]. Our calculation shows the Z_4 invariant of $Mn(Bi_{1-x}Sb_x)_4Te_7$ with FM configuration to be 2 for all x, which suggests a 3D FM axion insulator phase.

To show the novel physics, taking the $x = 0.1$ compound as an example, we further investigate the anomalous Hall conductivity (AHC) in the 2D limit. Figure 5.8 show the vacuum-[SL-QL- SL-QL- SL]-vacuum band structure of the slab model and the corresponding

AHC. Our calculation shows that the Hall conductivity exhibits a quantized plateau AHC $= -e^2/h$ when the E_F is gated inside the energy band gap. Otherwise the intensity of AHC decreases rapidly when EF shifted away from the gap. Next, we project the AHC onto a real space of the slab model based on the local Chern number density [34]. The equation of the layer-resolved AHC can be expressed as

$$\sigma_{xy}^{p}(l) = \frac{e^2}{h} \cdot \frac{-4\pi}{A \cdot N_{\boldsymbol{k}}} \mathrm{Im} \sum_{\boldsymbol{k},\alpha,\alpha',\beta} X_{\alpha,c,\boldsymbol{k}} Y^{\dagger}_{\alpha',\beta,\boldsymbol{k}} \rho_{\alpha',\alpha,\boldsymbol{k}}(l) \tag{5.5}$$

, where $X_{\alpha,c,\boldsymbol{k}} = \frac{<\alpha,\boldsymbol{k}|i\hbar\boldsymbol{v}_{\boldsymbol{x}}|\beta,\boldsymbol{k}>}{E_{\beta,\boldsymbol{k}}-E_{\alpha,\boldsymbol{k}}}$ and similarly for $Y_{\alpha',\beta,\boldsymbol{k}}$. The $\boldsymbol{v} = \frac{-i}{\hbar}[\boldsymbol{r}, H]$ in $X_{\alpha,c,\boldsymbol{k}}$ is the velocity operator. $\rho_{\alpha',\alpha,\boldsymbol{k}}(l) = \sum_j \psi^*_{\alpha,\boldsymbol{k}} \psi_{\alpha',\boldsymbol{k}}$ is the Bloch representation of the projection onto the corresponding layer l, where the j indicates the orbital index in a certain l layer. The indices α and β denote the VBs and CBs, respectively. For a 31 atomic layer symmetric slab, vacuum-[SL-QL-SL-QL-SL]-vacuum, when the E_F is gated inside the energy band gap, the layer-resolved AHC calculation (the blue line in Fig. 5.7 (f)) shows that the AHC mainly comes from the atomic layers on the top and bottom surfaces (about one SL and half QL), and the intensity rapidly decreases to approximately zero in the middle region of the device. As a result, each surface (fewer or near 10 atomic layers) contributes (the red line in Fig. 5.7(f)) $-0.5\ e^2/h$ to AHC, and gives $-1\ e^2/h$ for the whole slab. The half-integer quantized plateau in the middle indicates that the axion coupling strength equals the quantization value of π in this device, further confirming the $x = 0.1$ compound as a FM axion insulator [34].

5.6.2 Case II: periodic Mn2-antisite scenario

To include the antisite effect in case II, we perform the supercell calculation. First, we construct a $\sqrt{3}\times\sqrt{3}$ supercell of $MnBi_4Te_7$. In this model, one atomic Mn layer contains three Mn atoms (Mn1 sublattice). Then we exchange one Mn atom and one Bi atom within the SL (Mn2 sublattice), resulting a chemical formula of $(Mn_{0.67}\ Bi_{0.33})\ (Bi_{0.833}\ Mn_{0.167})_2Te_4{\cdot}Bi_2Te_3$ as shown in Fig. 5.7(g). By this, we calculate the band structure of $MnBi_4Te_7$ with 16.7% of the antisite disorder. We then perform a similar procedure to calculate the band structure of $(Mn_{0.67}\ Sb_{0.33})\ (Sb_{0.833}\ Mn_{0.167})_2Te_4{\cdot}Sb_2Te_3$. Finally, electronic structures of the doped

compounds are calculated by a linear interpolation of tight-binding model matrix elements of the Bi and Sb versions.

Our calculation indeed shows that, in this defect limit, the magnetic configuration of Mn1 and Mn2 is FM individually while Mn1 and Mn2 are coupled antiferromagnetically, forming the Ferri^{FM} ground state. In the Ferri^{FM} state, the bulk band gap of $MnBi_4Te_7$ is greatly reduced to about 20 meV. Meanwhile, the character of the band inversion also alters with doping, as shown in Figs. 5.7(h)-(k). Consequently, in the intermediate doping region at $x = 0.5$ for example, one can see a small energy gap about 10 meV near the Γ point (inset of Fig. 5.7 (i)). This tiny gap implies the existence of a Weyl semimetal state. Since the gapless Weyl points are not guaranteed to locate on the high symmetry point or the high symmetry line, to confirm the chirality of the Weyl nodes, we calculate the chiral charge based on the Wilson loop method. The associated chiral charge for W1(W2) is calculated to be $-1(+1)$ based on the Wilson loop method, indicating that they carry opposite chirality and do form a pair of Weyl nodes. Furthermore, a topological Fermi arc state, the characteristics of Weyl semimetal, appears in the (100) surface states and terminates directly at the projected Weyl nodes (Fig. 5.7(l)). This further supports the picture of a ferrimagnetic type-I Weyl semimetal with only two Weyl nodes.

5.6.3 Summary on topology

It remains an open but important question how robust the nontrivial band topology and thus the associated emergent phenomena will be against the antisite defects. Recent studies showed that Mn antisites are universal in $MnBi_{2n}Te_{3n+1}$; $\sim 3(1)\%$ for $MnBi_2Te_4$ and $\sim$ 13%-16% for $MnSb_2Te_4$ [107, 111]. While it is impossible to construct a structure model to reflect the real and complex chemical defects in our DFT calculations, our attempts with the defect-free and periodic-Mn2-antisites scenarios shed light on this puzzle. Two insightful observations can be made from Fig. 5.7.

First, in case II, the effect of Mn2 antisites is exaggerated on the band topology, especially for the low and intermediate dopings where the antisite defects are significantly smaller than

16.7%. However, even in this high-concentration case with periodic antisites, our calculations show robust band inversion and non-trivial topology, resulting in a Weyl semimetal state at the intermediate dopings. Second, in the Bi-rich side, the characteristics of the band inversion are very similar for the two cases (Figs. 5.7(a) and (h)). However, in the Sb-rich side, the features of band inversion are apparently different (Figs. 5.7(e) and (k)). This observation implies that the antisite defect has stronger effect on modifying the band topology in the Sb-rich 147 phase than the Bi-rich 147 phase. Therefore, we believe that the non-trivial topology is likely robust against the small amount of antisite defects here, especially at the Bi-rich side. Our finding is consistent with the observation that despite 3(1)% of antisite defects, a zero-field QAH effect appears at 1.5 K in a 5-SL device of $MnBi_2Te_4$ [54]. Future systematic ARPES measurements, in combination with the DFT calculations on Sb doped $MnBi_4Te_7$, will help settle this outstanding question.

5.7 Summary and outlooks

In Sb doped $MnBi_4Te_7$, the competition of the Mn1-Mn1 AFM interlayer coupling and the Mn3-assisted Mn1-Mn1 FM interlayer interaction leads to lower-temperature Ferri^{FM} state and higher-temperature Ferri^{AFM} state where the Mn3 sublattice is dynamically fluctuating at all temperatures. Meanwhile, the non-trivial band topology appears robust against low or intermediate antisites, pointing to a kaleidoscope of magnetic topological phases including the FM axion insulator state at low Sb-dopings and possible type-I ferrimagnetic Weyl semimetal states at intermediate Sb dopings. Future work in fine tuning the Sb doping level to the charge neutrality point so that quantum oscillation study can be made to shed light on this type-I FM Weyl semimetal state is strongly urged.

CHAPTER 6

Magnetic dynamics in FM $MnBi_{2n}Te_{3n+1}$ family

The majority of this chapter has been adapted from [115]. This work was done in collaboration with Ruslan Prozorov's group at Ames lab on the magnetic imaging measurements.

6.1 Introduction

In Chapter 3 and 4, we have shown how to reduce the interlayer AFM coupling by adding nonmagnetic Bi_2Te_3 QL between [$MnBi_2Te_4$] SLs to physically separate the magnetic SLs. By this design, $MnBi_4Te_7$ and $MnBi_6Te_{10}$ are found to be weakly-coupled A-type AFM [50, 72, 89, 89, 92–94, 101–103, 116, 117], and ferromagnetism is achieved in $MnBi_8Te_{13}$ [80, 81]. In Chapter 5, we have discussed the effect of doping Bi by Sb. Upon Sb doping, $Mn_{(Bi,\ Sb)}$ antisites are produced and enhanced due to the tendency of Sb and Mn to form antisites. The presence of antisites introduces additional Mn sublattices which facilitates FM coupling of the dominant Mn sublattice [100, 107, 118, 119]. As a result, the magnetic transition of the dominant Mn sublattice becomes FM-like in high-antisite $MnSb_2Te_4$. [107, 118, 119], Sb-doped $Mn(Bi_{1-x}Sb_x)_4Te_7$ [100], and Sb-doped $Mn(Bi_{1-x}Sb_x)_6Te_{10}$ [120].

Despite much efforts in studying magnetic properties of the $MnBi_{2n}Te_{3n+1}$ family, most works have been only about the steady state. For practical applications, especially in the pursuit of high-temperature QAHE when fluctuations become important, the study on magnetic dynamics is indispensable for the ferromagnetic members. A slow magnetic relaxation behavior was found in $Mn(Bi_{0.7}Sb_{0.3})_6Te_{10}$ at low temperatures. This behavior is attributed to the vanishing interlayer coupling due to the large interlayer distance between SLs for $n \geq 2$ [120]. This so-called single-layer magnetism picture is a two-dimensional analog of the

single-molecule magnet, a typical system to exhibit the superparamagnetic (SPM) behavior. In the other limit, the slow relaxation dynamics is also found in FM $MnSb_2Te_4$ [121], where the interlayer distance is much smaller. A frequency-dependent peak shift $\chi'(T)$ is attributed to a spin glass (SG) state, but the mechanism of the glassiness is unclear.

To understand the origin of the relaxation behavior in this family, we perform a comprehensive study of the dynamical magnetic properties in FM $MnBi_8Te_{13}$, $Mn(Bi_{0.93}Sb_{0.07})_6Te_{10}$ and $Mn(Bi_{0.24}Sb_{0.76})_4Te_7$ by the AC susceptibility and magneto-optical image measurements. We show that the slow relaxation behavior is universal among all FM $MnBi_{2n}Te_{3n+1}$ members, which arises from the dynamics of irreversible domain wall movements rather than the SPM or SG scenarios. Our study suggests FM domains in $MnBi_{2n}Te_{3n+1}$s are very soft and weakly pinned, resulting a unique "double-peak" behavior in the real part of the AC susceptibility $\chi'(T)$ under DC fields.

6.2 Magnetic relaxation revealed by AC susceptibility

In Figure 6.1, we show the zero-field-cooled (ZFC) and field-cooled (FC) DC temperature-dependent susceptibility $\chi(T)$ and isothermal magnetizations $M(H)$ of the three compounds. The T_C determined at the sharp turn in $\chi(T)$ [80,100] are at 14.2 K, 11.1 K and 10 K respectively. The difference in the ordering temperatures among the three, from $Mn(Bi_{0.24}Sb_{0.76})_4Te_7$ to $MnBi_8Te_{13}$, lies in both the increasing interlayer distance and the decreasing extent of the $Mn_{(Bi,\ Sb)}$ antisites. The larger the distance, the weaker the interlayer interaction, so T_C is the lowest in $MnBi_8Te_{13}$. As antisites switch the dominant Mn sublattice from AFM to FM in $MnBi_4Te_7$ and $MnBi_6Te_{10}$, they also increase the overall interlayer interaction and hence give rise to the higher T_C than the Néel temperature of the parent compounds [50]. In the $M(H)$ data presented in Figs. 6.1(b)(d)(f), FM hysteresis can be seen at 2 K for all compounds, and is the smallest in $Mn(Bi_{0.24}Sb_{0.76})_4Te_7$ and the largest in $MnBi_8Te_{13}$. The softness of a FM is controlled by two factors, one is the magnetocrystalline anisotropy, the other is defect. The crystalline anisotropy is proportional to the coercive field according to the Stoner-Wohlfarth model for a single-domain FM, while the defects tend to provide

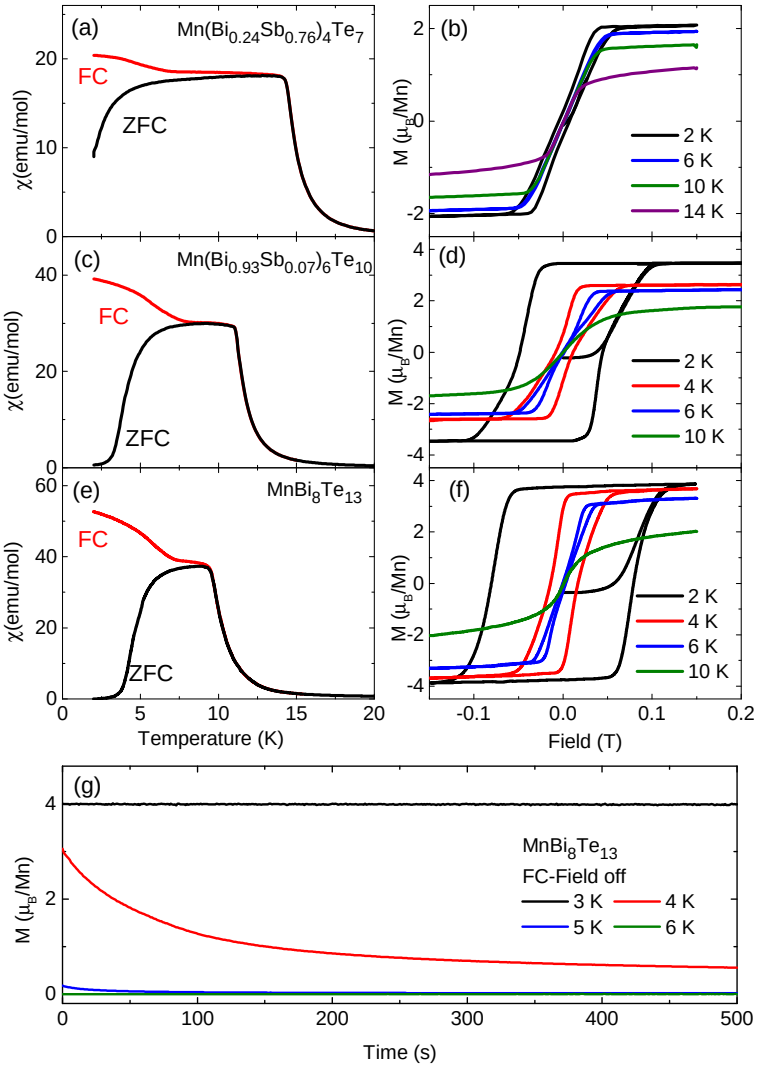

Figure 6.1: (a)(c)(e) The temperature-dependent zero-field-cooled (ZFC) and field-cooled (FC) magnetic susceptibility under 0.01 T with $H \| c$. (b)(d)(f) The isothermal magnetization $M(H)$ at various temperatures. (g) The time dependence of the magnetization at various temperatures after $MnBi_8Te_{13}$ is FC under 0.1 T and then switched off.

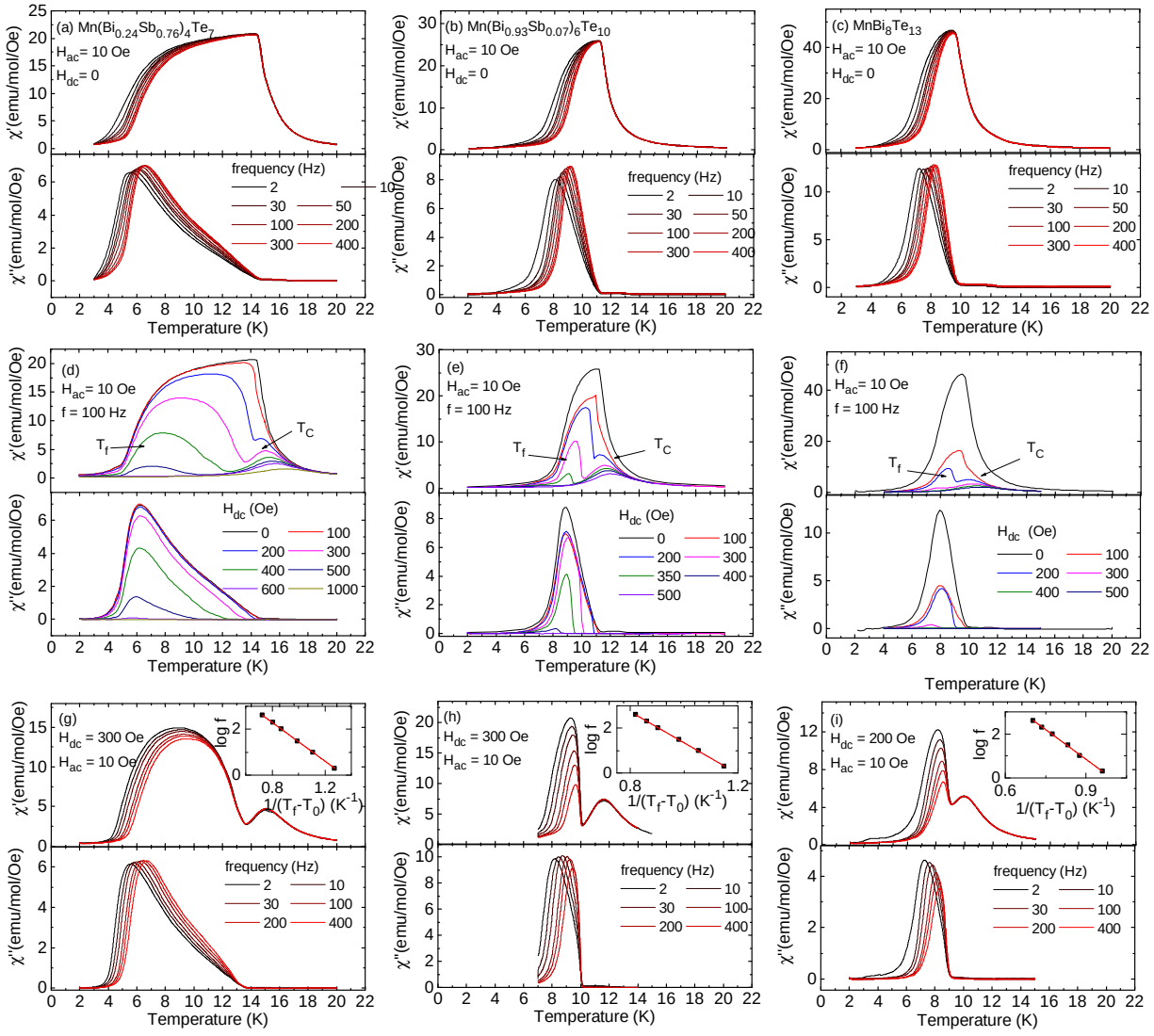

Figure 6.2: The temperature-dependent AC susceptibility for the FM $Mn(Bi_{0.24}Sb_{0.76})_4Te_7$, $Mn(Bi_{0.93}Sb_{0.07})_6Te_{10}$ and $MnBi_8Te_{13}$ measured in different conditions with H_{ac} and H_{dc} parallel to the c axis. (a-c) $H_{ac} = 10$ Oe with different sweeping frequency f; $H_{dc} = 0$ Oe. (d-f) $H_{ac} = 10$ Oe with $f = 100$ Hz; H_{dc} varies. (g-i) $H_{ac} = 10$ Oe with varying f; $H_{dc} = 300$ Oe. Insets: Vogel-Fulcher fitting showing linearity between the log of f and $1/(T_f\text{-}T_0)$.

more pinning. Thus the higher the magnetocrystalline anisotropy, the harder the FM; the more the defects, the harder the FM. Since the saturation field of $MnBi_8Te_{13}$ with $H//ab$ is about 3 times of that for $Mn(Bi_{0.24}Sb_{0.76})_4Te_7$, the former has higher magnetocrystalline anisotropy [80, 100]. Meanwhile, neutron scattering data suggest that $Mn(Bi_{0.24}Sb_{0.76})_4Te_7$ has more defects than $MnBi_8Te_{13}$ [80, 100]. Therefore, the fact that $MnBi_8Te_{13}$ is the hardest among all three suggests that the magnetocrystalline anisotropy dominates the level of softness in $MnBi_{2n}Te_{3n+1}$, which indicates that the domain pinning caused by the defects is very weak in $MnBi_{2n}Te_{3n+1}$. We also note that the hysteresis curves are non-trivial with the "bow-tie"-shaped hysteresis most clearly demonstrated at around 6 K in Fig. 6.1(d) and (f). This unusual hysteresis loop can be linked to the anomalous behavior of the FC $\chi(T)$. Instead of a smooth increase with establishing FM order upon cooling, FC $\chi(T)$ first shows a flat plateau below T_C before a clear slope change can be observed in the FC $\chi(T)$ near 6 K. These anomalous observations are likely to be caused by possible non-trivial domain formation in $MnBi_{2n}Te_{3n+1}$, as will be discussed later.

To probe the non-steady state directly, we performed a DC scan to study the relaxation in $MnBi_8Te_{13}$ at constant temperatures over a long time. The measurement was taken after the sample was FC under 0.1 T to the target temperature and then the field was switched off. A clear relaxation of the overall magnetization can be observed. The time scale for the relaxation depends heavily on the temperature. As shown in Fig. 6.1 (g), it is on the order of hundred seconds at 4 K and tens of seconds at 3 K. However, at temperatures below 3 K, the relaxation is simply too slow to see any decay of moment; at temperatures above 5 K, the relaxation time is so short that all moments fully decay before we make measurements. This motivates us to use the AC susceptibility to study the relaxation phenomena more comprehensively.

The temperature-dependent AC susceptibility of the three compounds measured under an AC field of $H_{ac} = 10$ Oe with different frequencies are summarized in Figs. 6.2(a)-(c). When $f = 2$ Hz, $\chi'(T)$ has the similar shape and peak position to that of the ZFC $\chi(T)$ data, but it is narrower on the low temperature end. In addition, non-zero $\chi''(T)$ can be detected

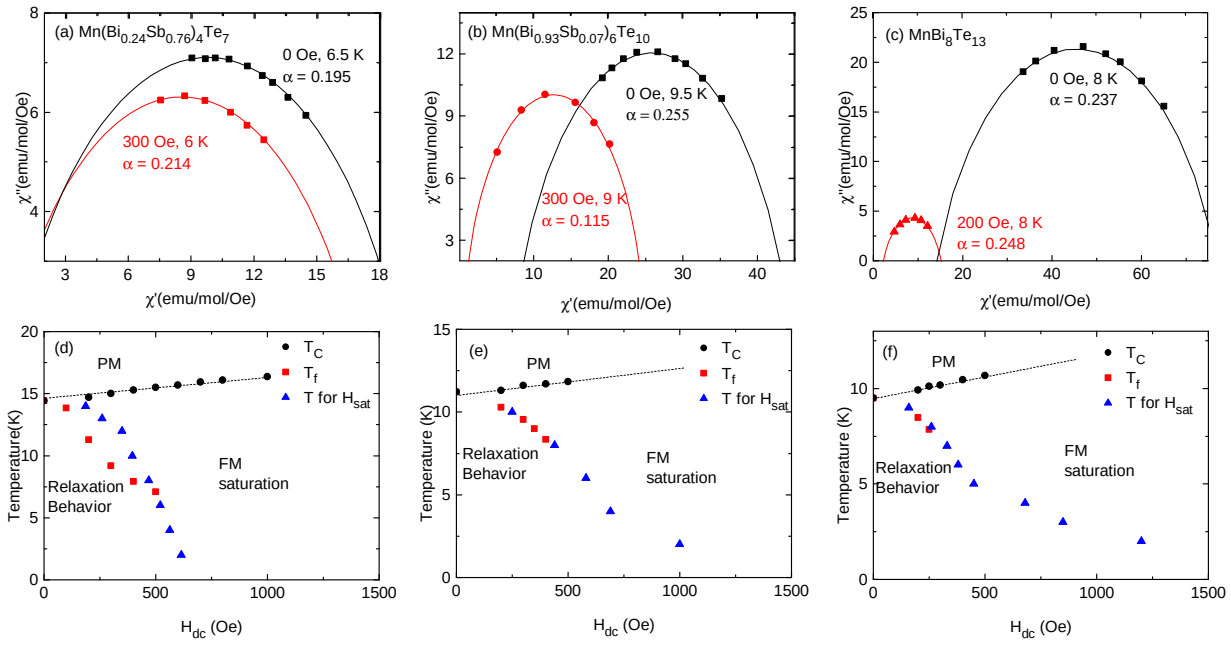

Figure 6.3: (a-c) Cole-Cole plots for $Mn(Bi_{0.24}Sb_{0.76})_4Te_7$, $Mn(Bi_{0.93}Sb_{0.07})_6Te_{10}$ as well as $MnBi_8Te_{13}$. $\chi''(\chi')$ data are taken from AC susceptibility at the selected temperature and DC field, across various frequencies. The fittings are done with Eqn. 6.4. (d-f) The DC field-temperature phase diagrams mapped via the AC susceptibility data. Also included are the saturation fields H_{sat} obtained in the $M(H)$ measurements.

in all FM compounds. This confirms the presence of slow relaxation in the FM state, whose time scale is close to the oscillation period of the applied AC field. $\chi''(T)$ is peaked near 6 K, 9 K and 8 K for $Mn(Bi_{0.24}Sb_{0.76})_4Te_7$, $Mn(Bi_{0.93}Sb_{0.07})_6Te_{10}$ and $MnBi_8Te_{13}$ respectively, where $\chi'(T)$ has the steepest increase with temperature. With increasing AC frequency, the overall weight of the entire $\chi'(T)$ and the low-temperature-end of $\chi'(T)$ shift to higher temperatures, concurrent with the frequency-dependent peak shifts in $\chi''(T)$. Meanwhile, the peak position in $\chi'(T)$ signaling T_C shows no frequency dependence and $\chi''(T)$ drops to zero at T_C, unlike that of a typical SG or SPM [122, 123].

In attempt to single out the frequency dependent component, we then performed the AC susceptibility measurements at $H_{ac} = 10$ Oe and $f = 100$ Hz under various DC field bias (H_{dc}). The result is summarized in Fig. 6.2 (d)-(f). Remarkably, in all three compounds, an additional low-T peak appears in $\chi'(T)$ under H_{dc}, resulting in the unusual "double-peak" feature. As H_{dc} increases, the original high-T peak slightly moves to higher temperatures while the low-T peak shifts to lower temperatures quickly. The magnitudes of these two peaks in $\chi'(T)$ decrease upon increasing H_{dc} and the low-T peak is completely suppressed with merely 600 Oe, 400 Oe, and 300 Oe in $Mn(Bi_{0.24}Sb_{0.76})_4Te_7$, $Mn(Bi_{0.93}Sb_{0.07})_6Te_{10}$ and $MnBi_8Te_{13}$, respectively.

To better understand this rare AC magnetic behavior under H_{dc}, we measured the AC susceptibility with varying f under a fixed H_{dc}. The data are shown in Figs. 6.2(g)-(i). It turns out that the magnitude and the peak position of the high-T peak are f-independent while the low-T peak shows a strong frequency dependence, suggesting the low-T peak is related to the freezing of some relaxation mechanism while the high-T peak is associated with the long range ordering. Therefore, the temperature at the high-T or low-T peak maximum are labeled as T_C or T_f, respectively.

Next we focus on the low-T peak. No matter the underlying causes for the slow relaxation, the overall dynamics of relaxation is similar. Therefore, we can extract some characteristic parameters by analyzing the AC susceptibility data to differentiate various physical scenarios. From the frequency dependence of T_f, we can calculate the Mydosh parameter K, a measure

of the relative peak shift per log frequency, by

$$K = \frac{T_1 - T_2}{T_{f0}(\log f_1 - \log f_2)}, \tag{6.1}$$

where T_1, T_2 and T_{f0} are taken as the T_f at $f_1 = 2$ Hz, $f_2 = 200$ Hz and the DC limit (2 Hz), respectively. The obtained K for each compound are 0.025, 0.016 and 0.020 respectively. The values are a few times greater than those in canonical SG with strong interaction and cooperative freezing such as $Cu_{1-x}Mn_x$ (K =0.005) [122, 123], but much smaller than those in the non-interacting SPM with gradual blocking such as α-[$Ho_2O_3(B_2O_3)$] (K =0.28) [122–124], placing these materials in neither category.

Then we performed the Vogel-Fulcher fitting shown in the insets of Figs. 6.3(g)-(i). The frequency dependence of T_f can be fitted by the Vogel-Fulcher formula

$$\tau(T) = \tau_0 \exp(E_a/k(T - T_0)). \tag{6.2}$$

Here, τ is the most probable relaxation time for the system to overcome the energy barrier for spin reversal. At T_f, τ can be taken as $1/f$. E_a is the thermal activation energy barrier for the spin reversal, τ_0 is a time constant which is temperature-independent and usually larger than 10^{-13}s [125]. T_0 is an empirical parameter in order to account for the deviation from a single-relaxation-time process due to the interaction between moments. Hence T_0 would be zero for an ideal non-interacting SPM. Yet fitting with $T_0 = 0$ would yield an unphysical value with $\tau_0 < 10^{-30}$s for all three samples. For the best fitting shown in the insets, T_0 and τ_0 are found to be around 8.16 K and 2.0×10^{-6} s for $Mn(Bi_{0.24}Sb_{0.76})_4Te_7$, 8.44 K and 5.4×10^{-9} s for $Mn(Bi_{0.93}Sb_{0.07})_6Te_{10}$ and 7.14 K and 1.95×10^{-9} s for $MnBi_8Te_{13}$. This again confirms that the relaxation behavior in these materials cannot be described by a single-relaxation-time process, but rather with a certain distribution of relaxation times.

To quantify the spread of the relaxation time, we performed Cole-Cole fitting [125, 126]. The generalized Debye formula describes the dynamic susceptibility as,

$$\chi_{ac}(\omega) \equiv \chi' - i\chi'' = \chi_S + \frac{\chi_T - \chi_S}{1 + (i\omega\tau)^{(1-\alpha)}} \tag{6.3}$$

Here $\omega = 2\pi f$, χ_S and χ_T are the high frequency and static constants, respectively, and α is an empirical parameter to account for the variation of the relaxation time around τ in the

system. We can write down

$$\chi''(\chi') = -\frac{\chi_T - \chi_S}{2\tan[(1-\alpha)\pi/2]} + \sqrt{(\chi' - \chi_S)(\chi_T - \chi') + (\frac{\chi_T - \chi_S}{2\tan[(1-\alpha)\pi/2]})^2} \tag{6.4}$$

α would be 0 for an ideal SPM with single-relaxation-time process, and around 0.9 for a SG system whose relaxation time has a broad variation. We extracted the $\chi''(\chi')$ data at selected temperatures from Figs. 6.2(a)-(c) and 6.3(g)-(i), and fitted the data using Eqn. 6.4 with α, χ_S and χ_T as the fitting parameters. The results are shown in Figs. 6.3(a)-(c). The obtained α are below 0.3, far from the expected value for SG 0.9 [122]. The values are also consistent with the previous reports on $Mn(Bi_{0.7}Sb_{0.3})_6Te_{10}$ [120]. Therefore, similar relaxation process with $\alpha < 0.3$ is not just limited to systems with large SL-SL separations but likely to be present among all members with FM coupling in this family.

So far we have shown that 1) the Mydosh-parameter estimation places these three compounds in neither SG nor ideal SPM type; 2) the Vogel-Fulcher fit suggests that the relaxation time has variations, excluding the ideal SPM scenario; 3) the fit of the Cole-Cole plot leads to a relatively moderate $\alpha < 0.3$, excluding the SG scenario. This leaves us with two possible scenarios causing the relaxation behavior, the irreversible domain wall movement and cluster SG. To differentiate these two, we constructed the T-H_{dc} phase diagram which mapped out T_C, T_f and the corresponding H_{dc} shown in Figs. 6.3(d)-(f). The obtained phase diagrams are shown in Fig. 6.3(d)-(f). Also included are the saturation fields obtained in $M(H)$ from Fig. 6.1 (b)(d)(f) at different temperatures. Interestingly, the T_f line matches or stays below the data line obtained from $M(H)$ in the field regime where the low-T peaks appear. This observation suggests the relaxation behavior only occurs before the magnetization saturates, that is, when there are irreversible domain wall motions [127]. Furthermore, in the view of energy scales, this observation also excludes the cluster SG scenario since the energy of 500 Oe magnetic field is too small to suppress a cluster SG whose freezing temperature is 6-8 K.

6.3 Magneto-optical imaging of ferromagnetic domains

To directly visualize the domain shapes, Ruslan Prozorov's group at Ames lab performed the magneto-optical imaging measurements. The FM nature of $MnBi_8Te_{13}$ is unambiguously established by the direct observation of the FM domains shown in Figs. 6.4 and 6.5.

Figure 6.4 illustrates the appearance and evolution of the FM domains when a DC field is applied after the sample was ZFC to 5.2 K, well below the FM transition. So Fig. 6.4 shows the penetration of the magnetic field after ZFC. This is a direct polarized light imaging with the contrast enhanced by setting the gray-scale levels using the imaging processing software, but no structural alterations were introduced and no local corrections were performed. With the increasing applied magnetic field, the first dendrite-looking domains appear at around 650 Oe and then the dendrites grow mostly in a one-dimensional fashion, similar to freezing ice. Eventually, at higher magnetic field the entire area is filled with the dark domain along the applied field. The dendritic growth is magnetically very soft, because the domains propagate and grow with almost no lateral displacement of the domain wall, spearheaded by the domain tip.

Note that a direct comparison with the $M(H)$ curve shown in Fig. 6.1(f) indicates a somewhat lower range of magnetic coercivity field compared to the imaging in Fig. 6.4. The difference is expected and is due to the difference in sample thickness. For imaging, very thin samples were used in search for the clean surface area, whereas magnetic measurements were performed on thicker samples. Initially, in a mono-domain state, the effective magnetic field on the edge is the sum of the applied field, H_0, and demagnetizing field, $H_{edge} = H_0 - NM$, where M is volume magnetization and N is the effective demagnetizing factor [128]. For a FM sample, M is positive and the effective edge field is reduced. Therefore, for a thinner sample where N is larger than that of a thicker sample, the difference in the effective field can be quite substantial. In the future, for a more quantitative analysis, we will need to image and measure magnetization of the same sample. Here, the imaging is used as an unambiguous proof of long-range FM and it establishes a very soft nature of the magnetic domains to explain the peculiarities of the AC response.

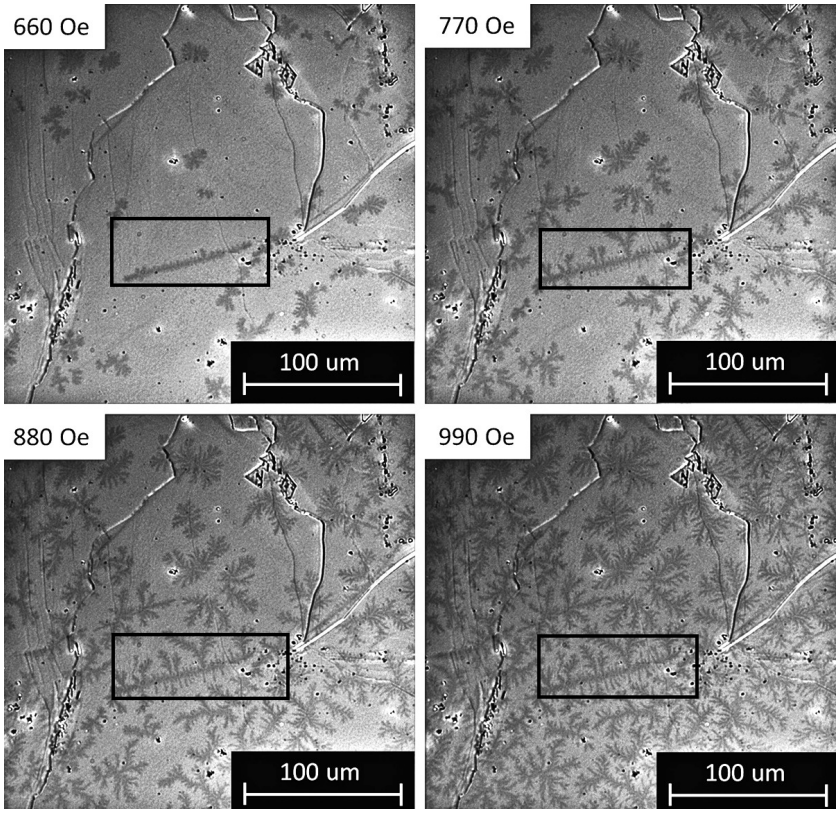

Figure 6.4: Magneto-optical polar Kerr effect imaging of the FM domains in $MnBi_8Te_{13}$. After cooling in zero magnetic field to 5.2 K (ZFC) a magnetic field of indicated amplitude was applied. Up to about 600 Oe, no domains appear. After that dendritic domains (rectangles highlight part of the dendritic domains) show up with a distinct one-dimensional grows along the dendrite tips.

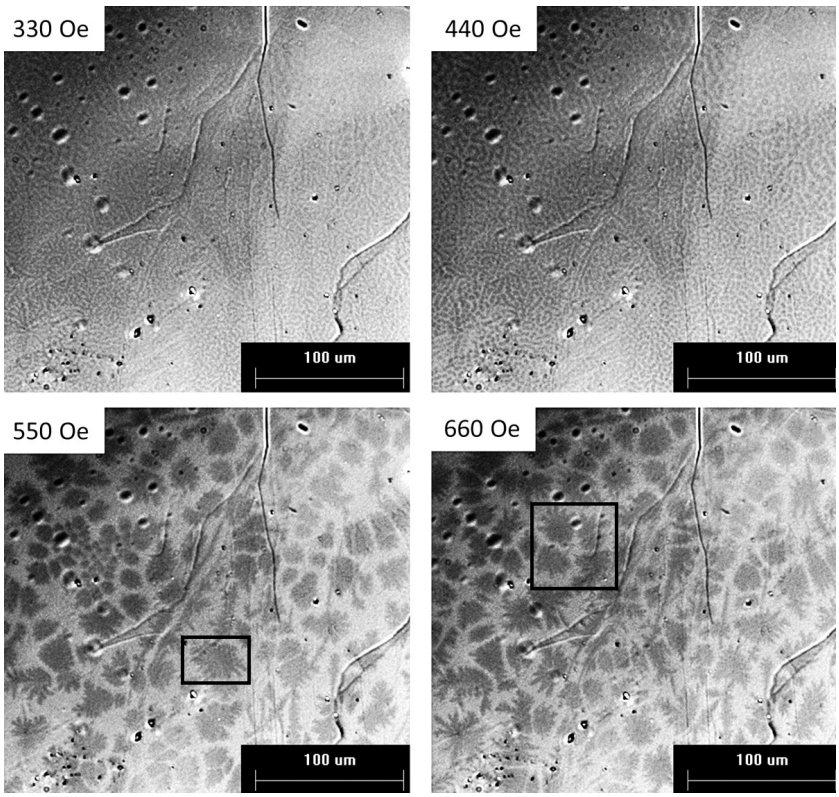

Figure 6.5: The remanent-state ferromagnetic domains in $MnBi_8Te_{13}$ crystals at 5.2 K and $H = 0$. The indicated magnetic field was applied and then removed, mimicking the "minor" hysteresis loop to investigate the irreversible coercive response. There is a significant change of the domain structure around 500 Oe with higher field triggering the appearance of sea-urchin domains (rectangles highlight part of the sea-urchin domains domains).

Figure 6.5 further demonstrates the soft nature and low coercivity of the FM state of $MnBi_8Te_{13}$ crystals. In this experiment, after ZFC to $T = 5.2$ K, the magnetic field shown in the legends was applied and then turned off (reduced to zero). So, all images in Fig. 6.5 shows flux exit and thus the structure of the magnetic remanence. While in the ZFC imaging shown in Fig. 6.4, a threshold field above 600 Oe is needed for the actual domains to appear, here we also see that the remanent-state domains do not appear up to about 300 Oe, probably indicating no domains or unsolvable fine domain structure upon minor $M(H)$ loop when the field is reduced to zero. The suggestion of a very fine structure finds indirect support in the images obtained after 330 Oe and 440 Oe were applied and removed. We see

a labyrinth-like structure, typical of very soft FM material, such as Permalloy [129]. Only above 500 Oe, the distinctly different, sea-urchin-looking structure, appears and is stabilized at the higher fields with "spines" clearly protruding off the body of the urchin-domains, suggesting small domain wall energy. Meanwhile, this pattern, when the domain of one sign (of local magnetization) is embedded into the continuous matrix of another dominant domain, is characteristic of very soft magnetic response with small domain wall energy [129].

Similar domain structures are reported for $MnSb_2Te_4$ [119], so the soft FM is universal in all FM Mn-Bi-Te members.

6.4 Discussion

Based on our observations of 1) the relaxation behavior arises from the irreversible domain movement as indicated in Figs. 6.3(d)-(f), and 2) FM in this family is very soft and the domains are quite weakly pinned as revealed in Figs. 6.4 and 6.5, we can understand the distinct "double-peak" AC response, including its f-dependence and H_{dc}-dependence shown in Fig. 6.2 as the following. Firstly, the high-T f-independent peak arises from the long-range FM ordering, which should show no AC frequency dependence and monotonic increase T_C with H_dc in Fig. 6.2 (d)-(i). Secondly, the low-T f-dependent peak is due to the relaxation from the irreversible domain movements. According to Eqn. 6.2, the irreversibility increases with lowering temperatures. Thus, upon cooling, the domain regime crosses over from saturated single domain (reversible) to the emergence of domains, and then to the peak at T_f where $\tau(T_f) = 1/f$ and finally viscously slowing down and essentially freezing out with no response to the AC field at the lowest temperatures, resulting in the relaxation peak observed.

This low-T peak should be f-dependent because the viscous force experienced by the domain walls is proportional to the instantaneous domain wall velocity, thus to the frequency. Although the relaxation is from domain formations, rather than the scenario of SG or SPM, the overall dynamics is similar to the SG, even more so, to a system of SPM nanoparticles

where instead of magnetic clusters here we have very soft and practically isotropic magnetic domains. Similar to the nanoparticles, domains are subject to a magnetic random potential pinning landscape with a spread of energy barriers for the thermally-activated relaxation, resulting in an effective barrier that depends on the driving force. This mechanism leads to f-dependent characteristic T_f where the temperature scales with the log of the frequency as shown in the inset in Figs. 6.2(g)-(i) and a moderate α between 0.1 to 0.3 in the Cole-Cole fitting as shown in Fig. 6.3(a)-(c) [130, 131].

The low-T peak should also be H_{dc} dependent. When H_{dc} is increased, the single domain region expands to lower temperatures as shown in Figs. 6.1(b), (d) and (f), so the low-T relaxation peak separates from the high-T ordering peak. The signature of peak separation in χ' upon H_{dc} was observed in the other soft FM $FeCr_2S_4$ [132]. However, it is more significant here since the FM here is softer. Such a small energy scale is a common feature in the FM members of $MnBi_{2n}Te_{3n+1}$ systems, likely due to the quasi-two-dimensionality and weak interlayer coupling.

Now let us understand the anomalous FC $\chi(T)$ and the "bow-tie"-shaped hysteresis. Figure 6.5 reveals two types of domains, one is the fine-structured one and the other is the sea-urchin one. Although both types of domains are very soft, the sea-urchin one is less isotropic and thus more irreversible. Therefore, sea-urchin domains appear and dominate at lower temperatures/higher fields while the fine-structured ones emerge at higher temperatures/lower fields. This observation shed light on the non-trivial bow-tie shaped hysteresis observed. At lower fields, the fine-structured domains dominate with very small hysteresis while at higher fields, the emergence of the sea-urchin domains leads to larger hysteresis. Following the line, the unusual slope change in FC $\chi(T)$ thus likely separates the high-temperature fine-structured domain regime from the low-temperature sea-urchin domain regime where large bifurcation of ZFC and FC data appear. Future temperature-dependent magneto-optical imaging measurements will help verify this picture.

The origin of the existence of two-types of domains may be related to the level of coupling between adjacent magnetic layers. At high temperatures or low fields, the interlayer coupling

is weak comparing to the thermal fluctuations, so each magnetic layer forms individual domains, resulting in the fine-structured domains. When FC to low temperatures or under higher fields, the interlayer coupling wins over the thermal fluctuation, leading to the larger sea-urchin-shaped domains. Future measurements such as μSR are encouraged to illuminate this scenario.

6.5 Summary

Slow relaxation dynamics is observed in the DC and AC susceptibility measurements for all FM members in the $MnBi_{2n}Te_{3n+1}$ family. Such a phenomenon arises from the irreversible domain movement below the saturation field, in these soft ferromagnets with very weak pinning. The magneto-optics provides the direct evidence for the magnetic softness, manifesting as two types of isotropic remnant-state domains, a very fine-structured one and a much larger sea-urchin one. The former tends to dominate at lower fields, and the opposite for the latter, which may explain the anomalous bow-tie-shaped hysteresis loop and the slope change in the FC temperature-dependent susceptibility. Such knowledge of the domains will be essential for the ongoing pursuit of high temperature QAHE and other topological phenomena in the $MnBi_{2n}Te_{3n+1}$ device.

CHAPTER 7

Growth, characterization and Chern insulator state in $MnBi_2Te_4$ via the chemical vapor transport method

The majority of this chapter has been adapted from [133]. This work was done in collaboration with Suyang Xu's group at Harvard University on thin-film device fabrication and transport measurement, Dan Dessau's group at University of Colorado, Boulder on ARPES measurements and Ilija Zeljkovic's group at Boston College on STM studies.

7.1 Introduction

Although $MnBi_{2n}Te_{3n+1}$ series of compounds are proposed as intrinsic MTI, chemical defects are avoidable in the $MnBi_{2n}Te_{3n+1}$ family as we have learned in Chapters 3 to 5. For flux-grown $MnBi_2Te_4$, studies find that 18(1) % of Mn sites are occupied by Bi atoms [72] while only 1-4% of Bi sites are occupied by Mn atoms [63, 72, 105, 134, 135]. Mn and Bi sites, as well as the antisite defects are displayed in Fig. 7.1 (a). This chemical complexity leads to electron carrier concentration on the order of 10^{20} cm^{-3} in samples grown by flux method or from stoichiometric melting [62, 75, 136]. Besides making the sample heavily-n doped, chemical defects have profound impacts on the magnetism and band topology of $MnBi_{2n}Te_{3n+1}$ compounds. Antisites result in additional Mn sublattices in $MnBi_{2n}Te_{3n+1}$. While the effect is relatively weak in $MnBi_2Te_4$, it is exaggerated in $MnSb_2Te_4$ [107, 137], Sb-doped $MnBi_2Te_4$ [105] and Sb-doped $MnBi_4Te_7$ [100] where sizable amount of Mn_{Sb} antisites are introduced when Sb atoms are present in the lattice, leading to ferrimagnetic ground states. From the aspect of band topology, large amount of Mn_{Sb} antisites can be

detrimental to non-trivial band topology in $MnBi_{2n}Te_{3n+1}$ [100, 107]. Because the QAHE is proposed theoretically on the ideal $MnBi_2Te_4$ structure, the defects which have caused the aforementioned complications may hinder the exploration of QAHE in $MnBi_{2n}Te_{3n+1}$. Therefore, growth of single crystals that have a lower carrier concentration, fewer defects and higher magnetic homogeneity is highly desired for the exploration of various emergent phenomena and future applications of the material.

In this chapter, we report a new single crystal growth route of $MnBi_2Te_4$ via chemical vapor transport (CVT) using I_2 as the transport agent. We find that a small thermal gradient is sufficient to drive the CVT growth and allows a good control of growth. Through magnetic, transport and spectroscopic measurements, we show the carrier density is greatly reduced in the CVT-grown samples. Chern insulator state is observed in a 6-SL device with the highest reported mobility. All evidence points to a new promising growth route so that enhanced functionality of the devices can be made.

7.2 Growth optimization

Single crystals of $MnBi_2Te_4$ were grown using CVT method with I_2 as the transport agent. Our initial trials of the CVT-growth of $MnBi_2Te_4$ were made in a Thermo Scientific muffle furnace rather than tube furnaces due to the two following considerations. First, the temperature profile of the CVT-growth is more delicate than the flux-growth of $MnBi_2Te_4$. The growth-end of the CVT-$MnBi_2Te_4$ should be kept at the temperature which is tested optimal for its flux growth. Second, a small temperature gradient of $\sim$ 2-3 K is sufficient and essential for the success of the CVT growth. As shown in Figs. 7.1(b) and (c), when the CVT-growths are positioned in the furnace, the thermal gradient intrinsic to the box furnace, either vertically between the top and bottom of the furnace, or horizontally between the heating element to the furnace center, is responsible and sufficient for driving the vapor transport. The temperature gradient is indicated by the arrows in both Figs. 7.1(b) and (c), which is only 2-3 degrees from source to end.

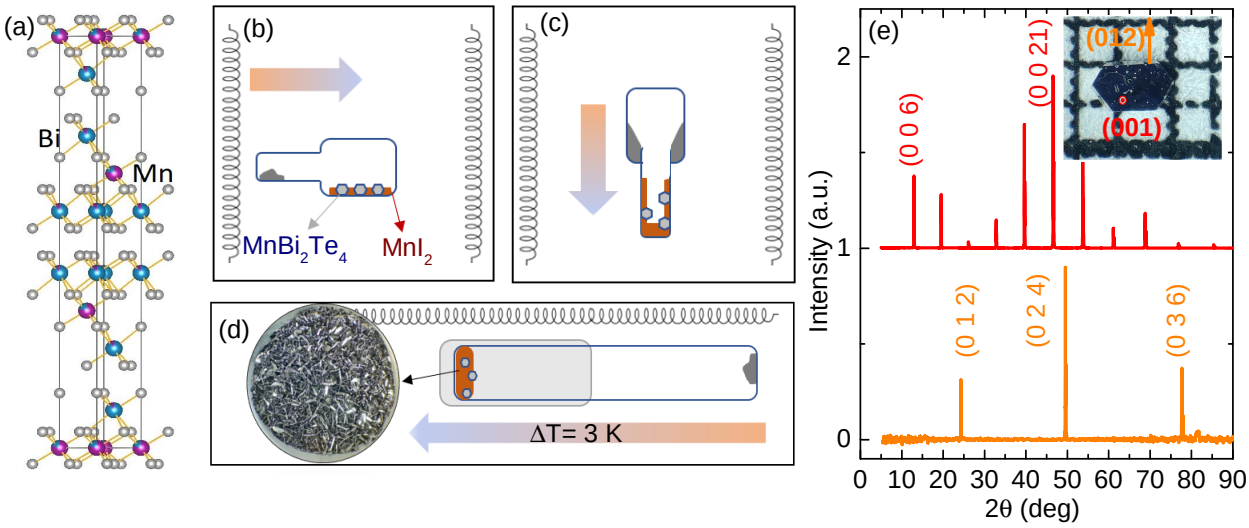

Figure 7.1: (a) Crystal structure of $MnBi_2Te_4$ with marked crystallographic Bi and Mn sites. Blue ball: Bi. Purple ball: Mn. Grey ball: Te. Mn site has Bi substitutions while the formation of Mn_{Bi} antisites results in a small amount of Mn atoms occupying the Bi site. The Mn atoms on the Mn site is denoted as Mn1, the Mn atoms on the Bi site is denoted as Mn2. Under T_N Mn1 sublattice is AFM by itself; Mn2 sublattice is AFM by itself; Mn1 and Mn2 sublattices are AFM to each other. (b-c) Schematics for the CVT growth, using the internal horizontal and vertical temperature gradient in a box furnace, respectively. The arrow indicates the gradient direction. (d) Schematics of the growth in a fine-tuned three zone furnace. Inset: mm-lateral-sized single crystals with thickness from tens to hundreds of microns after being taken out of a 19-mm-diameter tube and rinsed. (e) X-ray diffraction spectrum on the (001) surface and the (012) surface of a CVT-grown single crystal. Inset: a hexagonal shaped single crystal from an one-week growth is shown on top of the 1×1 mm-grids. The as-grown surface orientations are indexed.

Elemental form of Mn, Bi, Te and I are mixed according to the ratio of 1.7 : 2 : 4 : 1. Adding extra Mn or MnTe in the source end raises the melting point of the starting chunk, so it can remain as solid and allows a better control of its position at the source end during the transport. The elements were then sealed in a two-segment quartz tube as depicted in Fig. 7.1(b) or (c) under vacuum. The purpose of the two-segmented tube in a box furnace is to separate materials in the source (hot) and sink (cold) ends, and to have a balance over the cold-end area and transport rate so as to get sizable and abundant crystals. The quartz tube was then slowly heated to 900^{o}C overnight to avoid over-pressure. Afterwards, the tube is air-quenched and transferred back to this box furnace preset at 585^{o}C, which was pre-determined as the optimal temperature for our flux growth trials, and measured with an external thermocouple. The same thermocouple is used as the standard as we change between the furnaces, and as we measure the temperature gradient between the exact positions of hot and cold ends. In our trial-and-error process we find if the preset furnace temperature is 10 degrees higher, $MnBi_2Te_4$ in the cold end will be in the liquid form as condensed droplets; if the temperature is set to 10 degrees lower than the optimal, mixed phases of Bi_2Te_3 and $MnBi_{2n}Te_{3n+1}$ ($n \geq 2$) will form. A short tube with a length of 8-10 cm was used to ensure the minimal temperature fluctuations. It is noted that all I_2 is reacted in the first step of slow warming so MnI_2 becomes the effective transport agent. After an optimal growth time of one to two weeks, mm-lateral-sized single crystals with thickness from tens to hundreds of microns are obtained at the cold end of the growth together with red MnI_2. Longer growth time yields larger crystals, but they are more likely to grow into each other. When samples are taken out, the mixtures from the cold end are rinsed with water to remove MnI_2 and to isolate the $MnBi_2Te_4$ crystals. A crystal grown with setup in Fig. 7.1(b) is shown on top of mm-grids in the inset of Fig. 7.1(e).

With the experience of growing $MnBi_2Te_4$ in the box furnace, we can also accommodate the growth in a three-zone tube furnace. Here, a very careful calibration is needed ahead of the time at the exact location of both ends of the growth ampule. The furnace is set so that the cold end has the same temperature as that in the mid-bottom of the box furnace in

Figs. 7.1(b)(c) and the hot end is merely 3 K hotter. The cold end is then nested within an additional alumina crucible so that the temperature gradient can be further smoothed near the end as shown in Fig. 7.1(d). Eventually $MnBi_2Te_4$ and MnI_2 crystals form and almost cover the cold end of the tube. Figure 7.1(d) includes a picture showing a plate "webbed" by $MnBi_2Te_4$ single crystals which were taken from a one-month growth in a 19-mm-diameter quartz tube and rinsed with water. With the careful calibration, the CVT-growth in the tube furnace can result in higher yields than both setups in box furnaces. The crystals in the "web" can still be separated from each other for further measurements.

For comparison, $MnBi_2Te_4$ crystals were also grown using Bi_2Te_3 flux as described in Chapter 3. Comparatively, the CVT samples tend to have a hexagonal shape with well-defined edges along the a and b directions. They can be up to 1 mm thick and appear more three-dimensional with flat and shiny edge surfaces. Hence in addition to the $(00L)$ reflections, other reflections such as (012) can be observed on the as-grown surfaces on the side, as shown in Fig. 7.1(e). The two surfaces giving the XRD pattern are indexed for the crystal in the inset of Fig. 7.1(e). The WDS conducted over 15 pieces of hexagonal crystals from several CVT batches finds an elemental ratio of $Mn_{0.94(3)}Bi_{2.09(7)}Te_4$ with no significant batch-to-batch variation. There is piece-to-piece variation. We note that pieces with six well-defined edges as shown in the inset of Fig. 7.1(e) in general have higher Mn concentrations than those with one as-grown edge. The highest Mn ratio is up to 0.98. In comparison, the elemental analysis on our flux-grown crystals finds $Mn_{0.90(1)}Bi_{2.08(5)}Te_4$. This suggests an overall enhancement of Mn concentration, and motivates us to look into its impact on the physical properties.

7.3 Physical properties

The effect of higher Mn concentrations in CVT samples can be reflected in the bulk magnetic and transport measurements. The results in Fig. 7.2 are measured on and compared between a CVT-grown sample (CVT-S1) with $Mn_{0.95(1)}Bi_{2.09(1)}Te_4$ and a flux-grown sample (flux-S1) with $Mn_{0.90(1)}Bi_{2.11(2)}Te_4$, each characterized with WDS. Figures. 7.2 (a) and (b)

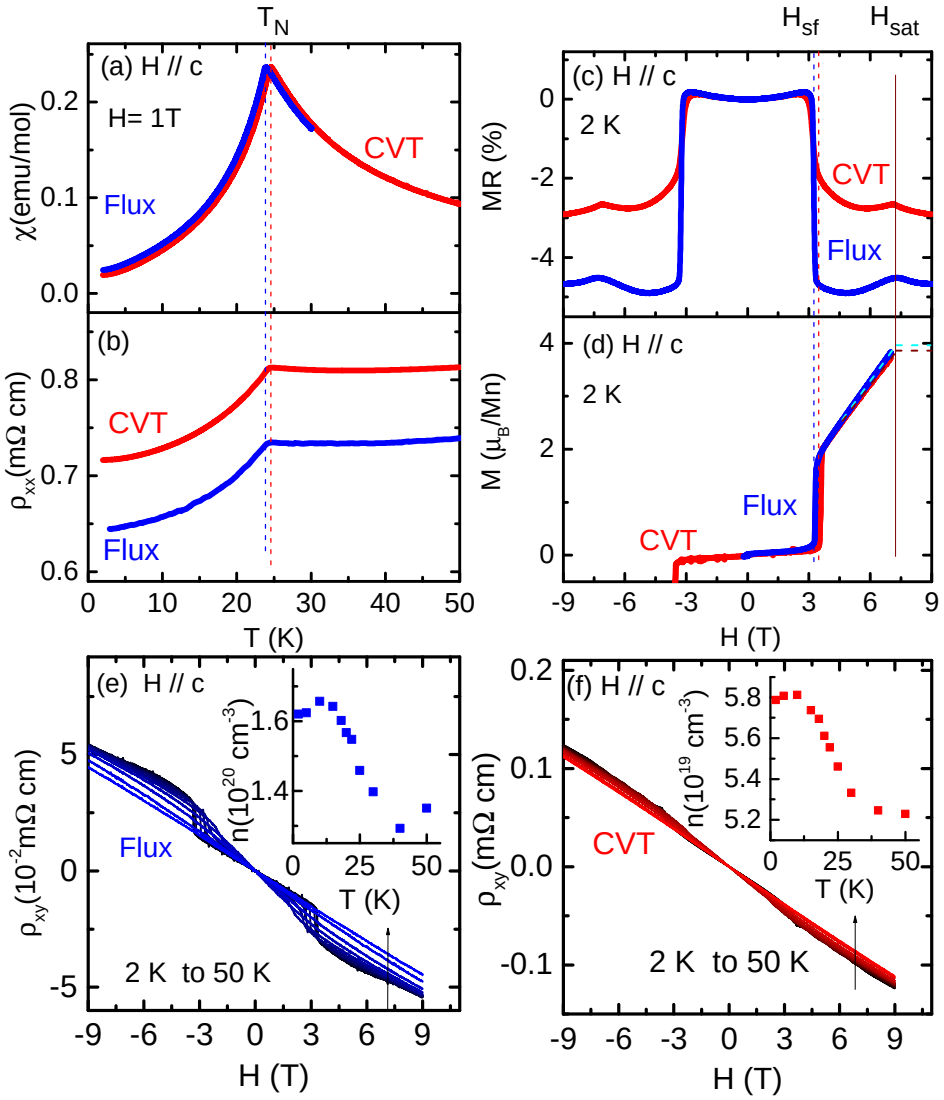

Figure 7.2: Comparison of the CVT-S1 and flux-S1 samples. (a-b) Temperature-dependent magnetic susceptibility measured along $H_{//c} = 1$ T and longitudinal resistivity ρ_{xx} measured in the *ab* plane. (c-d) Field-dependent MR and the magnetization with marked spin-flop transition field and saturation field measured at 2K. (e-f) Hall resistivity ρ_{xy} measured from 2 K to 50 K for the two samples. Inset: Extracted carrier density from the slope of $\rho_{xy}(H)$ in the polarized FM phase at each temperature.

show the temperature-dependent susceptibility $\chi_{H\|c}$ and resistivity ρ_{xx} ($I//ab$). The AFM transition appears as a sharp kink in $\chi_{H\|c}$(T) in both panels, which is found to be 24.6 K for CVT-S1 and 23.8 K for flux-S1. The drop of ρ_{xx} under T_N is consistent with the reduced spin-disorder scattering due to the formation of the in-plane ferromagnetic (FM) order.

The magnetism of $MnBi_2Te_4$ couples strongly with the charge carriers. The comparison of the magnetoresistance (MR), magnetization under field at 2K, as well as Hall resistivity from 2 to 50 K between the two samples is included in Figs. 7.2 (c)-(f). In Fig. 7.2(d), the magnetization per Mn is calculated based on the Mn concentration obtained from WDS. At 3.3 T for flux-S1, a feature from the spin-flop transition shows up across all panels. The MR drops sharply with the sharp increase of the magnetic magnetization. In comparison, the CVT-S1 sample shows the same feature at 3.5 T. Then at 7.7 T, a feature due to the magnetic saturation is seen as a peak in MR and a subtle kink in Hall resistivity for both samples in Figs. 7.2 (c) (e) (f). Using the slope of Hall resistivity in the polarized FM phase, we calculate the electron-type carrier density at 2 K to be 5.79×10^{19} cm^{-3} and 1.62×10^{20} cm^{-3} for the CVT-S1 and flux-S1 sample at 2 K. The same calculation is carried out for each temperature. The temperature dependent carrier density is plotted in the insets of Fig. 7.2(e) and (f).

The magnetization data provides valuable insights on the distribution of Mn occupancy [100, 139]. Bi substitutions of Mn on the Mn site as well as a very small amount of Mn_{Bi} antisites exist in $MnBi_2Te_4$. We denote the Mn atoms on the Mn site as Mn1, the Mn atoms on the Bi site as Mn2. Previous studies of the sample grown by the flux method [139] show that below 20 T, the Mn2 sublattice, aligns antiferromagnetically with the Mn1 sublattice. Therefore at H_{sat}, each Mn1 and Mn2 spins enter into its individual polarized FM state while these two sublattices are AFM to each other. Ref. [139] also shows at 50 T, Mn1 and Mn2 spins become parallel to each other. Therefore, the higher the Mn2-to-Mn1 ratio, the smaller the magnetic moment will be near 8 T since Mn1 and Mn2 are AFM to each other at 8 T. Considering the M(H) curve is linear between H_{sf} and H_{sat}, we can estimate the moment at H_{sat}. The values are found to be 3.86 μ_B/Mn for CVT-S1 and 3.94 μ_B/Mn for

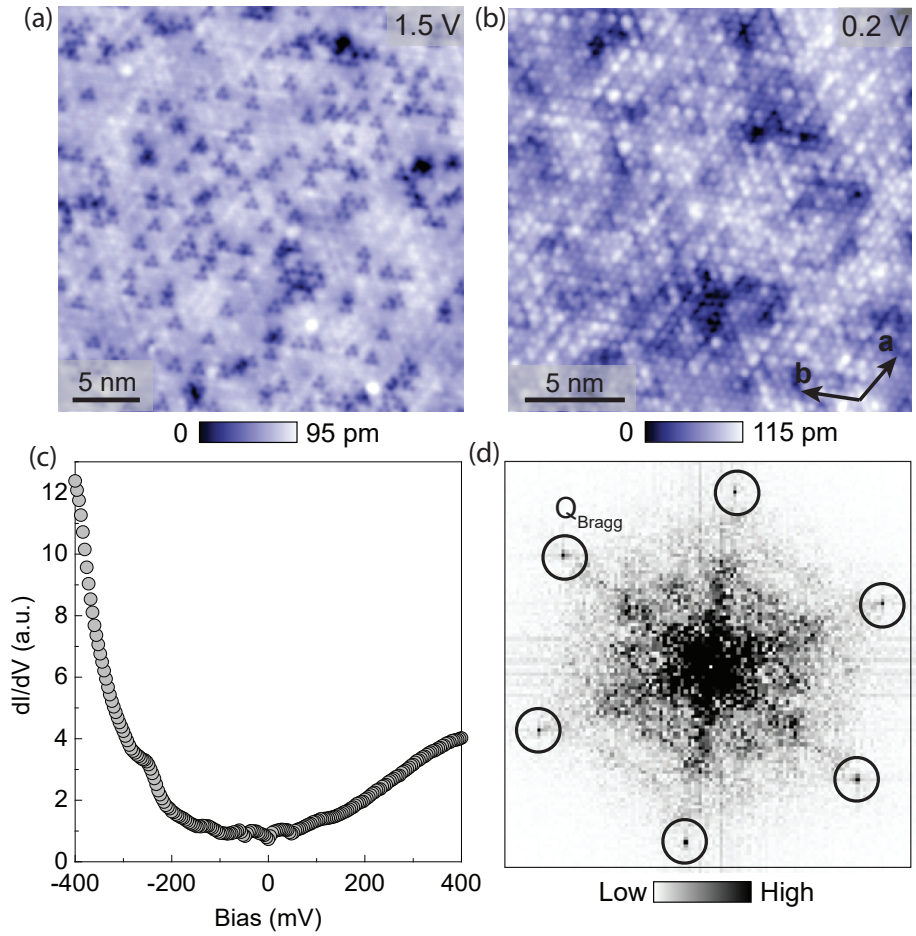

Figure 7.3: Scanning tunneling microscopy and spectroscopy of CVT-grown $MnBi_2Te_4$. (a) Large-scale STM topograph showing a large, flat surface obtained by the cleaving process. Dark triangular features in the topograph represent Mn substitutions at the Bi site [138]. (b) Zoom-in on a smaller region showing the expected hexagonal atomic structure. (c) Average dI/dV spectrum. (d) Fourier transform of the topograph in (b), with the atomic Bragg peaks denoted by black circles. STM setup condition: (a)1.5 V/1.5 nA ; (b) 200 mV/200 pA; (c) 400 mV/300 pA (4 mV bias excitation). All data is acquired at 4.5 K.

flux-S1. We can then further quantitatively estimate the occupancy of Mn1 and Mn2 using

$$m_1 + 2m_2 = \mathrm{Mn_{WDS}} \tag{7.1}$$

$$\frac{m_1 - 2m_2}{m_1 + 2m_2} = \frac{M_{8\mathrm{T}}}{M_{50\mathrm{T}}} \tag{7.2}$$

Here m_1 and m_2 are the occupancy of Mn1 and Mn2, respectively. $\mathrm{Mn_{WDS}}$ is the Mn concentration obtained from WDS. $M_{8\mathrm{T}}$ is the initial magnetization value estimated from the $M - H$ curve at 8 T. $M_{50\mathrm{T}}$ is the final magnetization value when Mn2 are also polarized to align in parallel with Mn1, which is suggested to be $4.6\mu_B$/Mn [139] based on the measurement up to 50 T. Based on these, m_1 and m_2 are found to be 0.835 and 0.032 for flux-S1, and 0.874 and 0.038 for CVT-S1.

To observe the distribution of the defects and their effects on the electronic structure, STM was performed on a CVT-grown $MnBi_2Te_4$. The CVT-grown single crystals were cleaved at room temperature at the pressure of 1×10^{-10} Torr and were immediately inserted into the STM head. Typical STM topographs show a flat surface with a hexagonal atomic structure (Fig. 7.3(a,b,d)), consistent with the expected $MnBi_2Te_4$ topmost surface layer composed of Te atoms. Dark triangular features in the high-bias STM topograph in Fig. 7.3(a) can be identified as Mn substitutions at the Bi site [138]. By manual counting of individual defects observed in the topograph, we calculate the density of these substitutions in our CVT samples to be around 3.5%. The antisite concentration is up from 3% in the STM of the flux-grown sample [62], suggesting a similar trend we found from our magnetization data. Lattice constant extracted from the Fourier transform (FT) of the topograph (Fig. 7.3(d)) is about 4.49 Å. Average dI/dV spectra show a sharp upturn in conductance at around -200 mV in Fig. 7.3(c). We note that this spectral feature is about 300 meV closer to the Fermi level compared to the spectra obtained in previous work [62, 135], which may indicate a lower level of self-doping in our samples.

The effect of defects and charge carriers on the band structure can be seen more clearly with ARPES. The measurements were made on three different CVT-samples. CVT-S2 has

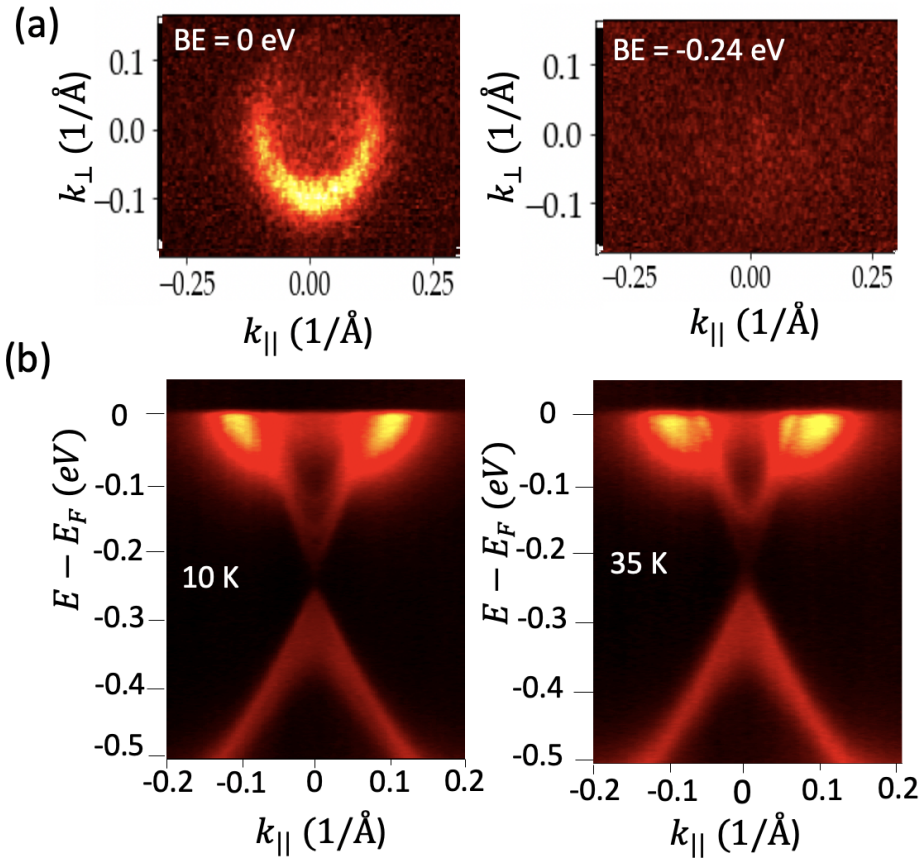

Figure 7.4: ARPES band maps and spectra on $MnBi_2Te_4$ sample CVT-S2. (a) ARPES intensity maps taken at E_f and the Dirac point at -0.24 eV binding energy. (b) ARPES spectra taken at 10 K and 35 K on the Γ to K cut, showing the TSS as well as a splitting of the bulk conduction band. ARPES data was taken with 26 eV, and the energy of the Dirac point is -0.24 eV, determined by finding the minimum of the energy distribution curve at Γ.

6 as-grown edges while CVT-S3 and CVT-S4 have only one as-grown edge. The topological surface state (TSS), along with bulk conduction and valence bands were observed. Figure 7.4 summarizes the ARPES data taken on CVT-S2. Figure 7.4(a) shows ARPES intensity maps at the Fermi energy, and at the Dirac point (DP) at -0.24 eV binding energy, respectively. Figure 7.4(b) shows the band structure of CVT-S2 cutting from the Γ point to K point in the Brillouin zone above and below the Néel temperature near 24 K. A splitting of the bulk conduction band is clearly observed below the Néel temperature in the 26-eV spectra, similar to previous reports on samples grown by the flux method or stoichiometric melting [68, 140]. The energies of the Dirac point can be estimated as the minimum of the energy distribution curve at the Γ point. It is -0.24 eV for CVT-S2, -0.26 eV for CVT-S3, and -0.275 eV for CVT-S4. This variation in energy is consistent with what we have learned from our WDS measurements, that is, the well-shaped CVT crystals have higher Mn concentrations. In previous measurements on flux-grown samples, the DP energy ranges from -0.275 eV to -0.28 eV binding energy [66, 69, 141], and samples grown with stoichiometric melting have DP energies at -0.27 and -0.275 eV binding energy [68, 140]. Therefore, compared to flux-grown samples, the CVT-grown samples are in general more intrinsic. Especially, for the hexagonal-shaped CVT-2, the DP is around 35 meV lower and closer to the TSS. This is again consistent with the lower carrier concentration extracted from the Hall resistivity.

7.4 Chern insulator state in 2D limit

To investigate the transport properties of the CVT-grown samples in the 2D limit, we exfoliated the $MnBi_2Te_4$ samples down to the atomically thin regime and fabricated 2D quantum devices. Figures 7.5 (a)-(c) show representative data of a 6-SL device made of a CVT grown $MnBi_2Te_4$ crystal. In the AFM phase ($H = 0$), our transport measurement (Fig. 7.5 (a)) shows a clear insulating behavior with the resistance reaching over 10^6 Ohms. This agrees with the theoretical expectation that the 6-SL AFM $MnBi_2Te_4$ is an Axion insulator with zero Chern number. Notably, as shown in Fig. 7.5 (a), the gate voltage that corresponds to the charge neutrality in the CVT-device is very close to V_{BG}=0 V. This

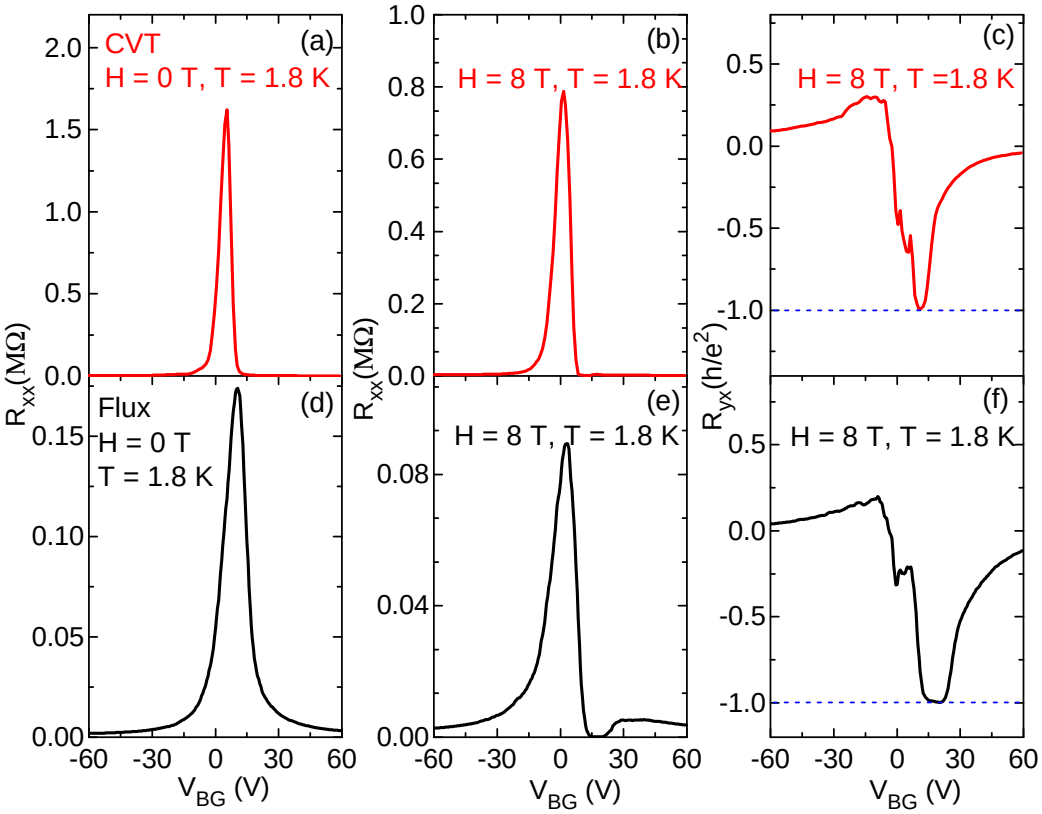

Figure 7.5: Observation of Chern insulator state in CVT and flux grown $MnBi_2Te_4$. All data are taken at 1.8 K. For the CVT-device and flux-device respectively: (a)(d) gate-voltage-dependent longitudinal resistance R_{xx} in the AFM state at zero field. At the gated charge neutrality point, R_{xx}(T) in (a) is 10 times of that in (d) with a much sharper response to the gating voltage, suggesting better quality of the device. (b)(e) gate-voltage-dependent longitudinal resistance R_{xx} in the FM state at 8 T, with marked reduction of resistance near the charge neutrality point. (c)(f) gate-voltage-dependent Hall resistance R_{yx} in the FM state at 8 T, with marked quantized value of $-\frac{h}{e^2}$ near the charge neutrality point.

indicates that natural doping in this 6-SL $MnBi_2Te_4$ device is small, consistent with the reduced carrier density that we obtained from the bulk transport measurements. Based on the field effect model, we estimate a carrier mobility of ~ 2500 cm^2/V·s, which is the highest that has ever been reported. In the FM phase (H=8 T), our transport data reveal a fully vanishing longitudinal resistance R_{xx} and fully quantized Hall resistance, which demonstrate the topological Chern insulator state, consistent with previous studies [54, 55].

7.5 Discussion

WDS reveals higher amount of Mn concentration in CVT-S1 than that in flux-S1. Meanwhile from the analysis of the M(H) data, the concentrations of Mn1 and Mn2 sublattices, that is m_1 and m_2, are 0.835 and 0.032 for flux-S1, and 0.874 and 0.038 for CVT-S1, respectively. Ideally, $MnBi_2Te_4$ crystals with more Mn atoms going into the dominant Mn site (higher m_1) and less Mn atoms occupying the Bi site (lower m_2) will have better magnetic homogeneity and thus be more promising for the realization of QAHE, etc. However, our experiments indicate that the higher the total Mn concentrations we pushed in by optimizing the growth condition and method, the higher the m_1 and m_2 though m_2 increases much slower than m_1. Therefore, there is no way that $MnBi_2Te_4$ crystals with simultaneously higher Mn1 concentration and lower Mn_{Bi} can be made. If so, when screening samples for the device fabrication, will the samples with total higher Mn concentration be more ready to show quantized Hall conductance in devices? To answer this question, we compare the 6-SL device using the CVT-grown $MnBi_2Te_4$ crystal with a 6-SL device using a flux-grown $MnBi_2Te_4$ crystal. As shown in Fig. 7.5, the two devices show qualitatively similar behaviors, i.e., an insulating behavior in the AFM phase and a topological Chern insulator behavior with quantized Hall response in the FM phase. However, one can clearly see that the resistance peak is much sharper and higher for the CVT-device as a result of the larger carrier mobility. Based on the field effect model, carrier mobility of the flux-device is found ~ 800 cm^2/V·s, which is around one third of the CVT one. We further note that the Chern insulator behavior appears in a narrower range of gate voltage in the CVT-device. This may

be related to the larger amount of antisite disorder present in the CVT-crystal. Despite this, the CVT-devices have a higher success rate in realizing the Chern insulator state with the same carefully-controlled fabrication process. We realized Chern insulator state in 6 out of 18 flux samples and 4 out of 5 CVT samples. The success rate of the device made from CVT-samples is more than twice as large as that of flux sample, which is likely to be attributed to the high Mn1 concentration that gives higher magnetic homogeneity. Therefore, the higher the m_1, the higher the success rate in realizing the Chern insulator state; the higher the m_2, the narrower the gate voltage window the Chern insulator state will appear.

The fact that both m_1 and m_2 are higher in CVT-S1 also explains why the magnetic transition temperature of CVT-S1 is higher. The higher Mn occupancy can also be associated with the reduced carrier concentration in the CVT-S1, since Bi atoms on Mn site is an electron-donor and makes the sample more n-type, while Mn on Bi site is an electron-acceptor [142] which makes the sample more p-type. Compared to the flux-S1 sample, the Mn1 occupancy of the CVT-S1 sample increases by 0.039 while the Mn2 occupancy only increases by 0.006. This decreases the number of electron-donors and increases the number of electron-acceptors, thus making the sample less n-doped. Indeed, the low carrier concentration is universal in CVT single crystals. At 2 K, the carrier concentrations from 15 measured pieces from different batches range from 2.7-10 $\times 10^{19}$ cm^{-3} with an average of 5.8 $\times 10^{19}$ cm^{-3}. The values from 5 measured pieces from different flux batch range in 1.3-2.0 $\times 10^{20}$ cm^{-3} with an average of 1.6$\times 10^{20}$ cm^{-3}.

7.6 Summary and outlooks

In summary, compared with the flux-grown $MnBi_2Te_4$ single crystals, the CVT-grown ones have less Bi substitution on the Mn site and slightly more Mn_{Bi} antisites, leading to a smaller carrier density and reduced energy difference between the Fermi level and the Dirac point in bulk CVT-sample. Furthermore, when exfoliated into 6-SL device, the CVT samples show by far the highest mobility of 2500 cm^{2}V·s with vanishing R_{xx} and quantized R_{xy} at 8 T. Therefore, our new growth design readily allowed us to achieve the Chern insulator

state in devices with higher quality and high success rate. This paves a new way to optimize crystal growth of $MnBi_2Te_4$ and related $MnBi_{2n}Te_{3n+1}$ ($n \geq 2$) to investigate the emergent phenomena arising from the interplay of topology and the magnetism. Future optimization such as varying the Mn concentration in the source end, using other transport agents such as TeI_4, etc. can be explored to further improve the sample quality.

CHAPTER 8

Conclusion

In this dissertation, I presented our studies on the $MnBi_{2n}Te_{3n+1}$ (MBT) family in different aspects including design, growth, characterization, magnetism, topology, defect chemistry, and magnetic dynamics. Our proposed material design of inserting $[Bi_2Te_3]$ spacer layer between the magnetic $[MnBi_2Te_4]$ layers was realized with the successful single crystal growths of natural heterostructures $MnBi_{2n}Te_{3n+1}$. The subsequent characterization, physical property measurement and our collaborations with other groups show that the $n = 2, 3$ numbers are intrinsic Z_2 AFM TIs with very weak interlayer magnetic coupling. We further demonstrated that the $n = 4$ member is the first intrinsic FM axion insulator ever discovered. Therefore, as the interlayer coupling decreases with increasing n and increasing interlayer Mn-Mn distance, the magnetism and band topology in MBT can be tuned from AFM TI to FM axion insulator, suggesting the close competition between AFM and FM inside this family. Then our study of the Sb-doped $MnBi_4Te_7$ single crystals provides a material series whose magnetism can be tuned in a controllable and continuous manner from AFM to FM and then to ferrimagnetic. We attribute such an evolution of magnetism to the increasing amount of the $Mn_{Bi,\,Sb}$ antisites arising from the Sb doping. The antisites mediate an additional effectively-FM exchange path that is temperature and defect-density dependent, leading to the competition with the original AFM interlayer superexchange interaction and thus the observed evolution of magnetism. We close our investigation of the magnetism in MBT by discussing the magnetic dynamics in FM MBTs. It is found that the van der Waals magnetism with strong FM intraplanar coupling and vanishing interplanar coupling host unique domain formation that gives rise to the exotic magnetic relaxation behavior. Last but not least, we have developed a new way to grow $MnBi_2Te_4$ via chemical vapor transport

(CVT) and have optimized the recipe to enhance the crystal size and yield. The comparison between the crystals grown by the CVT methods and flux methods in defects, magnetism and device quality indeed suggests that our new growth design readily allowed us to achieve the quantized Hall conductance in devices with higher quality and success rate.

From their magnetic and topological properties, we have seen the $MnBi_{2n}Te_{3n+1}$ family are great candidates for QAHE and can host many interesting magnetic topological states such as FM axion insulator, type-I magnetic Weyl semimetal, etc. Up to the time of this writing, however, there has only been one report of zero-field QAHE in $MnBi_2Te_4$ [54]. This could come from different fabrication environment in which bulk crystals are exfoliated and made into a device, or something intrinsic to the crystals like Mn deficiencies and Mn_{Bi} antisites. To consistently achieve high-temperature realization of quantum anomalous Hall effect in MBT family, optimizations of both 2D device fabrication and 3D bulk material are needed. For the former aspect, the side effect of each fabrication step especially on the exfoliated surface needs to be investigated. On the material side, although $MnBi_{2n}Te_{3n+1}$ host intrinsic magnetism, antisite defects and Mn deficiencies are prevalent in the crystals. Given these understandings, it is desired in the future work to optimize the growth of 3D MBT crystals to lower the Mn deficiency and antisites. New material discoveries based on the $[MnBi_2Te_4]$ and other building blocks are also urged to bring breakthroughs.

Appendix A

Additional Method for structural, magnetic and topological property measurement

A.1 Method for Band structure calculation and measurement

A.1.1 DFT

We computed the electronic structures using the projector augmented wave method [143, 144] as implemented in the VASP package [145] within the generalized gradient approximation schemes (GGA) [146] and GGA plus Hubbard U (GGA + U) [147] scheme. On-site $U = 5.0$ eV was used for Mn d orbitals. A 11×11×5 MonkhorstPack k-point mesh was used in the computations. The spin-orbit coupling effects were included in calculations. The experimental lattice parameters were used. The atomic positions were relaxed until the residual forces were less than 0.01 eV/Å. We used Mn d orbitals, Bi p orbitals, Sb p orbitals, and Te p orbitals to construct Wannier functions, without performing the procedure for maximizing localization [148].

A.1.2 ARPES

We have seen DFT as a powerful way to obtain the band structure of the material and thereby the topological number. Experimentally, electronic band structures can be directly probed by angle-resolved photoelectronic spectroscopy. A beam of photon with known energy E_i and momentum k_i vector is shined on a cleaved surface of a crystal. The distribution of energy E_f and moment k_f of the excited electrons are measured. By comparing the input

and the output, one can reconstruct the energy and moment of the electron before excitation. Therefore one can get from ARPES the electron distribution in the reciprocal space, i.e. the band structure.

For many topological materials such as Dirac semimetals, Weyl semimetals , one key feature is the linear dispersion. This can be directly seen by ARPES. ARPES can be used to distinguish their surface state from the bulk states. For example, with topological insulators like Bi2Se3, ARPES can clearly shows the gap opening by SOC. For our studies, ARPES usually goes in hand with DFT, so the calculation with topological numbers are done in a valid band structure.

ARPES measurements were carried out at the Advanced Light Source (ALS) endstation 7.0.2.1, and Stanford Synchrotron Research Laboratory (SSRL) beam-lines 5-2 and 5-4. Data was taken with photon energies of 26 eV with linear horizontal polarization. Samples were cleaved *in situ* and measured under ultrahigh vacuum below 3 $\times 10^{-11}$ Torr at SSRL 5-4, 4 $\times 10^{-11}$ Torr at SSRL 5-2, and 2 $\times 10^{-11}$ Torr at ALS. Data was collected with Scienta R4000, DA30 L, and R4000 analyzers at SSRL 5-4, SSRL 5-2 and ALS, respectively.

A.2 Method for scanning probe and imaging

A.2.1 Scanning tunnelling microscopy

Scanning tunneling microscopy (STM) data was acquired using a customized Unisoku USM1300 microscope. Single crystals were cleaved at room temperature in ultra-high vacuum (UHV) pressure of about 1×10^{-10} Torr and immediately inserted into the STM chamber where they were kept at 4.5 K during the measurements. Spectroscopic measurements were made using a standard lock-in technique with 915 Hz frequency and bias excitation as detailed in figure captions. STM tips used were home-made chemically-etched tungsten tips, annealed in UHV to bright orange color before being used for imaging.

A.2.2 Magneto-optical Kerr imaging

Direct magneto-optical Kerr imaging was performed using a helium flow-type cryostat with temperature down to 5 K and the ability to apply a 1kOe - range magnetic field. Optical imaging in linearly polarized light was done using a Leica DMLM polarized microscope equipped with the high quality polarizer and analyzer. In the experiment, the sample is positioned on top of a gold-plated copper stage with its flat surface perpendicular to the direction of light propagation. The light polarization direction, also perpendicular to the light propagation direction (thus parallel to the sample surface that is being imaged), was controlled by a polarizer and could be changed with respect to the stationary sample for optimal contrast. Upon reflection off the sample, polarization direction rotates by the angle proportional to the surface magnetization (magneto-optical polar Kerr effect). Due to chirality of the problem, opposite magnetic moments lead to the opposite directions of the polarization rotation. When viewed through an analyzer rotated almost perpendicular to the polarizer, a 2D image of the magnetic pattern emerges. The appearance can be switched at will by adjusting the polarizer/analyzer pair and we chose to show domains along the direction of the applied field to be dark, whereas opposite domains are white and not magnetized state is neutral-gray. In this setting, the maximum contrast between the domains is achieved. More detailed discussion of magneto-optical techniques can be found elsewhere [129].

Appendix B

Structural Refinement from $MnBi_{2n}Te_{3n+1}$ single crystals

Table B.1: Refined structural parameters for $MnBi_4Te_7$ at room temperature based on the powder X-ray diffraction data. [50]

Atom	Site	x	y	z	B
Mn	1b	0	0	0.5	0.8
Bi1	2d	0.3333	0.6667	0.0866(4)	0.8
Bi2	2d	0.3333	0.6667	0.3407(4)	0.8
Te1	1a	0	0	0	0.8
Te2	2d	0.6667	0.3333	0.1546(7)	0.8
Te3	2c	0	0	0.2671(7)	0.8
Te4	2d	0.6667	0.3333	0.4355(6)	0.8

Table B.2: Refined structural parameters for $MnBi_6Te_{10}$ at room temperature based on the powder X-ray diffraction data. [80]

Atom	Site	x	y	z	B
Mn1	3a	0	0	0	0.8
Bi1	6c	0	0	0.2357(1)	0.8
Bi2	6c	0	0	0.2953(1)	0.8
Bi3	6c	0	0	0.4704(1)	0.8
Te1	6c	0	0	0.0535(2)	0.8
Te2	6c	0	0	0.1154(2)	0.8
Te3	6c	0	0	0.1790(2)	0.8
Te4	6c	0	0	0.3490(2)	0.8
Te5	6c	0	0	0.4133(2)	0.8

Table B.3: Refined structural parameters for $MnBi_8Te_{13}$ at room temperature based on the powder X-ray diffraction data. [80]

Atom	Site	x	y	z	B
Mn1	3a	0	0	0	0.8
Bi1	6c	0	0	0.18221(4)	0.31(7)
Bi2	6c	0	0	0.22824(5)	0.31(7)
Bi3	6c	0	0	0.36168(5)	0.31(7)
Bi4	6c	0	0	0.40865(6)	0.31(7)
Te1	6c	0	0	0.04172(8)	1.6(1)
Te2	6c	0	0	0.0897(1)	1.6(1)
Te3	6c	0	0	0.13757(8)	1.6(1)
Te4	6c	0	0	0.2707(1)	1.6(1)
Te5	6c	0	0	0.32131(7)	1.6(1)
Te6	6c	0	0	0.4524(1)	1.6(1)
Te7	3b	0	0	0.5	1.6(1)

Bibliography

[1] M. Z. Hasan and C. L. Kane, "Colloquium: topological insulators," *Reviews of modern physics*, vol. 82, no. 4, p. 3045, 2010.

[2] R. S. Mong, A. M. Essin, and J. E. Moore, "Antiferromagnetic topological insulators," *Physical Review B*, vol. 81, no. 24, p. 245209, 2010.

[3] Y. Tokura, K. Yasuda, and A. Tsukazaki, "Magnetic topological insulators," *Nature Reviews Physics*, vol. 1, no. 2, pp. 126–143, 2019.

[4] C.-Z. Chang and M. Li, "Quantum anomalous hall effect in time-reversal-symmetry breaking topological insulators," *Journal of Physics: Condensed Matter*, vol. 28, no. 12, p. 123002, 2016.

[5] Y. Chen, J. G. Analytis, J.-H. Chu, Z. Liu, S.-K. Mo, X.-L. Qi, H. Zhang, D. Lu, X. Dai, Z. Fang, *et al.*, "Experimental realization of a three-dimensional topological insulator, bi2te3," *science*, vol. 325, no. 5937, pp. 178–181, 2009.

[6] N. Nagaosa, J. Sinova, S. Onoda, A. H. MacDonald, and N. P. Ong, "Anomalous hall effect," *Reviews of modern physics*, vol. 82, no. 2, p. 1539, 2010.

[7] M. I. D'Yakonov and V. Perel, "Possibility of orienting electron spins with current," *Soviet Journal of Experimental and Theoretical Physics Letters*, vol. 13, p. 467, 1971.

[8] S. Murakami, N. Nagaosa, and S.-C. Zhang, "Dissipationless quantum spin current at room temperature," *Science*, vol. 301, no. 5638, pp. 1348–1351, 2003.

[9] J. Sinova, D. Culcer, Q. Niu, N. Sinitsyn, T. Jungwirth, and A. H. MacDonald, "Universal intrinsic spin hall effect," *Physical review letters*, vol. 92, no. 12, p. 126603, 2004.

[10] Y. K. Kato, R. C. Myers, A. C. Gossard, and D. D. Awschalom, "Observation of the spin hall effect in semiconductors," *science*, vol. 306, no. 5703, pp. 1910–1913, 2004.

[11] "Quantum hall effect."

[12] "Quantum hall effect: edge states."

[13] T. Ando, Y. Matsumoto, and Y. Uemura, "Theory of hall effect in a two-dimensional electron system," *Journal of the Physical Society of Japan*, vol. 39, no. 2, pp. 279–288, 1975.

[14] K. v. Klitzing, G. Dorda, and M. Pepper, "New method for high-accuracy determination of the fine-structure constant based on quantized hall resistance," *Physical review letters*, vol. 45, no. 6, p. 494, 1980.

[15] C. Day, "Quantum spin hall effect shows up in a quantum well insulator, just as predicted," *Physics Today*, vol. 61, no. 1, p. 19, 2008.

[16] C. L. Kane and E. J. Mele, "Quantum spin hall effect in graphene," *Physical review letters*, vol. 95, no. 22, p. 226801, 2005.

[17] B. A. Bernevig and S.-C. Zhang, "Quantum spin hall effect," *Physical review letters*, vol. 96, no. 10, p. 106802, 2006.

[18] X.-L. Qi and S.-C. Zhang, "The quantum spin hall effect and topological insulators," *arXiv preprint arXiv:1001.1602*, 2010.

[19] M. Konig, S. Wiedmann, C. Brune, A. Roth, H. Buhmann, L. W. Molenkamp, X.-L. Qi, and S.-C. Zhang, "Quantum spin hall insulator state in hgte quantum wells," *Science*, vol. 318, no. 5851, pp. 766–770, 2007.

[20] H. Zhang, C.-X. Liu, X.-L. Qi, X. Dai, Z. Fang, and S.-C. Zhang, "Topological insulators in bi2se3, bi2te3 and sb2te3 with a single dirac cone on the surface," *Nature physics*, vol. 5, no. 6, pp. 438–442, 2009.

[21] F. D. M. Haldane, "Model for a quantum hall effect without landau levels: Condensed-matter realization of the" parity anomaly"," *Physical review letters*, vol. 61, no. 18, p. 2015, 1988.

[22] C.-Z. Chang, J. Zhang, X. Feng, J. Shen, Z. Zhang, M. Guo, K. Li, Y. Ou, P. Wei, L.-L. Wang, *et al.*, "Experimental observation of the quantum anomalous hall effect in a magnetic topological insulator," *Science*, vol. 340, no. 6129, pp. 167–170, 2013.

[23] C. Nayak, S. H. Simon, A. Stern, M. Freedman, and S. D. Sarma, "Non-abelian anyons and topological quantum computation," *Reviews of Modern Physics*, vol. 80, no. 3, p. 1083, 2008.

[24] X.-L. Qi, T. L. Hughes, and S.-C. Zhang, "Topological field theory of time-reversal invariant insulators," *Physical Review B*, vol. 78, no. 19, p. 195424, 2008.

[25] L. Fu and C. L. Kane, "Superconducting proximity effect and majorana fermions at the surface of a topological insulator," *Physical review letters*, vol. 100, no. 9, p. 096407, 2008.

[26] B. Jäck, Y. Xie, J. Li, S. Jeon, B. A. Bernevig, and A. Yazdani, "Observation of a majorana zero mode in a topologically protected edge channel," *Science*, vol. 364, no. 6447, pp. 1255–1259, 2019.

[27] J. Alicea, "New directions in the pursuit of majorana fermions in solid state systems," *Reports on progress in physics*, vol. 75, no. 7, p. 076501, 2012.

[28] L. Fu and C. L. Kane, "Probing neutral majorana fermion edge modes with charge transport," *Physical review letters*, vol. 102, no. 21, p. 216403, 2009.

[29] A. Akhmerov, J. Nilsson, and C. Beenakker, "Electrically detected interferometry of majorana fermions in a topological insulator," *Physical review letters*, vol. 102, no. 21, p. 216404, 2009.

[30] X.-L. Qi, T. L. Hughes, and S.-C. Zhang, "Chiral topological superconductor from the quantum hall state," *Physical Review B*, vol. 82, no. 18, p. 184516, 2010.

[31] J. Alicea and P. Fendley, "Topological phases with parafermions: theory and blueprints," *Annual Review of Condensed Matter Physics*, vol. 7, pp. 119–139, 2016.

[32] F. Wilczek, "Two applications of axion electrodynamics," *Physical review letters*, vol. 58, no. 18, p. 1799, 1987.

[33] F. Wilczek, "A theoretical physicist examines exotic particles lurking in new materials," *Nature*, vol. 458, p. 129, 2009.

[34] N. Varnava and D. Vanderbilt, "Surfaces of axion insulators," *Physical Review B*, vol. 98, no. 24, p. 245117, 2018.

[35] N. P. Armitage and L. Wu, "On the matter of topological insulators as magnetoelectrics," *SciPost Physics*, vol. 6, no. 4, p. 046, 2019.

[36] Y. Xu, Z. Song, Z. Wang, H. Weng, and X. Dai, "Higher-order topology of the axion insulator euin 2 as 2," *Physical review letters*, vol. 122, no. 25, p. 256402, 2019.

[37] C. Yue, Y. Xu, Z. Song, H. Weng, Y.-M. Lu, C. Fang, and X. Dai, "Symmetry-enforced chiral hinge states and surface quantum anomalous hall effect in the magnetic axion insulator bi2–xsmxse3," *Nature Physics*, vol. 15, no. 6, pp. 577–581, 2019.

[38] M. Gu, J. Li, H. Sun, Y. Zhao, C. Liu, J. Liu, H. Lu, and Q. Liu, "Spectral signatures of the surface anomalous hall effect in magnetic axion insulators," *Nature communications*, vol. 12, no. 1, pp. 1–9, 2021.

[39] N. J. Ghimire, A. Botana, J. Jiang, J. Zhang, Y.-S. Chen, and J. Mitchell, "Large anomalous hall effect in the chiral-lattice antiferromagnet conb3s6," *Nature communications*, vol. 9, no. 1, pp. 1–6, 2018.

[40] L. Šmejkal, R. González-Hernández, T. Jungwirth, and J. Sinova, "Crystal time-reversal symmetry breaking and spontaneous hall effect in collinear antiferromagnets," *Science advances*, vol. 6, no. 23, p. eaaz8809, 2020.

[41] H. Chen, Q. Niu, and A. H. MacDonald, "Anomalous hall effect arising from noncollinear antiferromagnetism," *Physical review letters*, vol. 112, no. 1, p. 017205, 2014.

[42] D. Sheng, Z. Weng, L. Sheng, and F. Haldane, "Quantum spin-hall effect and topologically invariant chern numbers," *Physical review letters*, vol. 97, no. 3, p. 036808, 2006.

[43] C. L. Kane and E. J. Mele, "Z 2 topological order and the quantum spin hall effect," *Physical review letters*, vol. 95, no. 14, p. 146802, 2005.

[44] L. Fu and C. L. Kane, "Time reversal polarization and a z 2 adiabatic spin pump," *Physical Review B*, vol. 74, no. 19, p. 195312, 2006.

[45] L. Fu and C. L. Kane, "Topological insulators with inversion symmetry," *Physical Review B*, vol. 76, no. 4, p. 045302, 2007.

[46] A. M. Turner, Y. Zhang, R. S. Mong, and A. Vishwanath, "Quantized response and topology of magnetic insulators with inversion symmetry," *Physical Review B*, vol. 85, no. 16, p. 165120, 2012.

[47] E. C. Stoner and E. Wohlfarth, "A mechanism of magnetic hysteresis in heterogeneous alloys," *Philosophical Transactions of the Royal Society of London. Series A, Mathematical and Physical Sciences*, vol. 240, no. 826, pp. 599–642, 1948.

[48] J. Rodríguez-Carvajal, "Recent advances in magnetic structure determination by neutron powder diffraction," *Physica B: Condensed Matter*, vol. 192, no. 1-2, pp. 55–69, 1993.

[49] B. C. Chakoumakos, H. Cao, F. Ye, A. D. Stoica, M. Popovici, M. Sundaram, W. Zhou, J. S. Hicks, G. W. Lynn, and R. A. Riedel, "Four-circle single-crystal neutron diffractometer at the high flux isotope reactor," *Journal of Applied Crystallography*, vol. 44, no. 3, pp. 655–658, 2011.

[50] C. Hu, K. N. Gordon, P. Liu, J. Liu, X. Zhou, P. Hao, D. Narayan, E. Emmanouilidou, H. Sun, Y. Liu, *et al.*, "A van der waals antiferromagnetic topological insulator with weak interlayer magnetic coupling," *Nature communications*, vol. 11, no. 1, pp. 1–8, 2020.

[51] D. Zhang, M. Shi, T. Zhu, D. Xing, H. Zhang, and J. Wang, "Topological axion states in the magnetic insulator mnbi 2 te 4 with the quantized magnetoelectric effect," *Physical review letters*, vol. 122, no. 20, p. 206401, 2019.

[52] J. Li, Y. Li, S. Du, Z. Wang, B.-L. Gu, S.-C. Zhang, K. He, W. Duan, and Y. Xu, "Intrinsic magnetic topological insulators in van der waals layered mnbi2te4-family materials," *Science Advances*, vol. 5, no. 6, p. eaaw5685, 2019.

[53] M. M. Otrokov, I. I. Klimovskikh, H. Bentmann, D. Estyunin, A. Zeugner, Z. S. Aliev, S. Gaß, A. Wolter, A. Koroleva, A. M. Shikin, *et al.*, "Prediction and observation of an antiferromagnetic topological insulator," *Nature*, vol. 576, no. 7787, pp. 416–422, 2019.

[54] Y. Deng, Y. Yu, M. Z. Shi, Z. Guo, Z. Xu, J. Wang, X. H. Chen, and Y. Zhang, "Quantum anomalous hall effect in intrinsic magnetic topological insulator mnbi2te4," *Science*, vol. 367, no. 6480, pp. 895–900, 2020.

[55] C. Liu, Y. Wang, H. Li, Y. Wu, Y. Li, J. Li, K. He, Y. Xu, J. Zhang, and Y. Wang, "Robust axion insulator and chern insulator phases in a two-dimensional antiferromagnetic topological insulator," *Nature Materials*, vol. 19, no. 5, pp. 522–527, 2020.

[56] K. He, Y. Wang, and Q.-K. Xue, "Topological materials: quantum anomalous hall system," *Annual Review of Condensed Matter Physics*, vol. 9, pp. 329–344, 2018.

[57] C.-X. Liu, S.-C. Zhang, and X.-L. Qi, "The quantum anomalous hall effect: Theory and experiment," *Annual Review of Condensed Matter Physics*, vol. 7, pp. 301–321, 2016.

[58] J. Wang, B. Lian, X.-L. Qi, and S.-C. Zhang, "Quantized topological magnetoelectric effect of the zero-plateau quantum anomalous hall state," *Physical Review B*, vol. 92, no. 8, p. 081107, 2015.

[59] D. S. Lee, T.-H. Kim, C.-H. Park, C.-Y. Chung, Y. S. Lim, W.-S. Seo, and H.-H. Park, "Crystal structure, properties and nanostructuring of a new layered chalcogenide semiconductor, bi 2 mnte 4," *CrystEngComm*, vol. 15, no. 27, pp. 5532–5538, 2013.

[60] Z. S. Aliev, I. R. Amiraslanov, D. I. Nasonova, A. V. Shevelkov, N. A. Abdullayev, Z. A. Jahangirli, E. N. Orujlu, M. M. Otrokov, N. T. Mamedov, M. B. Babanly, *et al.*, "Novel ternary layered manganese bismuth tellurides of the mnte-bi2te3 system: Synthesis and crystal structure," *Journal of Alloys and Compounds*, vol. 789, pp. 443–450, 2019.

[61] Y. Gong, J. Guo, J. Li, K. Zhu, M. Liao, X. Liu, Q. Zhang, L. Gu, L. Tang, X. Feng, *et al.*, "Experimental realization of an intrinsic magnetic topological insulator," *Chinese Physics Letters*, vol. 36, no. 7, p. 076801, 2019.

[62] J.-Q. Yan, Q. Zhang, T. Heitmann, Z. Huang, K. Chen, J.-G. Cheng, W. Wu, D. Vaknin, B. C. Sales, and R. J. McQueeney, "Crystal growth and magnetic structure of mnbi 2 te 4," *Physical Review Materials*, vol. 3, no. 6, p. 064202, 2019.

[63] A. Zeugner, F. Nietschke, A. U. Wolter, S. Gaß, R. C. Vidal, T. R. Peixoto, D. Pohl, C. Damm, A. Lubk, R. Hentrich, *et al.*, "Chemical aspects of the candidate antiferromagnetic topological insulator mnbi2te4," *Chemistry of Materials*, vol. 31, no. 8, pp. 2795–2806, 2019.

[64] M. M. Otrokov, I. P. Rusinov, M. Blanco-Rey, M. Hoffmann, A. Y. Vyazovskaya, S. V. Eremeev, A. Ernst, P. M. Echenique, A. Arnau, and E. V. Chulkov, "Unique thickness-dependent properties of the van der waals interlayer antiferromagnet mnbi 2 te 4 films," *Physical Review Letters*, vol. 122, no. 10, p. 107202, 2019.

[65] B. Chen, F. Fei, D. Zhang, B. Zhang, W. Liu, S. Zhang, P. Wang, B. Wei, Y. Zhang, Z. Zuo, *et al.*, "Intrinsic magnetic topological insulator phases in the sb doped mnbi 2 te 4 bulks and thin flakes," *Nature communications*, vol. 10, no. 1, pp. 1–8, 2019.

[66] Y.-J. Hao, P. Liu, Y. Feng, X.-M. Ma, E. F. Schwier, M. Arita, S. Kumar, C. Hu, M. Zeng, Y. Wang, *et al.*, "Gapless surface dirac cone in antiferromagnetic topological insulator mnbi 2 te 4," *Physical Review X*, vol. 9, no. 4, p. 041038, 2019.

[67] J. Ge, Y. Liu, J. Li, H. Li, T. Luo, Y. Wu, Y. Xu, and J. Wang, "High-chern-number and high-temperature quantum hall effect without landau levels," *National Science Review*, vol. 7, no. 8, pp. 1280–1287, 2020.

[68] Y. Chen, L. Xu, J. Li, Y. Li, H. Wang, C. Zhang, H. Li, Y. Wu, A. Liang, C. Chen, *et al.*, "Topological electronic structure and its temperature evolution in antiferromagnetic topological insulator mnbi 2 te 4," *Physical Review X*, vol. 9, no. 4, p. 041040, 2019.

[69] H. Li, S.-Y. Gao, S.-F. Duan, Y.-F. Xu, K.-J. Zhu, S.-J. Tian, J.-C. Gao, W.-H. Fan, Z.-C. Rao, J.-R. Huang, *et al.*, "Dirac surface states in intrinsic magnetic topological insulators eusn 2 as 2 and mnbi 2 n te 3 n+ 1," *Physical Review X*, vol. 9, no. 4, p. 041039, 2019.

[70] B. Li, J.-Q. Yan, D. M. Pajerowski, E. Gordon, A.-M. Nedić, Y. Sizyuk, L. Ke, P. P. Orth, D. Vaknin, and R. J. McQueeney, "Competing magnetic interactions in the antiferromagnetic topological insulator mnbi 2 te 4," *Physical review letters*, vol. 124, no. 16, p. 167204, 2020.

[71] H. Li, S. Liu, C. Liu, J. Zhang, Y. Xu, R. Yu, Y. Wu, Y. Zhang, and S. Fan, "Antiferromagnetic topological insulator mnbi 2 te 4: synthesis and magnetic properties," *Physical Chemistry Chemical Physics*, vol. 22, no. 2, pp. 556–563, 2020.

[72] L. Ding, C. Hu, F. Ye, E. Feng, N. Ni, and H. Cao, "Crystal and magnetic structures of magnetic topological insulators mnbi 2 te 4 and mnbi 4 te 7," *Physical Review B*, vol. 101, no. 2, p. 020412, 2020.

[73] S. Muff, F. Von Rohr, G. Landolt, B. Slomski, A. Schilling, R. J. Cava, J. Osterwalder, and J. H. Dil, "Separating the bulk and surface n-to p-type transition in the topological insulator gebi 4- x sb x te 7," *Physical Review B*, vol. 88, no. 3, p. 035407, 2013.

[74] P. Swatek, Y. Wu, L.-L. Wang, K. Lee, B. Schrunk, J. Yan, and A. Kaminski, "Gapless dirac surface states in the antiferromagnetic topological insulator mnbi 2 te 4," *Physical Review B*, vol. 101, no. 16, p. 161109, 2020.

[75] S. H. Lee, Y. Zhu, Y. Wang, L. Miao, T. Pillsbury, H. Yi, S. Kempinger, J. Hu, C. A. Heikes, P. Quarterman, *et al.*, "Spin scattering and noncollinear spin structure-induced intrinsic anomalous hall effect in antiferromagnetic topological insulator mnb i 2 t e 4," *Physical Review Research*, vol. 1, no. 1, p. 012011, 2019.

[76] D. Nevola, H. X. Li, J.-Q. Yan, R. Moore, H.-N. Lee, H. Miao, and P. D. Johnson, "Coexistence of surface ferromagnetism and a gapless topological state in mnbi 2 te 4," *Physical Review Letters*, vol. 125, no. 11, p. 117205, 2020.

[77] C. Yan, S. Fernandez-Mulligan, R. Mei, S. H. Lee, N. Protic, R. Fukumori, B. Yan, C. Liu, Z. Mao, and S. Yang, "Origins of electronic bands in the antiferromagnetic topological insulator mnbi 2 te 4," *Physical Review B*, vol. 104, no. 4, p. L041102, 2021.

[78] R. Vidal, H. Bentmann, T. Peixoto, A. Zeugner, S. Moser, C.-H. Min, S. Schatz, K. Kißner, M. Ünzelmann, C. Fornari, *et al.*, "Surface states and rashba-type spin polarization in antiferromagnetic mnbi 2 te 4 (0001)," *Physical Review B*, vol. 100, no. 12, p. 121104, 2019.

[79] D. Estyunin, I. I. Klimovskikh, A. M. Shikin, E. Schwier, M. Otrokov, A. Kimura, S. Kumar, S. Filnov, Z. S. Aliev, M. Babanly, *et al.*, "Signatures of temperature driven antiferromagnetic transition in the electronic structure of topological insulator mnbi2te4," *APL Materials*, vol. 8, no. 2, p. 021105, 2020.

[80] C. Hu, L. Ding, K. N. Gordon, B. Ghosh, H.-J. Tien, H. Li, A. G. Linn, S.-W. Lien, C.-Y. Huang, S. Mackey, *et al.*, "Realization of an intrinsic ferromagnetic topological state in $mnbi_8te_{13}$," *Science Advances*, vol. 6, no. 30, p. eaba4275, 2020.

[81] L. Ding, C. Hu, E. Feng, C. Jiang, I. A. Kibalin, A. Gukasov, M. Chi, N. Ni, and H. Cao, "Neutron diffraction study of magnetism in van der waals layered mnbi2n te3n+ 1," *Journal of Physics D: Applied Physics*, vol. 54, no. 17, p. 174003, 2021.

[82] M. Campostrini, M. Hasenbusch, A. Pelissetto, P. Rossi, and E. Vicari, "Critical exponents and equation of state of the three-dimensional heisenberg universality class," *Physical Review B*, vol. 65, no. 14, p. 144520, 2002.

[83] A. Taroni, S. T. Bramwell, and P. C. Holdsworth, "Universal window for two-dimensional critical exponents," *Journal of Physics: Condensed Matter*, vol. 20, no. 27, p. 275233, 2008.

[84] A. R. Wildes, V. Simonet, E. Ressouche, G. J. Mcintyre, M. Avdeev, E. Suard, S. A. Kimber, D. Lançon, G. Pepe, B. Moubaraki, *et al.*, "Magnetic structure of the quasi-two-dimensional antiferromagnet nips 3," *Physical Review B*, vol. 92, no. 22, p. 224408, 2015.

[85] B. Li, D. M. Pajerowski, S. X. Riberolles, L. Ke, J.-Q. Yan, and R. McQueeney, "Quasi-two-dimensional ferromagnetism and anisotropic interlayer couplings in the magnetic topological insulator mnbi 2 te 4," *Physical Review B*, vol. 104, no. 22, p. L220402, 2021.

[86] A. A. Soluyanov and D. Vanderbilt, "Computing topological invariants without inversion symmetry," *Physical Review B*, vol. 83, no. 23, p. 235401, 2011.

[87] L. Fu, "Hexagonal warping effects in the surface states of the topological insulator bi 2 te 3," *Physical review letters*, vol. 103, no. 26, p. 266801, 2009.

[88] A. K. Geim and I. V. Grigorieva, "Van der waals heterostructures," *Nature*, vol. 499, no. 7459, pp. 419–425, 2013.

[89] S. Tian, S. Gao, S. Nie, Y. Qian, C. Gong, Y. Fu, H. Li, W. Fan, P. Zhang, T. Kondo, S. Shin, J. Adell, H. Fedderwitz, H. Ding, Z. Wang, T. Qian, and H. Lei, "Magnetic topological insulator $mnbi_6te_{10}$ with a zero-field ferromagnetic state and gapped dirac surface states," *Phys. Rev. B*, vol. 102, p. 035144, Jul 2020.

[90] S. Ono and H. Watanabe, "Unified understanding of symmetry indicators for all internal symmetry classes," *Physical Review B*, vol. 98, no. 11, p. 115150, 2018.

[91] H. Watanabe, H. C. Po, and A. Vishwanath, "Structure and topology of band structures in the 1651 magnetic space groups," *Science advances*, vol. 4, no. 8, p. eaat8685, 2018.

[92] K. N. Gordon, H. Sun, C. Hu, A. G. Linn, H. Li, Y. Liu, P. Liu, S. Mackey, Q. Liu, N. Ni, *et al.*, "Strongly gapped topological surface states on protected surfaces of antiferromagnetic mnbi _4 te _7 and mnbi _6 te _{10}," *arXiv preprint arXiv:1910.13943*, 2019.

[93] L. Xu, Y. Mao, H. Wang, J. Li, Y. Chen, Y. Xia, Y. Li, J. Zhang, H. Zheng, K. Huang, *et al.*, "Persistent gapless surface states in mnbi2te4/bi2te3 superlattice antiferromagnetic topological insulator," *arXiv preprint arXiv:1910.11014*, 2019.

[94] N. H. Jo, L.-L. Wang, R.-J. Slager, J. Yan, Y. Wu, K. Lee, B. Schrunk, A. Vishwanath, and A. Kaminski, "Intrinsic axion insulating behavior in antiferromagnetic mnbi 6 te 10," *Physical Review B*, vol. 102, no. 4, p. 045130, 2020.

[95] X. Qian, J. Liu, L. Fu, and J. Li, "Quantum spin hall effect in two-dimensional transition metal dichalcogenides," *Science*, vol. 346, no. 6215, pp. 1344–1347, 2014.

[96] Z. Fei, T. Palomaki, S. Wu, W. Zhao, X. Cai, B. Sun, P. Nguyen, J. Finney, X. Xu, and D. H. Cobden, "Edge conduction in monolayer wte2," *Nature Physics*, vol. 13, no. 7, pp. 677–682, 2017.

[97] X.-M. Ma, Z. Chen, E. F. Schwier, Y. Zhang, Y.-J. Hao, S. Kumar, R. Lu, J. Shao, Y. Jin, M. Zeng, *et al.*, "Hybridization-induced gapped and gapless states on the surface of magnetic topological insulators," *Physical Review B*, vol. 102, no. 24, p. 245136, 2020.

[98] X. Wu, J. Li, X.-M. Ma, Y. Zhang, Y. Liu, C.-S. Zhou, J. Shao, Q. Wang, Y.-J. Hao, Y. Feng, *et al.*, "Distinct topological surface states on the two terminations of mnbi 4 te 7," *Physical Review X*, vol. 10, no. 3, p. 031013, 2020.

[99] R. Yu, X. L. Qi, A. Bernevig, Z. Fang, and X. Dai, "Equivalent expression of z 2 topological invariant for band insulators using the non-abelian berry connection," *Physical Review B*, vol. 84, no. 7, p. 075119, 2011.

[100] C. Hu, S.-W. Lien, E. Feng, S. Mackey, H.-J. Tien, I. I. Mazin, H. Cao, T.-R. Chang, and N. Ni, "Tuning magnetism and band topology through antisite defects in sb-doped $mnbi_4te_7$," *Phys. Rev. B*, vol. 104, p. 054422, Aug 2021.

[101] J. Wu, F. Liu, M. Sasase, K. Ienaga, Y. Obata, R. Yukawa, K. Horiba, H. Kumigashira, S. Okuma, T. Inoshita, *et al.*, "Natural van der waals heterostructural single crystals with both magnetic and topological properties," *Science advances*, vol. 5, no. 11, p. eaax9989, 2019.

[102] M. Shi, B. Lei, C. Zhu, D. Ma, J. Cui, Z. Sun, J. Ying, and X. Chen, "Magnetic and transport properties in the magnetic topological insulators mnb i 2 t e 4 (b i 2 t e 3) n (n= 1, 2)," *Physical Review B*, vol. 100, no. 15, p. 155144, 2019.

[103] J.-Q. Yan, Y. Liu, D. Parker, Y. Wu, A. Aczel, M. Matsuda, M. McGuire, and B. Sales, "A-type antiferromagnetic order in mnbi 4 te 7 and mnbi 6 te 10 single crystals," *Physical Review Materials*, vol. 4, no. 5, p. 054202, 2020.

[104] H. Deng, Z. Chen, A. Wołłoś, M. Konczykowski, K. Sobczak, J. Sitnicka, I. V. Fedorchenko, J. Borysiuk, T. Heider, ŁL. Pluciński, K. Park, A. B. Georgescu, J. Cano, and L. Krusin Elbaum, "High-temperature quantum anomalous Hall regime in a MnBi2Te4/Bi2Te3 superlattice," *Nature Physics*, Aug. 2020.

[105] J.-Q. Yan, S. Okamoto, M. A. McGuire, A. F. May, R. J. McQueeney, and B. C. Sales, "Evolution of structural, magnetic, and transport properties in mnbi 2- x sb x te 4," *Physical Review B*, vol. 100, no. 10, p. 104409, 2019.

[106] T. Murakami, Y. Nambu, T. Koretsune, G. Xiangyu, T. Yamamoto, C. M. Brown, and H. Kageyama, "Realization of interlayer ferromagnetic interaction in mns b 2 t e 4 toward the magnetic weyl semimetal state," *Physical Review B*, vol. 100, no. 19, p. 195103, 2019.

[107] Y. Liu, L.-L. Wang, Q. Zheng, Z. Huang, X. Wang, M. Chi, Y. Wu, B. C. Chakoumakos, M. A. McGuire, B. C. Sales, *et al.*, "Site mixing for engineering magnetic topological insulators," *Physical Review X*, vol. 11, no. 2, p. 021033, 2021.

[108] M.-H. Du, J. Yan, V. R. Cooper, and M. Eisenbach, "Tuning fermi levels in intrinsic antiferromagnetic topological insulators mnbi2te4 and mnbi4te7 by defect engineering and chemical doping," *Advanced Functional Materials*, vol. 31, no. 3, p. 2006516, 2021.

[109] M. Winter, "Webelements^tm."

[110] C. Hu, M. A. Tanatar, R. Prozorov, and N. Ni, "Defect-driven ferrimagnetism and hidden magnetization in mnbi _2 te _4," *arXiv preprint arXiv:2106.08969*, 2021.

[111] Y. Lai, L. Ke, J. Yan, R. D. McDonald, and R. J. McQueeney, "Defect-driven ferrimagnetism and hidden magnetization in mnbi _2 te _4," *arXiv preprint arXiv:2102.05797*, 2021.

[112] S.-Y. Xu, Y. Xia, L. Wray, S. Jia, F. Meier, J. Dil, J. Osterwalder, B. Slomski, A. Bansil, H. Lin, *et al.*, "Topological phase transition and texture inversion in a tunable topological insulator," *Science*, vol. 332, no. 6029, pp. 560–564, 2011.

[113] T.-R. Chang, S.-Y. Xu, G. Chang, C.-C. Lee, S.-M. Huang, B. Wang, G. Bian, H. Zheng, D. S. Sanchez, I. Belopolski, *et al.*, "Prediction of an arc-tunable weyl fermion metallic state in mo x w 1- x te 2," *Nature communications*, vol. 7, no. 1, pp. 1–9, 2016.

[114] B. J. Wieder and B. A. Bernevig, "The axion insulator as a pump of fragile topology," *arXiv preprint arXiv:1810.02373*, 2018.

[115] C. Hu, M. A. Tanatar, R. Prozorov, and N. Ni, "Unusual dynamic susceptibility arising from soft ferromagnetic domains in mnbi8te13 and sb-doped mnbi2nte3n+ 1 (n= 2, 3)," *arXiv preprint arXiv:2106.08969*, 2021.

[116] Y. Hu, L. Xu, M. Shi, A. Luo, S. Peng, Z. Wang, J. Ying, T. Wu, Z. Liu, C. Zhang, *et al.*, "Universal gapless dirac cone and tunable topological states in (mnb i 2 t e 4) m (b i 2 t e 3) n heterostructures," *Physical Review B*, vol. 101, no. 16, p. 161113, 2020.

[117] I. I. Klimovskikh, M. M. Otrokov, D. Estyunin, S. V. Eremeev, S. O. Filnov, A. Koroleva, E. Shevchenko, V. Voroshnin, A. G. Rybkin, I. P. Rusinov, *et al.*, "Tunable 3d/2d magnetism in the (mnbi 2 te 4)(bi 2 te 3) m topological insulators family," *npj Quantum Materials*, vol. 5, no. 1, pp. 1–9, 2020.

[118] S. Wimmer, J. Sánchez-Barriga, P. Küppers, A. Ney, E. Schierle, F. Freyse, O. Caha, J. Michalicka, M. Liebmann, D. Primetzhofer, *et al.*, "Ferromagnetic mnsb2te4: A topological insulator with magnetic gap closing at high curie temperatures of 45-50 k," *arXiv preprint arXiv:2011.07052*, 2020.

[119] W. Ge, P. M. Sass, J. Yan, S. H. Lee, Z. Mao, and W. Wu, "Direct evidence of ferromagnetism in mnsb 2 te 4," *Physical Review B*, vol. 103, no. 13, p. 134403, 2021.

[120] J. Wu, F. Liu, C. Liu, Y. Wang, C. Li, Y. Lu, S. Matsuishi, and H. Hosono, "Toward 2d magnets in the (mnbi2te4)(bi2te3) n bulk crystal," *Advanced Materials*, p. 2001815, 2020.

[121] H. Li, Y. Li, Y.-K. Lian, W. Xie, L. Chen, J. Zhang, Y. Wu, and S. Fan, "Spin glass state in layered compound mnsb2te4," *arXiv preprint arXiv:2104.00898*, 2021.

[122] J. A. Mydosh, *Spin glasses: an experimental introduction.* CRC Press, 1993.

[123] J. Mydosh, "Spin glasses: redux: an updated experimental/materials survey," *Reports on Progress in Physics*, vol. 78, no. 5, p. 052501, 2015.

[124] D. Gatteschi, R. Sessoli, and J. Villain, *Molecular nanomagnets*, vol. 5. Oxford University Press on Demand, 2006.

[125] M. Balanda, "Ac susceptibility studies of phase transitions and magnetic relaxation: Conventional, molecular and low-dimensional magnets," *Acta Phys. Pol. A*, vol. 124, no. 6, pp. 964–976, 2013.

[126] K. S. Cole and R. H. Cole, "Dispersion and absorption in dielectrics i. alternating current characteristics," *The Journal of chemical physics*, vol. 9, no. 4, pp. 341–351, 1941.

[127] C. Topping and S. Blundell, "Ac susceptibility as a probe of low-frequency magnetic dynamics," *Journal of Physics: Condensed Matter*, vol. 31, no. 1, p. 013001, 2018.

[128] R. Prozorov and V. G. Kogan, "Effective demagnetizing factors of diamagnetic samples of various shapes," *Physical Review Applied*, vol. 10, no. 1, p. 014030, 2018.

[129] A. Hubert and R. Schäfer, *Magnetic domains: the analysis of magnetic microstructures*. Springer Science & Business Media, 2008.

[130] R. Prozorov, Y. Yeshurun, T. Prozorov, and A. Gedanken, "Magnetic irreversibility and relaxation in assembly of ferromagnetic nanoparticles," *Physical Review B*, vol. 59, no. 10, p. 6956, 1999.

[131] R. Prozorov and T. Prozorov, "Effective collective barrier for magnetic relaxation in frozen ferrofluids," *Journal of magnetism and magnetic materials*, vol. 281, no. 2-3, pp. 312–317, 2004.

[132] V. Tsurkan, J. Hemberger, M. Klemm, S. Klimm, A. Loidl, S. Horn, and R. Tidecks, "Ac susceptibility studies of ferrimagnetic fecr 2 s 4 single crystals," *Journal of Applied Physics*, vol. 90, no. 9, pp. 4639–4644, 2001.

[133] C. Hu, A. Gao, B. S. Berggren, H. Li, R. Kurleto, D. Narayan, I. Zeljkovic, D. Dessau, S. Xu, and N. Ni, "Growth, characterization, and chern insulator state in mnbi 2 te 4 via the chemical vapor transport method," *Physical Review Materials*, vol. 5, no. 12, p. 124206, 2021.

[134] Z. Huang, M.-H. Du, J. Yan, and W. Wu, "Native defects in antiferromagnetic topological insulator mnbi 2 te 4," *Physical Review Materials*, vol. 4, no. 12, p. 121202, 2020.

[135] Y. Yuan, X. Wang, H. Li, J. Li, Y. Ji, Z. Hao, Y. Wu, K. He, Y. Wang, Y. Xu, *et al.*, "Electronic states and magnetic response of mnbi2te4 by scanning tunneling microscopy and spectroscopy," *Nano letters*, vol. 20, no. 5, pp. 3271–3277, 2020.

[136] A. Gao, Y.-F. Liu, C. Hu, J.-X. Qiu, C. Tzschaschel, B. Ghosh, S.-C. Ho, D. Bérubé, R. Chen, H. Sun, *et al.*, "Layer hall effect in a 2d topological axion antiferromagnet," *Nature*, vol. 595, no. 7868, pp. 521–525, 2021.

[137] S. Wimmer, J. Sánchez-Barriga, P. Küppers, A. Ney, E. Schierle, F. Freyse, O. Caha, J. Michalička, M. Liebmann, D. Primetzhofer, *et al.*, "Mn-rich mnsb2te4: A topological insulator with magnetic gap closing at high curie temperatures of 45–50 k," *Advanced Materials*, vol. 33, no. 42, p. 2102935, 2021.

[138] Y. Hor, P. Roushan, H. Beidenkopf, J. Seo, D. Qu, J. Checkelsky, L. Wray, D. Hsieh, Y. Xia, S.-Y. Xu, *et al.*, "Development of ferromagnetism in the doped topological insulator bi 2- x mn x te 3," *Physical Review B*, vol. 81, no. 19, p. 195203, 2010.

[139] Y. Lai, L. Ke, J. Yan, R. D. McDonald, and R. J. McQueeney, "Defect-driven ferrimagnetism and hidden magnetization in mnbi _2 te _4," *arXiv preprint arXiv:2102.05797*, 2021.

[140] D. A. Estyunin, I. I. Klimovskikh, A. M. Shikin, E. F. Schwier, M. M. Otrokov, A. Kimura, S. Kumar, S. O. Filnov, Z. S. Aliev, M. B. Babanly, and E. V. Chulkov, "Signatures of temperature driven antiferromagnetic transition in the electronic structure of topological insulator $mnbi_2te_4$," *APL Materials*, vol. 8, no. 2, p. 021105, 2020.

[141] P. Swatek, Y. Wu, L.-L. Wan, K. Lee, B. Schrunk, J. Yan, and A. Kaminski, "Gapless dirac surface states in the antiferromagnetic topological insulator $mnbi_2te_4$," *Physical Review B*, vol. 101, p. 161109(R), 2020.

[142] M.-H. Du, J. Yan, V. R. Cooper, and M. Eisenbach, "Tuning fermi levels in intrinsic antiferromagnetic topological insulators $mnbi_2te_4$ and $mnbi_4te_7$ by defect engineering and chemical doping," *Advanced Functional Materials*, vol. 31, no. 2006516, pp. 1–8, 2021.

[143] P. E. Blöchl, "Projector augmented-wave method," *Physical review B*, vol. 50, no. 24, p. 17953, 1994.

[144] G. Kresse and D. Joubert, "From ultrasoft pseudopotentials to the projector augmented-wave method," *Physical review b*, vol. 59, no. 3, p. 1758, 1999.

[145] G. Kresse and J. Furthmüller, "Efficiency of ab-initio total energy calculations for metals and semiconductors using a plane-wave basis set," *Computational materials science*, vol. 6, no. 1, pp. 15–50, 1996.

[146] J. P. Perdew, K. Burke, and M. Ernzerhof, "Generalized gradient approximation made simple," *Physical review letters*, vol. 77, no. 18, p. 3865, 1996.

[147] S. Dudarev, G. Botton, S. Y. Savrasov, Z. Szotek, W. Temmerman, and A. Sutton, "Electronic structure and elastic properties of strongly correlated metal oxides from first principles: Lsda+ u, sic-lsda and eels study of uo2 and nio," *Physica status solidi (a)*, vol. 166, no. 1, pp. 429–443, 1998.

[148] N. Marzari and D. Vanderbilt, "Maximally localized generalized wannier functions for composite energy bands," *Physical review B*, vol. 56, no. 20, p. 12847, 1997.